SEARCH FOR HIGH-MASS RESONANCES DECAYING TO $e\mu$ IN $p\bar{p}$ COLLISIONS AT $\sqrt{s} = 1.96$ TeV

Kristian A. Hahn

A DISSERTATION

in

Physics and Astronomy

Presented to the Faculties of the University of Pennsylvania in Partial Fulfillment of the Requirements for the Degree of Doctor of Philosophy

2006

Nigel S. Lockyer

Supervisor of Dissertation

Andrea J. Liu

Graduate Group Chairperson

To my parents, Cynthia and Walter Allan Hahn

Acknowledgments

I am deeply indebted to my parents. Without their sacrifice, encouragement and continued support I could not have reached this point in my career. I am also extremely grateful to :

Prof. Nigel Lockyer, my supervisor, for his faith in me and for guiding my transition from engineering student to physicist.

Prof. Peter Wittich, for his friendship, instruction and encouragement.

Prof. Joe Kroll, for pushing me when my enthusiasm had flagged.

Prof. Brig Williams, for allowing me an opportunity to experience an ATLAS test-beam before I entered graduate school.

Dr. Ted Liu, for providing me freedom and encouragement in my work on the CDF Level 2 (PULSAR) Trigger upgrade.

All in the Penn HEP group, for kindling my interest in hardware and computing.

And, of course, Seema, my fiancee, for her love, support and patience.

ABSTRACT

SEARCH FOR HIGH-MASS RESONANCES DECAYING TO $e\mu$ IN $p\bar{p}$ COLLISIONS AT $\sqrt{s} = 1.96$ TeV

Kristian Hahn

Nigel Lockyer

We describe a general search for resonances decaying to a neutral $e\mu$ final state in $p\bar{p}$ collisions at a center-of-mass energy of 1.96 TeV. Using a data sample representing 344 pb^{-1} of integrated luminosity recorded by the CDF II experiment, we compare Standard Model predictions with the number of observed events for invariant masses between 50 and 800 GeV/c^2. Finding no significant excess (5 events observed vs. 7.7 ± 0.8 expected for $M_{e\mu} > 100$ GeV/c^2), we set limits on sneutrino and Z' masses as functions of lepton family number violating couplings.

Contents

List of Figures

List of Tables

Chapter 1

Introduction

The contemporary graduate student thesis in experimental particle physics typically begins with a homage to the Standard Model, the theory of the strong, weak and electromagnetic interactions that represents current understanding of how Nature operates at small-distance and high-energy scales. Praise for the Standard Model is not undue; it has withstood countless experimental tests over the past 40 years and has emerged with its predictions precisely verified.[1] Only now, with an enormous international investment in large scale experiment, does the particle physics community believe that the limits of the Standard Model's applicability might finally be surpassed and that the near future will again be marked by the discovery of "New Physics".

The Standard Model's success stems from the recognition of fundamental symmetries. Particles in the Standard Model are categorized according to quantum numbers associated with the $SU(3) \times SU(2)_L \times U(1)$ gauge symmetries and fundamental forces are described in terms of corresponding gauge fields. Symmetry is not merely an organizational principle in the Standard Model; its real

[1]The only notable exception is the evidence for neutrino oscillation, discussed later in this section. Though not a direct test of the SM, cosmological measurements that support the existence of "Dark Matter" may also lead to conflicts with SM predictions.

importance follows from the predictive power it confers. The discovery of a third charged lepton (the tau) in 1975 [1], for example, foretold of a third generation of quarks, needed for the cancellation of divergent terms at higher order in the Standard Model. Generational symmetry was regained with the discovery of the bottom quark at Fermilab in 1978 [2]. Weak $SU(2)$ symmetry demanded a partner for the bottom, the top, discovered by CDF [3] and D0 [4] in 1995. Symmetry likewise required an $SU(2)$ partner for the tau, the tau neutrino, which was first observed directly at Fermilab in 2000 [5].

While appeals to symmetry in the Standard Model have often been fulfilled by experiment, discoveries of *violated* symmetry have proven equally prescient. The discovery of parity violation in 1956 [6] provided evidence for the V-A couplings of electrons and electron-neutrinos in weak decays, a description that would later apply universally to weak charged currents in the Standard Model. In 1964, with experimental evidence for only two quark generations, the discovery of indirect CP violation [7] hinted at a third quark generation and a 3-dimensional quark mixing matrix with an additional, CP-violating phase. These discoveries introduced what was considered New Physics at the time and later motivated the development of important aspects of the Standard Model.

The most recent discovery of violated symmetry, that of individual lepton family number (or lepton flavor), will undoubtedly impact the Standard Model as well. The first experimental evidence of lepton flavor violation was observed by the Homestake experiment [8], which measured a deficit of electron neutrinos relative to the prediction from the Standard Solar Model [9]. More recently, the Super-Kamiokande collaboration reported an anomalous detection rate of atmospheric muon-neutrinos [10] while SNO has both confirmed the validity of the Standard Solar Model and conclusively established the disappearance of electron-neutrinos *en route* to Earth [11].

The neutrino mixing results are the first to conflict with Standard Model predictions. The Standard Model assumes that neutrinos are massless particles and therefore unable to participate in flavor-changing interactions. While neutrino data prove these assumptions inaccurate, the scale of the New Physics they imply is still in question. It may be possible to account for these results by simply extending the Standard Model to include neutrino masses [12]. A more exciting (and some feel more natural [13]) explanation is that lepton flavor violation is the first indication of physics beyond the Standard Model.

Motivated by the existing evidence for lepton flavor violation and by the historical connection between violated symmetry and New Physics, we have conducted a general search for the lepton flavor violating decays of heavy neutral particles at CDF [14]. We consider the production of new scalar and vector particles from $p\bar{p}$ and their decay to an electron-muon final state. We search $e\mu$ invariant masses between 50 and 800 GeV/c^2 and compare our results with Standard Model predictions. Finding no significant excess of $e\mu$ events, we set limits on lepton flavor violating couplings and particle masses in two specific New Physics models.

Chapter 2

Lepton Flavor Violation

2.1 The Standard Model

The mechanism that enforces lepton flavor conservation in the Standard Model differs from that which preserves most other conserved quantities. As was first understood by Noether, conservation laws are a natural result of a Lagrangian's invariance under transformation. The Standard Model Lagrangian is invariant with respect to many types of transformations (*ie*, symmetries) and Noether's Theorem implies that conserved quantities are associated with each. Momentum conservation, for instance, is explained in terms of the invariance of the free-particle Lagrangian under displacement while the conservation of electric charge follows from the symmetry of the Standard Model Lagrangian under $U(1)$ gauge transformation.

Lepton flavor, on the other hand, is preserved in the Standard Model on account of an "accidental" symmetry of the underlying field theory. A field theory in four space-time dimensions is renormalizable only if its terms contain combinations of field operators of summed mass dimension less than or equal to 4. Field operators otherwise appear with a coupling of negative mass dimension,

leading to the divergent growth of successive terms in the perturbation expansion. Terms that describe direct lepton flavor violating interactions first occur with mass dimension 5 [15] and therefore cannot be included in the Standard Model Lagrangian if it is to remain renormalizable.

Thus, conservation of lepton flavor does not follow from transformational symmetry but from a constraint on the types of operators appearing in the Standard Model Lagrangian. This distinction is compelling because of its possible relation to New Physics. If the real purview of the Standard Model is as a weak scale approximation of physics at higher energy scales, then the renormalization requirement on the Standard Model Lagrangian may be relaxed. If interpreted as an "effective" field theory, the Standard Model may admit non-renormalizable terms representing low-energy phenomenology associated with New Physics. Non-renormalizability would be tolerated since, in this view, the Standard Model would not need to describe physics beyond the electroweak scale but only account for the manifestation of that physics at accessible energies[1].

Searches for lepton flavor violation have long been considered sensitive probes of New Physics because lepton flavor is not "protected" by symmetry. Aside from results in the neutrino sector however, precision measurements have found no evidence for its occurrence. Typical searches seek to measure deviations from Standard Model predictions for processes involving charged leptons. The most familiar of such experiments are the searches for muon conversion, $\mu \rightarrow e\gamma$. Existing limits on this rare decay are stringent; the MEGA collaboration constrained the relative branching ratio $\Gamma_R(\mu \rightarrow e\gamma) = BR(\mu \rightarrow e\gamma)/BR(\mu \rightarrow e\bar{\nu}_e\nu_\mu)$ to $\lesssim 10^{-11}$ [16]. Similar limits have been obtained from experiments sensitive to related processes (*eg:* $\Gamma_R(\mu^- \rightarrow e^-e^+e^-) \lesssim 10^{-12}$ by SINDRUM-II [17] and

[1] A parallel is found in Fermi's theory of weak interactions. The theory is non-renormazliable but successfully accounts for the phenomenology associated with weak charged currents at energies below the W production threshold.

$\Gamma_R(\mu^- \to e^-\gamma\gamma) \lesssim 10^{-10}$ at LAMPF [18]).

While impressively precise, these limits do not preclude a discovery of lepton flavor violating New Physics. Indirect searches at low momentum transfer can be susceptible to interference effects that hinder the detection of new phenomena. In addition, limits on the production of new particles often contain a strong dependence on the mass scale presumed for the particles. In some models heavy New Physics can decouple from weak-scale phenomena altogether and elude precision tests that search for deviations from Standard Model predictions at low energy [19]. As a result, the indirect limits are generally model-dependent and usually leave open sufficient parameter-space to accommodate a direct observation of the lepton flavor violating decays of heavy new particles.

2.2 Supersymmetry and R-parity Violation

Issues related to renormalization also motivate a discussion of Supersymmetry (SUSY). Although the requirement of renormalizability may be relaxed for operators representing weak-scale, lepton flavor violating interactions of new particles, terms contributing to the Standard Model Higgs boson's mass must remain renormalizable. This condition is not easily met by extensions to the Standard Model that contain heavy new particles because the Higgs is extremely sensitive to the masses of all particles to which it couples. Corrections to the square of the Higgs mass, Δm_H^2, diverge quadratically as the mass scale of new particles increases. This pushes the Higgs mass toward that of the heaviest objects in the theory and far from the range required for the Higgs to function as the source of electroweak symmetry breaking. Conventionally termed the "hierarchy problem", the sensitivity of the Higgs mass on high energy scales stems from its role as a fundamental scalar. Fermions, for example, do not suffer similar instability since

their masses are protected by an approximate chiral symmetry [20].

Interestingly, a symmetry may also serve to stabilize the Higgs. Without a systematic means of removing divergences, equally large counter-terms must be added in order to cancel corrections to the Higgs mass so that it remains on order $\lesssim 1$ TeV/c^2. While essentially successful, the deliberate addition of large counter-terms to effect delicate cancellation constitutes a "fine-tuning" of parameters that is felt by most to be unnatural. Supersymmetric theories, on the other hand, remove large corrections to m_H at every order through a correspondence between fermions and bosons.

The first term in the brackets of Eqn. 2.1 shows the corrections to m_H^2 that are associated with fermions. Λ_{UV} denotes the ultra-violet cutoff used in regularization and can lie many orders of magnitude above the weak scale.

$$\Delta m_H^2 \propto [6m_f^2 \ln(\Lambda_{\mathrm{UV}}/\mathrm{m_f}) - 6\mathrm{m_b^2}\ln(\Lambda_{\mathrm{UV}}/\mathrm{m_b})] \tag{2.1}$$

SUSY theories cancel corrections from heavy fermions by pairing each with a bosonic partner, resulting in the second term in Eqn. 2.1. This terms cancels the previous at every order in perturbation if the symmetry between fermions and bosons is exact (*ie,* if they are mass degenerate). The removal of divergences by this mechanism is robust and preferred over the "fine-tuning" solution, which requires a "re-tuning" of counter-terms at every mass scale.

The widely referenced "Minimal Supersymmetric Standard Model" (MSSM) is the minimal extension to the Standard Model that realizes supersymmetry. It does so by pairing every Standard Model fermion (gauge boson) with a bosonic (fermionic) *superpartner* [2]. Standard Model particles (or "particles") and their SUSY partners ("sparticles") are grouped in *supermultiplets* and share the same

[2]The MSSM also includes 5 Higgs particles, representing additional degrees of freedom remaining from two Higgs doublets after electroweak symmetry breaking.

$SU(3) \times SU(2)_L \times U(1)$ quantum numbers. Particles and their superpartners differ by a half unit of spin but have equal masses before SUSY is broken.[3] Supermultiplets are referred to as "chiral" or "vector" depending on whether the particles included are fermions or bosons. Table 2.1 shows the (s)particle content of the chiral multiplets, which are relevant to the discussion that follows.

Names		Bosons	Fermions
(s)quarks ×3 families	Q	$(\tilde{u}_L, \tilde{d}_L)$	(u_L, d_L)
	$\bar{U}$	$\tilde{u}_R^*$	$u_R^\dagger$
	$\bar{D}$	$\tilde{d}_R^*$	$d_R^\dagger$
(s)leptons ×3 families	L	$(\tilde{\nu}, \tilde{e}_L)$	(ν, e_L)
	$\bar{E}$	$\tilde{e}_R^*$	$e_R^\dagger$
Higgs(inos)	H_u	(H_u^+, H_u^0)	$(\bar{H}_u^+, \bar{H}_u^0)$
	H_d	(H_d^0, H_d^-)	$(\bar{H}_d^0, \bar{H}_d^-)$

Table 2.1: **Chiral Supermultiplets.** The MSSM introduces bosonic partners for the SM fermions. Members of the (s)quark and (s)lepton multiplets are important in our SUSY signal model.

Non-gauge interactions in the MSSM derive from an analytic function of the field operators, the *superpotential* (W), shown in Eqn. 2.2.

[3]SUSY must be a broken symmetry since we do not observe sparticles with masses equal to those of the known particles. The mechanism by which SUSY is broken is not important in this analysis.

$$W = \epsilon_{\alpha\beta}\mu H_1^\alpha H_2^\beta + [y_e H_1 \bar{L}\bar{E} + y_d H_1 Q \bar{D} + y_u H_2 Q \bar{U}] \tag{2.2}$$
$$+ [\lambda_{ijk} L^i L^j \bar{E}^k + \lambda'_{ijk} L^i Q^j \bar{D}^k + \lambda''_{ijk} \bar{U}^i \bar{D}^j \bar{D}^k]$$

Interaction terms in the Lagrangian are obtained from the superpotential through the application of derivative operations shown in Eqn. 2.3.

$$\mathcal{L}_{\mathrm{W}} = -\sum_{\mathrm{i}} |\frac{\partial \mathrm{W}}{\partial \mathrm{z_i}}|^2 - \frac{1}{2}\sum_{\mathrm{ij}} [\bar{\psi}_{\mathrm{iL}} \frac{\partial^2 \mathrm{W}}{\partial \mathrm{z_i} \partial \mathrm{z_j}} \psi_{\mathrm{j}} + \mathrm{h.c.}] \tag{2.3}$$

The derivative from the first term in Eqn. 2.3 acts on the first term in Eqn. 2.2 to give rise to Higgs masses. Terms $2-4$ in Eqn. 2.2 lead to Yukawa interactions with the Higgs. The final three terms lead to the direct coupling of sparticles to Standard Model fermions and generate interactions that violate baryon number (via the λ'' terms) or total lepton number (via the λ and λ' terms). The "lambda" terms can describe processes that conflict with experiment. The λ''_{i11} parameter, for example, permits the coupling of down-type squarks to u and d quarks, initiating rapid proton decay ($\sim 10^{-2}$ s) if squarks also couple to quarks and leptons through λ'_{1i1} terms (see Fig. 2.1).

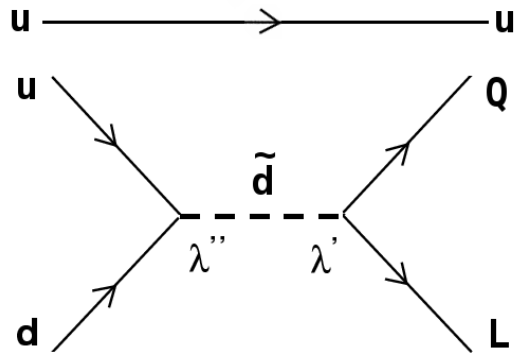

Figure 2.1: **RPV proton decay.** Proton decay, prevented by R-parity conservation in the MSSM, can proceed quickly if both λ' and λ'' RPV couplings are non-zero.

The MSSM introduces a discrete multiplicative symmetry, R-parity (R_P), to prevent this problem. The representation of the symmetry in Eqn. 2.4 shows that Standard Model particles are even under R_P while the superpartners are odd.

$$R_P = (-1)^{3B-L+2S} \tag{2.4}$$

The lambda-terms in Eqn. 2.2 violate R_P because they describe interactions in which a single sparticle ($R_P = -1$) couples to two particles ($R_P = +1$). The MSSM removes the problematic baryon and lepton number violating terms in Eqn. 2.2 by enforcing R_P conservation and setting all lambda-couplings to zero. The coupling of single sparticles to pairs of particles is then prohibited. Sparticles must be pair-produced and SUSY decay chains must terminate in a lightest supersymmetric particle, the *LSP*. Shielded by symmetry, the LSP is completely stable and is a candidate for non-baryonic, cold dark matter [21].

While R_P provides a means to suppress proton decay and generates a dark-matter candidate, theoretical justification for the symmetry is not compelling. Like the violated symmetries of the Standard Model, there is no gauge group that protects R_P in the MSSM and one might therefore anticipate that the symmetry is not exact. Furthermore, it is not necessary for *all* lambda-couplings to be exactly zero in order for the predicted rate of proton decay to meet experimental constraints. Proton decay remains prohibited in SUSY models with non-zero λ and λ' *or* non-zero λ'' couplings [22].

Lepton flavor violating interactions are permitted if R_P violating (RPV) λ and λ' couplings assume non-zero values. Fig. 2.2, for instance, describes sneutrino ($\tilde{\nu}$, the superpartner of the neutrino) production from protons and anti-protons and its lepton flavor violating decay to electrons and anti-muons, $d\bar{d} \rightarrow \tilde{\nu}_k \rightarrow \ e^-\mu^+$. The production vertex involves only down-type quarks and follows from the λ'_{i11}

term in Eqn.2.2. The λ_{1i2} coupling governs LFV sneutrino decay and its middle index, referring to the lepton flavor of the sneutrino, must match the free index of λ'_{i11}. The Hermitian conjugates of the relevant terms in Eqn. 2.2 lead to anti-sneutrino ($\bar{\tilde{\nu}}$) production and decay to an oppositely charged final-state, $d\bar{d} \rightarrow \bar{\tilde{\nu}}_k \rightarrow e^- \mu^+$.

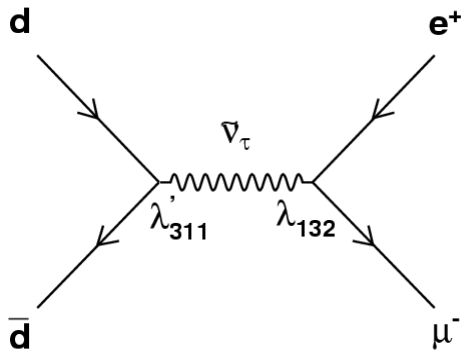

Figure 2.2: **RPV sneutrino production and decay.** Non-zero λ_{132} and λ'_{311} couplings lead to the lepton flavor violating decay to tau-sneutrinos to $e\mu$.

The SUSY portion of our analysis specifically focuses on the tau sneutrino and anti-sneutrino because their couplings are less constrained by experiment than those corresponding to other flavors. Current limits for the relevant couplings, λ_{132} and λ'_{311}, are obtained from measurements of tau lepton branching ratios at low-energy. Figs 2.3 and 2.4 present the leading order diagrams that contribute to leptonic and single-prong hadronic tau decay in the Standard Model. The branching ratios to these final-states may be enhanced relative to Standard Model predictions by the additional contributions from the RPV SUSY processes shown in Figs 2.3 and 2.4.

The coupling limits, $\lambda_{132} < 0.1 \times \frac{m(\tilde{\bar{d}})}{100\mathrm{GeV/c^2}}$ and $\lambda'_{311} < 0.05 \times \frac{m(\tilde{\bar{d}})}{100\mathrm{GeV/c^2}}$ [23] [24], depend on the mass of the exchanged sparticle (either a charged slepton or down-type squark) and weaken as the mass limit on the sparticle improves. CDF conducted a Run I RPV sneutrino search [25] that used these limits (for assumed

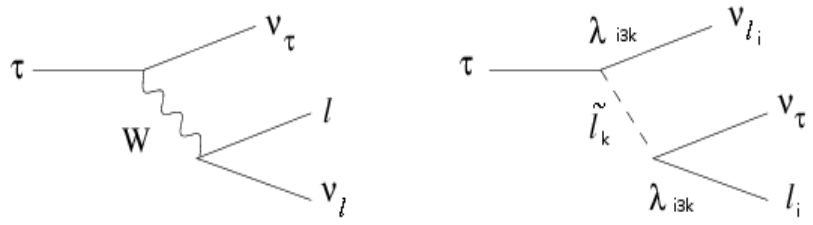

Figure 2.3: **Processes Contributing to the Measurement of λ_{132}.** Limits on λ_{132} come from measurements of the leptonic branching ratio of the tau (left), which may be enhanced by RPV squark exchange (right).

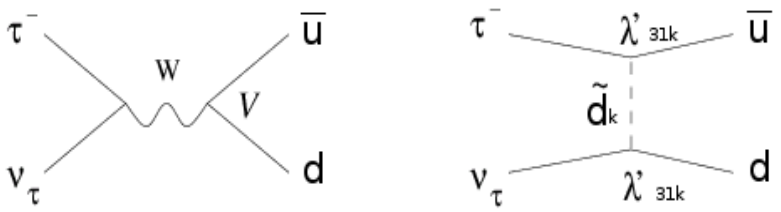

Figure 2.4: **Processes Contributing to the Measurement of λ'_{311}.** Limits on λ'_{311} come from measurements of the single-prong hadronic branching ratios of the tau (left), which may be enhanced by RPV slepton exchange (right).

100 GeV/c^2 squark and charged slepton masses) in the next-to-leading (NLO) $\tilde{\nu}_\tau$ cross section times branching ratio ($\sigma \times BR(e\mu)$) prediction. With these assumptions, the analysis constrained the $\tilde{\nu}_\tau$ mass to values below 375 GeV/c^2. Searches for muon conversion, which we discuss in the following section, imply more stringent bounds ($\sim 10^{-8}$) on products of λ and λ' couplings [26].

2.3 Extended Gauge Symmetry

Lepton flavor violation also emerges in New Physics models that contain extra gauge symmetry. Such models are often associated with *Grand Unified* (GU) theories, which seek to explain the electromagnetic, weak and strong forces as resulting from a single gauge group. Georgi and Glashow developed one of the earliest GU models in 1974 with this as their aim [27]. They proposed an $SU(5)$

symmetry that contains the $SU(3) \times SU(2)_L \times U(1)$ product as a subgroup and accommodates the three fermion generations of the Standard Model. Lepton flavor and baryon number violating interactions arise naturally in this model since quarks and leptons of the same generation are combined in multiplets and can transform into one another [28].

The minimal $SU(5)$ model is not viable however since, like the most general MSSM, it predicts a proton decay rate in excess of existing experimental bounds [29]. Although discounted as a precise model of unification, many aspects of the $SU(5)$ model have been incorporated by modern GU theories. For example, extended gauge symmetry is a common feature of unified superstring theories, which attempt to unite gravity and the known gauge forces. Recent theoretical work [30] has raised hopes that superstring theories may provide a consistent framework for gauge unification. Attention has focused on a particular 10-dimensional superstring theory, $E_8 \times E_8'$, as it easily accommodates the Standard Model gauge group and fermion families.

The Standard Model $SU(3) \times SU(2)_L \times U(1)$ symmetries are obtained from $E_8 \times E_8'$ by first breaking one of the E_8 groups to E_6. The E_6 group can undergo the following decomposition :

$$E_6 \rightarrow SO(10) \times U(1)_\psi \tag{2.5}$$

$$\rightarrow SU(5) \times U(1)_\psi \times U(1)_\eta \tag{2.6}$$

$$\rightarrow SU(3) \times SU(2)_L \times U(1) \times U(1)_\psi \times U(1)_\chi \tag{2.7}$$

Eqn. 2.7 shows that the E_6 group eventually leads to two $U(1)$ gauge groups, $U(1)_\chi$ and $U(1)_\psi$, in addition to those familiar from the Standard Model. A linear combination of the new $U(1)$ groups yields a single gauge group, $U(1)'$,

and an associated new gauge boson, the Z', that is accessible at the weak scale. E_6 models specify the combination of $U(1)_\chi$ and $U(1)_\psi$ through a parameter θ, which also determines the Z' coupling to leptons and quarks, Q'.

$$Q' = Q_\chi \cos\theta + Q_\psi \sin\theta \tag{2.8}$$

Z' couplings in E_6 models are flavor diagonal and thus the models do not allow lepton flavor violation by construction. Despite this feature these models provide a useful framework for the interpretation of our search results in terms of the LFV decays of vector particles. The models stipulate Z' production cross sections that set an overall scale for our $\sigma \times BR(e\mu)$ upper-limits. In addition, the results of Z' dilepton searches [31] are typically presented in terms of limits on E_6 models. Our use of the E_6 cross sections facilitates comparison with these results.

We consider a group of E_6-inspired models that permit lepton flavor violation. We extend the χ, ψ, η and Secluded E_6 models [32] to include flavor non-diagonal Z' couplings to $e\mu$, Q^l_{12} [33]. We determine a Z' branching ratio to $e\mu$ from Q^l_{12} in the same way that branching ratios to dileptons are calculated from the flavor diagonal couplings, Q^l_{11} and Q^l_{22}. We assume that the Z' couples to left-handed fermions only as this scenario is theoretically favored [33].

Limits exist for Q^l_{12} with respect to several Z' models [34] [36]. These limits derive from the SINDRUM-II search for coherent, neutrino-less muon conversion [35]. The experiment involves the formation of muonic atoms, created when a low energy muon beam is stopped in a target of high atomic number (Z) and mass (A). Electrons produced from the weak decay of muons in orbit $(\mu+(A,Z) \rightarrow e\bar{\nu}_e\nu_\mu+(A,Z))$ or by the conversion of photons from radiative muon capture $(\mu + (A,Z) \rightarrow \gamma\nu_\mu + (A, Z-1))$ are detected with Cerenkov counters

and drift chambers. These background processes produce a broad distribution of electron energies that is easily distinguished from the mono-energetic LFV signal ($\mu + (A, Z) \rightarrow e + (A, Z)$).

The limit on the branching ratio of LFV muon conversion relative to muon capture ($6.1 \times\ 10^{-13}$) can be used to constrain Q^l_{12}. A simple Z' model [36] that permits LFV and predicts a muon conversion rate of

$$R(\mu N \rightarrow eN) = 3.1 \times 10^{-11} \left(\frac{g_X}{g_Y}\right)^4 \left(\frac{Q^l_{12}}{10^{-5}}\right)^2 \left(\frac{1\text{TeV}}{m_{Z'}}\right)^4 \tag{2.9}$$

The g_X and g_Y parameters in Eqn. 2.9 are the new $U(1)'$ and the Standard Model $U(1)$ coupling strengths, respectively. Existing limits on $(g_X/g_Y)^2|Q^l_{12}|^2$ range from $\sim 10^{-7}$ to $\sim 10^{-6}$ for Z' masses between 0.2 and 1 TeV/c^2. In order to compare with these limits, we substitute the values of g_X specified by E_6 models and re-express the limits in terms of Q^l_{12} alone, as shown in Table 2.2.

E_6 Model	g_X/g_Y	Q^l_{12} Upper-Limit
χ	0.335	$9 \times 10^{-4}\ -\ 3 \times 10^{-3}$
ψ	0.432	$7 \times 10^{-4}\ -\ 2 \times 10^{-3}$
η	0.547	$6 \times 10^{-4}\ -\ 2 \times 10^{-3}$
Secluded	1.29	$2 \times 10^{-4}\ -\ 8 \times 10^{-4}$

Table 2.2: **Limits on Q^l_{12} for $E6$ Models.** We translate $(g_X/g_Y)Q^l_{12}$ limits from a generic Z' model to limits on Q^l_{12} in E_6 models by substituting g_X values specific to the models.

Chapter 3

Apparatus

As of this writing, experiments that search for the direct production of heavy new particles are conducted exclusively at the Fermi National Accelerator Laboratory. Fermilab's proton/anti-proton ($p\bar{p}$) collider, the Tevatron, is part of the world's highest energy particle accelerator and is used to generate 980 GeV proton and anti-proton beams. The CDF II detector is one of two situated at the Tevatron and registers the secondary particles produced in $p\bar{p}$ collisions every 396 ns. This chapter reviews the generation and acceleration of protons and anti-protons at Fermilab and describes the CDF II detector systems that we use to reconstruct the remnants of their collisions.

3.1 The Fermilab Accelerator Chain

Proton and anti-proton acceleration at Fermilab occurs in stages, sketched in Fig 3.1 and described in the following sections. In addition to their role in $p\bar{p}$ collisions, accelerated protons serve in the creation of secondary particle beams for a variety of experimental endeavors at Fermilab. These aspects of Fermilab's experimental program do not factor in our LFV $e\mu$ search and are not discussed.

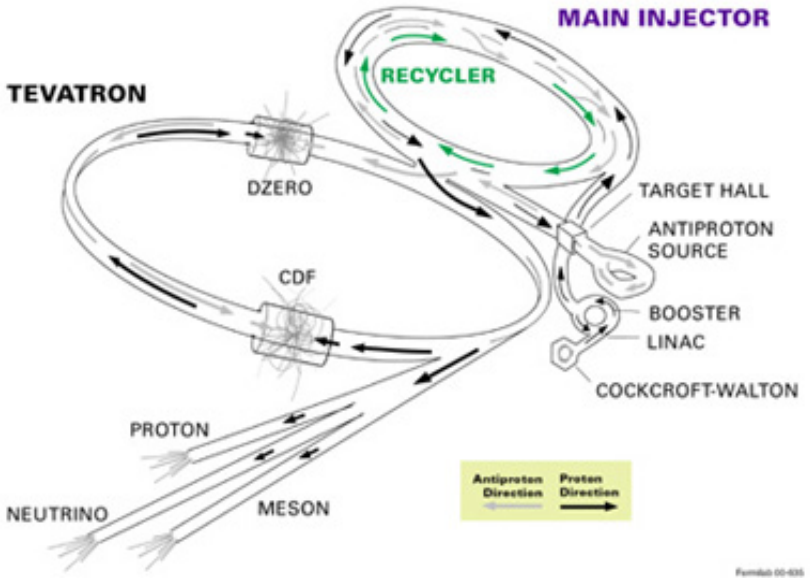

Figure 3.1: **The Fermilab proton/anti-proton acceleration chain.** This diagram depicts stages in the acceleration of p's and $\bar{p}$'s at Fermilab that end with their collision in the Tevatron.

Recent upgrades to the Tevatron have raised the center of mass energy ($\sqrt{s}$) of $p\bar{p}$ collisions from 1.8 TeV, the operating energy of "Run I" (1985-1995), to 1.96 TeV in "Run II"(2001-present). The 160 GeV energy gain significantly increases the cross sections of some physics processes and provides for the potential creation of heavier new particles. The cross section for $t\bar{t}$ production grows by 30% [53], for example, and that predicted for 200 GeV/c^2 sneutrinos increases by 18% [38].

Additional Run II upgrades have increased *instantaneous luminosity*, defined in Section 3.1.3 as a measure of the combined intensity of the p and $\bar{p}$ beams. Larger luminosities reflect a larger number of $p\bar{p}$ interactions and a higher rate of data collection. Run II luminosity gains have been substantial, as is conveyed by the difference in the peak instantaneous luminosity achieved in Run I ($\sim$ 20 x10^{31} cm^{-2}s^{-1}) and that currently in Run II ($\sim$180 x10^{31} cm^{-2}s^{-1}).

3.1.1 Proton Production & Acceleration

Proton/anti-proton collisions at Fermilab are the final stage in a sequence that begins with the generation of negatively charged Hydrogen ions (H^-), formed in the flow Hydrogen gas over a metallic surface. The ions are collected with an electric field applied in the "Cockroff-Walton", an electrostatic accelerator and voltage multiplier that produces a direct current of 750 keV ions. This current is input to a linear accelerator (linac) that consists of a series of radio-frequency (RF) cavities that create strong, alternating electric fields. H^- acceleration is achieved using cavities of increasing length and separation so that ions traversing the linac encounter an electric field of the same orientation in every cavity. The H^- beam is segmented into bunches before entering the linac in order to maximize the number of ions that are in phase with the RF frequency of the cavities, and therefore subject to acceleration.

Bunches emerge from the linac at 400 MeV and are stripped of electrons. The resulting protons are accelerated to 8 GeV in the "Booster", a $\sim$75 m radius synchrotron. Protons from the Booster undergo further acceleration in the "Main Injector". This $\sim$530 m radius synchrotron functions in two operational modes. In one, proton bunches from the Booster are accelerated to 150 GeV before their delivery to and final acceleration in the Tevatron. Alternatively, bunches intended for use in the production of $\bar{p}$'s are accelerated to 120 GeV and sent to a fixed target as described below.

3.1.2 Anti-Proton Production & Acceleration

The production and acceleration of $\bar{p}$'s are the most technically challenging stages of the collision sequence. As is illustrated in Figure 3.2, anti-protons are created by aiming 120 GeV protons from the Main Injector at a nickel target [39]. This

produces a spray of $\bar{p}$'s and other particles that are collected with a solid-core Lithium "lens". The 650 kA current in this 3 cm^2 $\times$ 15 cm cylindrical device generates a magnetic field (1000 T/m gradient) that focuses the particle beam. Anti-protons are then filtered from the beam as they traverse the field of a "Bend Magnet" that serves as a charge-mass spectrometer.

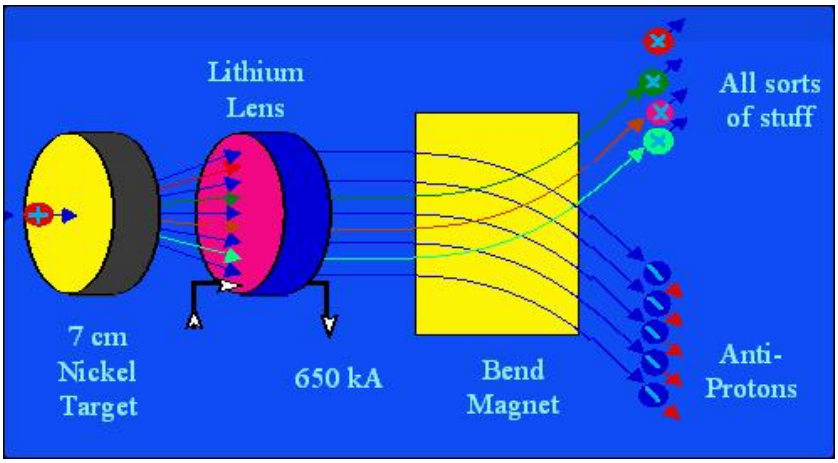

Figure 3.2: **Anti-proton production.** Anti-protons and other particles are produced as a high-energy beam of protons strikes a nickle target. A Lithium lens focuses the beam and the $\bar{p}$'s are separated using a magnetic field.

Anti-protons that emerge from the magnet retain the bunch structure of the original protons but are more widely distributed in energy. Subsequent acceleration stages require a uniform energy distribution and the $\bar{p}$'s must be "debunched" and "cooled" in order to ensure a smaller energy spread. The first step in this processes is the bunch "rotation" of the $\bar{p}$'s in the *Debuncher* , a $\sim$ 90m radius triangular synchrotron (Figure 3.3). Anti-protons that enter this ring move into orbits determined by their energy, with higher (lower) energy $\bar{p}$'s assuming a larger (smaller) radius. High energy $\bar{p}$'s overtake those with lower energy in the straight sections of the ring, leading to a difference in arrival time at the RF cavities along the Debuncher's circumference. As such, low and high energy $\bar{p}$'s experience different phases of acceleration in the RF cavities and are accelerated

or decelerated accordingly. This results in a $\bar{p}$ beam that lacks spatial structure and is more uniform in energy than that emerging from the target.

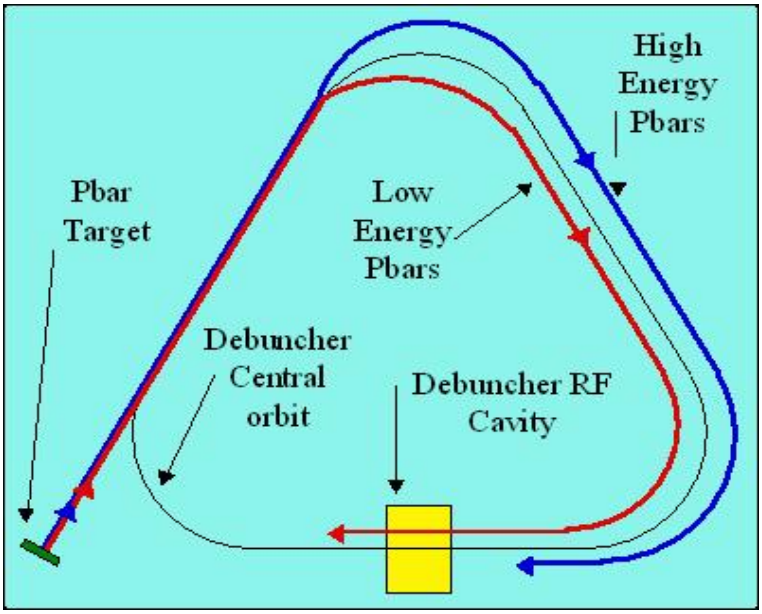

Figure 3.3: **The Debuncher.** The Debuncher reduces the energy spread of anti-protons from the target. Low and high-energy $\bar{p}$'s reach the Debuncher's RF cavities at different times and experience different phases of the accelerating field. As a result, high-energy $\bar{p}$'s are slowed while those with low-energy are accelerated.

Cooling is used to further regulate particle momenta in the direction of beam transport and to diminish momentum components in the transverse direction. Cooling processes reduce *emittance* (ϵ), a quantity that characterizes the spatial extent of a beam. Equation 3.1 shows that the RMS size of a beam, σ, at the collision point is directly related to its ϵ and β^*, a function that describes the envelope of transverse particle trajectories possible in the synchrotron.

$$\sigma = \sqrt{\beta^* \epsilon} \tag{3.1}$$

A central, or "core", beam momentum is maintained through Stochastic cooling. In this technique, illustrated in Figure 3.4, deviations from the ideal $\bar{p}$ orbit are detected at a "pick-up" sensor. The pick-up initiates a compensating impulse

from a "kicker" electrode that corresponds to the average deviation in the orbits. The net force experience by a single particle in the beam at the kicker may be split into two components, the "feedback" that corrects the particle's own errant orbit and the combination of forces meant to correct the orbits of all other particles. Because the orbits of all particles in the beam differ, the forces that comprise this second component are incoherent with respect to a single particle. This component therefore averages to zero and over time each particle experiences only its own damping force. Thus, while no technology is able to distinguish specific particles in the beam, the Stochastic technique allows each particle to be individually cooled to the momentum of the core.

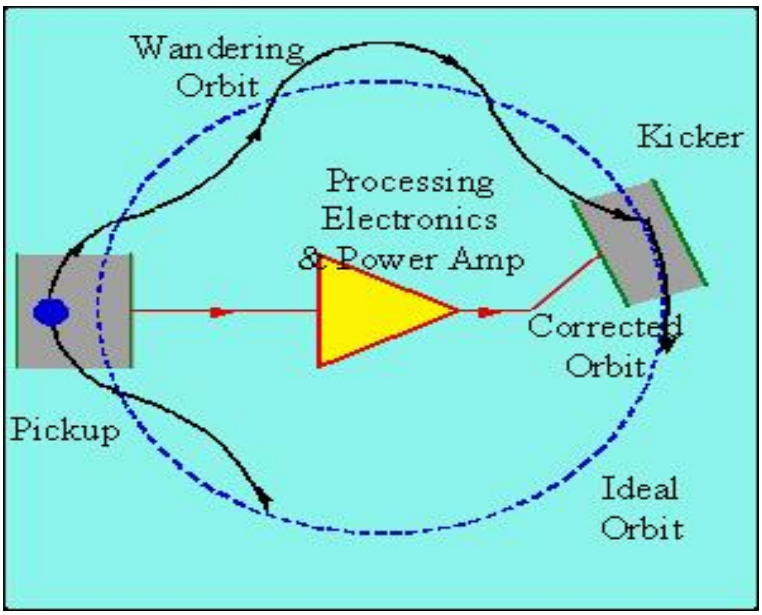

Figure 3.4: **Stochastic Cooling.** Anti-proton beams are cooled in the Accumulator using a system of feedback. Departures from the ideal $\bar{p}$ orbit are detected at the "pickup", inducing compensating pulses from a "kicker" electrode.

The efficiency of Stochastic cooling degrades as the $\bar{p}$ beam current increases [40] and *electron cooling* is employed to further reduce $\bar{p}$ emittance. In this approach, a cooled, mono-energetic beam of electrons is prepared with velocities matching that of $\bar{p}$'s at the desired energy. The electron and $\bar{p}$ beams merge and $\bar{p}$'s of a

greater (lesser) energy than desired will collide with the electrons to lose (gain) momentum. The electrons are heated in this process and separated by magnetic deflection to leave a cooled $\bar{p}$ beam.

Stochastic cooling is employed in the Debuncher to reduce the $\bar{p}$ momentum spread to $< 0.2\%$. The $\bar{p}$'s are then delivered to the *Accumulator*, a triangular synchrotron that fits within the circumference of the Debuncher. Anti-proton generation is a low-yield processes (~ 20 $\bar{p}$'s generated per $\sim 10^6$ incident protons) and $\bar{p}$'s are stored in the Accumulator so that a substantial number can be amassed before their injection to the Tevatron. Anti-protons are accelerated to 8 GeV in the Accumulator and Stochastic cooling is used to maintain a core momentum at this value.

The Accumulator possesses limited storage capacity due to the difficulties associated with cooling a large current of $\bar{p}$'s with Stochastic methods alone. Additional capacity is provided by a fixed-energy (*ie,* non-accelerating) synchrotron, the "Recycler", located above the Main Injector. The Recycler was constructed as part of the Run II Tevatron upgrade and employs electron cooling to further reduce beam emittance. The 4.8 MeV/0.5 A electron beam that cools $\bar{p}$'s in the Recycler is created in the *Pellatron*, a ~ 25 m tall electrostatic generator and accelerator. Nearly all of the electrons used in cooling are collected and recirculated to the Pellatron. Electron-cooled $\bar{p}$'s are sent from the Accumulator to the Main Injector and accelerated to 150 GeV prior to their transfer to the Tevatron.

3.1.3 The Tevatron

Protons and anti-protons undergo final acceleration in the Tevatron, the world's first superconducting synchrotron. At the beginning of a store, an equal number (36) of p and $\bar{p}$ bunches are transfered to the Tevatron from the Main Injector,

forming oppositely circulating bunch trains. A series of 8 RF cavities along a section of the Tevatron's $\sim$6.3 km circumference ramp the bunches to 980 GeV. 816 quadrapole and 204 dipole magnets (4.2 T) respectively focus and steer the beams. The p and $\bar{p}$ bunch trains cross every 396 ns (2.5 MHz) at points central to the CDF II and D0 detectors, resulting in $p\bar{p}$ collisions (or "events") with $\sqrt{s} = 1.96$ TeV. Two systems of quadrapole magnets, 'low-β quads", focus the p and $\bar{p}$ beams to $\sim$35 μm in the transverse plane before they reach the interaction region. A typical Tevatron store continues for $1-2$ days, during which the rate of $p\bar{p}$ collisions decrease to a point where it becomes advantageous to begin the process anew.

Instantaneous luminosity ($\mathcal{L}$ [$\mathrm{cm^{-2}s^{-1}}$]), a quantity related to flux, is a measure of the probability for $p\bar{p}$ collisions in the Tevatron. As shown in Eqn. 3.2, $\mathcal{L}$ depends on the number of bunches in the ring (N_B), the bunch crossing frequency (f) and the number of p's and $\bar{p}$'s per bunch (N_p and $N_{\bar{p}}$). The parameters σ_p and $\sigma_{\bar{p}}$ are characteristic bunch sizes determined from Equation 3.1. Their appearance in the denominator of Eqn. 3.2 supports the intuition that the probability for $p\bar{p}$ interaction should increase with bunch density. F is a form factor that accounts for the shape of the bunches.

$$\mathcal{L} = \frac{\mathrm{N_B n_p n_{\bar{p}} f}}{2\pi\sqrt{\sigma_{\mathrm{p}}^2 + \sigma_{\bar{\mathrm{p}}^2}}} \times \mathrm{F}(\beta^*) \tag{3.2}$$

The time-integral of instantaneous luminosity is *integrated luminosity*, Eqn. 3.3, which represents the total number of $p\bar{p}$ collisions per unit area over a given period.

$$\mathcal{L}_{\mathrm{int}} = \int \mathcal{L}\mathrm{dt} \tag{3.3}$$

3.2 The CDF Experiment

The CDF II detector, depicted in Fig. 3.5, comprises many subdetector systems. Each system performs a specific function in the reconstruction of the particles produced in $p\bar{p}$ collisions. Several of these systems have been upgraded in order to cope with the increased luminosities and event activity experienced in Run II. The following sections describe the CDF II subdetectors that are important in the reconstruction of high-momentum electrons and muons. A more general description of the detector is provided elsewhere [41].

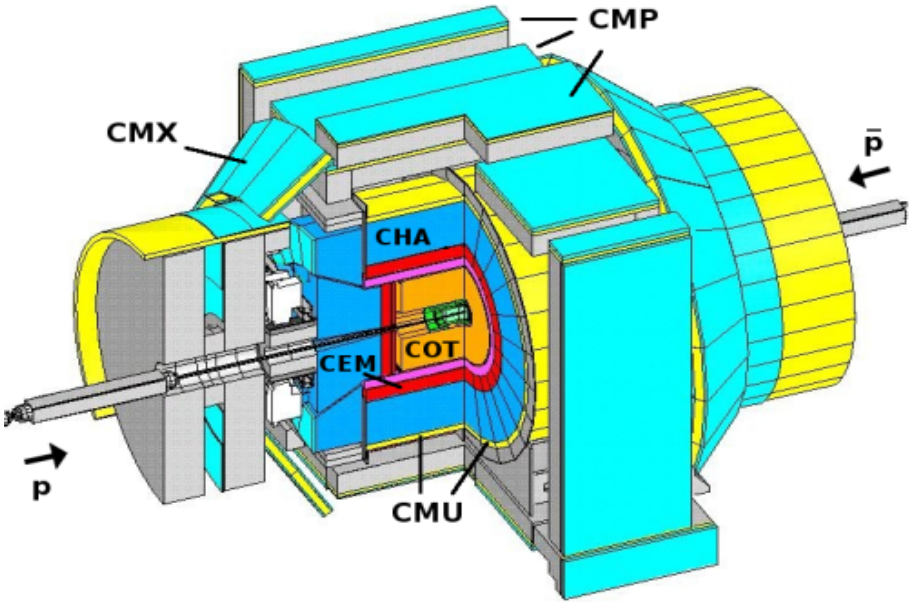

Figure 3.5: **The CDF II Detector.** The detector is built of many subdetectors that contribute to the reconstruction of secondary particles.

The CDF II coordinate system aligns the z-axis in the direction of incident protons and the x-axis toward the interior of the Tevatron. With this convention, spherical and cylindrical systems follow from the usual rules of coordinate transformation. *Pseudo-rapidity*, defined in Eqn. 3.4, is preferred over the spherical θ-coordinate since particle production is an approximately constant function of this quantity.

$$\eta = -\ln(\tan\frac{\theta}{2}) \tag{3.4}$$

3.2.1 Forward Beam Counters

The **CLC** [42], gaseous beam counters at $\theta < 3°$, are used to obtain luminosity estimates. These devices measure the Cerenkov light emitted by charged particles that travel faster than the speed of light in the CLC gas medium. Cerenkov photons are converted to analog signals in photomultiplier tubes (PMT's) located at the end of the detector volume. The CLC detectors are located at small angles relative to the beamline so that inelastic $p\bar{p}$ scattering contributes the dominant source of signal. The cross section for this process (~ 60 mb [43]) is known with small uncertainty and is used together with the measured event rate to obtain an estimate of instantaneous luminosity.

3.2.2 Tracking

Charged particles produced in $p\bar{p}$ collisions at CDF curl in the 1.4 T magnetic field of a 1.5 m radius superconducting solenoid aligned with the z-axis. Their trajectories and transverse momenta (p_T) are reconstructed using measurements from a 1.37 m outer radius open-cell drift chamber, the Central Outer Tracker (**COT**) [44], that sits within. The COT's cylindrical volume contains 30240 axial sense wires, 32760 potential wires and a mixture of argon-ethane gas. Charged particles that traverse the COT ionize molecules of the gas, freeing electrons that drift to the sense wires. An electron generated in an initial ionization gains kinetic energy near a sense wire and produces additional ionization in collisions with gas molecules. The process continues and an "avalanche" of ionized charge develops, inducing a pulse of current as it arrives on a sense wire.

Pulses on the sense wires are recorded by readout chips, the "Amplifier Shaper Discriminator Charge Encoder" [1]. The *ASDQ*s output digital waveforms that encode the amount and drift-time of charge collected on the wires. This information is used to assign position measurements (or "hits") of individual wires to a reconstructed particle trajectory (or "track").

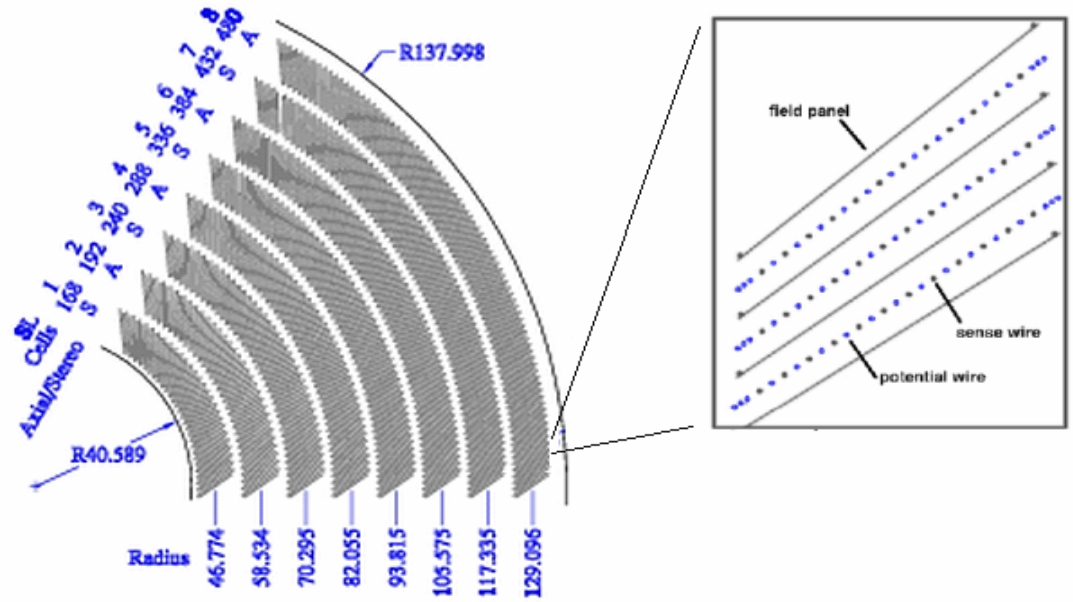

Figure 3.6: **COT superlayers.** COT wires from the 96 ϕ-layers are grouped into cells. The cells form 8 axial and stereo superlayers. Each cell contains 12 sense-wires that collect charge produced from charged particles that traverse the COT.

The $\sim 32K$ COT sense wires are arranged in 96 concentric ϕ-layers. Sense wires from consecutive layers are grouped in twelves to form mechanically and electrostatically isolated "cells" shown in Figure 3.6. Cells are oriented at 35° with respect to the r-direction[2] and make 8 concentric rings in ϕ called *superlayers* (SL0-SL8). Wires in the even-numbered superlayers are strung axially while the rest skew 3° with respect to the z-direction. These "stereo" wires provide information on the z-position of a track since the drift distance to such a wire

[1]The ASDQ's were designed and tested at the University of Pennsylvania.
[2]This *Lorentz angle*compensates for the deflections caused by the magnetic field

grows with increasing z-coordinate.

The COT provides ~ 140 μm single hit, $r-\phi$ position resolution. Its measurements are used in track reconstruction software that determines the p_T of charged particles with an accuracy[3] of $\frac{\delta p_T}{p_T} \simeq (0.15\%) \times p_T$. Track z-positions, reconstructed using information from the stereo layer, are determined with an accuracy of $\sim$5 mm.

3.2.3 Time Of Flight

The CDF "Time Of Flight" (**TOF**) system [45] is used primarily to distinguish between low momentum kaons and pions. We use TOF to identify muons from cosmic-rays, which present an irreducible background in our search. The TOF detector[4] consists of bars of scintillator that form a thin cylinder between the outer radius of the COT and the inner radius of the solenoid. Photomultiplier tubes (PMT's) connected to the ends of the bars record the arrival time of particles at the scintillator with an accuracy of 5 ps. Cosmic-ray muons that pass through the volume contained by the system show a characteristic difference in the detection times measured in upper and lower TOF bars. This difference, $t_{\text{upper}} - t_{\text{lower}} \simeq 280$ cm/c $\simeq -10$ ns, is easily resolved by the TOF detector.

3.2.4 Calorimetry

Outside of the COT and solenoid lie the central electromagnetic (**CEM**) [46] and hadronic (**CHA**) [47] calorimeters.[5] These devices measure the energy of particles that shower within their volume. The development of an electromagnetic

[3]Better position resolution is achieved by adding measurement from the CDF II silicon tracker, which is not discussed here.

[4]The University of Pennsylvania contributed to the development of the TOF detector and readout electronics.

[5]The University of Pennsylvania contributed to the calibration of the CEM.

shower results from the joint processes of bremsstrahlung and electron-positron pair production. Charged particles emit photons as they are slowed by interactions with atomic nuclei. High-energy photons can form energetic e^+e^- pairs (in the presence of matter) that radiate additional photons. These processes continue (resulting in the formation of an electromagnetic shower) until the energies of the photons produced fall below that required for additional pair-production. The initiation of an electromagnetic shower is a probabilistic process; the average amount of material needed to reduce the energy of an electron beam to $\frac{1}{e}$ of its initial value ($\sim$37%) is termed a "radiation length".

The CEM covers the range $|\eta| < 1.0$ and is constructed of 31 layers of scintillating plastic interspersed with layers of 3.4 mm thick lead. The combined lead-scintillator layers constitute 19 radiation lengths. Showers in the lead layers excite organic molecules in the plastic that emit photons as they return to their ground-state. Blue light emitted from the scintillator is shifted to green using organic plastics (wavelength shifters) and guided to PMT's. The amount of light collected on a PMT is used to determine the energy of an incident, showering particle.

A thin, 2-dimensional proportional chamber, the **CES** [46], is located at the position of maximum shower development for electrons ($\sim$ 6 radiation lengths). This device provides a $\eta - \phi$ position measurement of electromagnetic showers. Hits on the azimuthal strips and longitudinal wires of the CES are clustered and compared with test beam profiles to assign an overall shower position.

The electromagnetic sections of the central calorimeter are followed by hadronic compartments built of 32 layers of 2.5 cm thick iron alternating with scintillator. Hadronic showers develop from a progression of inelastic collisions between hadrons and atomic nuclei. The CHA layers constitute 5.5 nuclear absorption lengths, or 5.5 times the mean path for an inelastic collision. The particles pro-

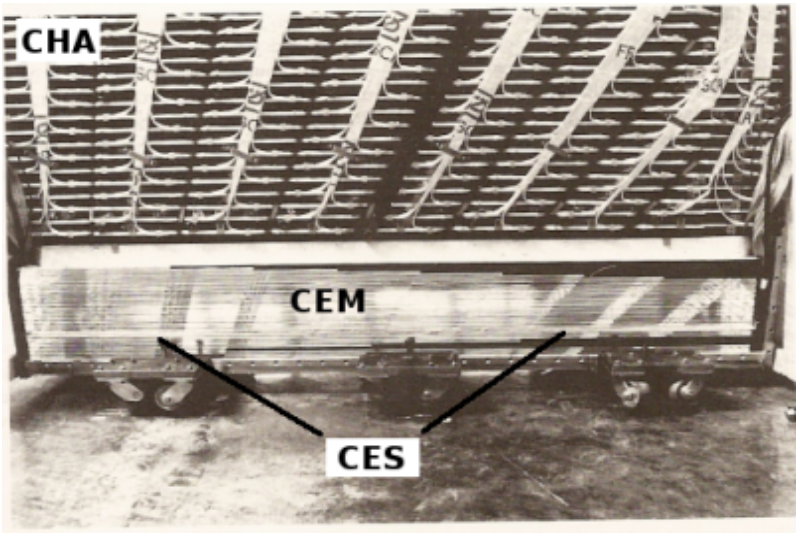

Figure 3.7: **Central Calorimeters.** This picture shows the electromagnetic and hadronic compartments of a central calorimeter wedge. The wedge is divided into 10 η-projective towers (only 8 CHA towers are visible in the figure). A thin proportional chamber, the CES, is embedded within the electromagnetic calorimeter to resolve electromagnetic shower positions.

duced in a hadronic shower, like those generated in an electromagnetic shower, will interact with molecules of scintillating plastic to generate light. Light produced in the scintillating layers of the CHA is likewise detected with PMT's and the measured light yield is related to the initial energy of the showering hadron.

The central calorimeter systems are divided amongst four arches. Each arch is segmented into 12 ϕ-wedges that are further split into 10 η-projective towers. Towers span 0.1 in η, 15° in ϕ and define the spatial resolution of the calorimeters[6]. Figure 3.7 depicts the CEM and CHA compartments and the 10 towers of a wedge. The energy resolution of the CEM is $\sigma(E)/E = 0.135/\sqrt{E_T} \oplus 1.5\%$. That of the CHA is $\sigma(E)/E = 0.5/\sqrt{E_T} \oplus 3\%$.

[6]The CES provides position measurements of electromagnetic showers that are more precise (2 mm resolution).

3.2.5 Muon Chambers

Muons do not undergo bremsstrahlung to the same extent as electrons (due to their larger mass) and interact with matter primarily through the process of ionization. As such, muons do not deposit significant energy in the CDF II calorimeters and are distinguished at CDF as charged particles that persist after a significant number of radiation and interaction lengths. Muons are detected using gas-proportional chambers that lie outside of the CHA's 5.5 interaction lengths of iron. As described in Section 3.2.2, high-energy charged particles ionize gas molecules to produce "tracks" of ionization. The muon chambers used at CDF collect this charge on senses wires, enabling the reconstruction of short track segments ("stubs") that are matched with tracks extrapolated from the COT. This analysis uses muon stubs identified in the CDF II central muon systems, the **CMU** [48] and **CMP** at $|\eta| \lesssim 0.6$ and the **CMX** between $0.6 \lesssim |\eta| \lesssim 1.0$ [49].

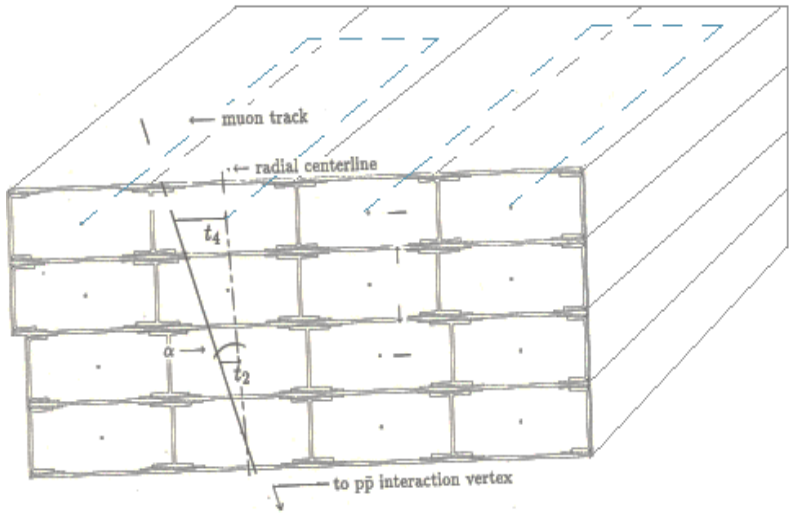

Figure 3.8: **CMU Muon Chambers.** Sense wires (dashed lines) shared between neighboring cells of the CMU detectors provide z-position measurements through charge division. Cells are stacked in the radial direction and allow four $r-\phi$ position measurements.

The CMU chambers border the outer radius of the CHA and ring the central

calorimeter in ϕ. The system is constructed of 6.35 cm $\times$ 2.68 cm $\times$ 226 cm cells that contain argon-ethane gas and a high-voltage sense wire. Sense wires are shared between two cells that neighbor in ϕ, as shown in Figure 3.8. Current pulses on the wire are digitized by readout chips at the ends of both cells. Differences in the arrival times and amplitudes of pulses at the two ends of the same wire give an indication of the z-position of the incident muon. CMU cells are stacked four-deep to yield four independent radial position measurements. The CMU chambers provide single hit, $r - \phi$ position resolution of 0.25 mm. The charge division technique used to reconstruct a z-position provides an accuracy of 1.2 mm.

Beyond the CMU chambers lies an additional 60 cm of steel shielding and another set of muons chambers, the CMP. The CMP is constructed of cells similar to those of the CMU although the system is not ϕ-symmetric however and each cell possesses an independent sense wire. Finally, the CMX muon chambers, of nearly identical construction to those of the CMP, extend the η coverage of muon detection. The CMX cells are arranged in cones at both ends of the CDF II detector. $r - \phi$ hit resolution for the CMP and CMX systems are similar to that of the CMU.

3.2.6 Trigger Systems and Data Logging

CDF employs a three-tiered trigger system to reduce the rate of data read out from the detector and to enrich this data with events that contain evidence of rare or interesting physics. On average, the data used to describe a single event at CDF in Run II is $\sim$ 150 kB. Without a trigger system, the readout rate would be determined by the beam crossing frequency, 1.7 MHz, leading to a theoretical data output of 2.6 x10^5 MB/s. Data transfer rates of this magnitude

are unsustainable.

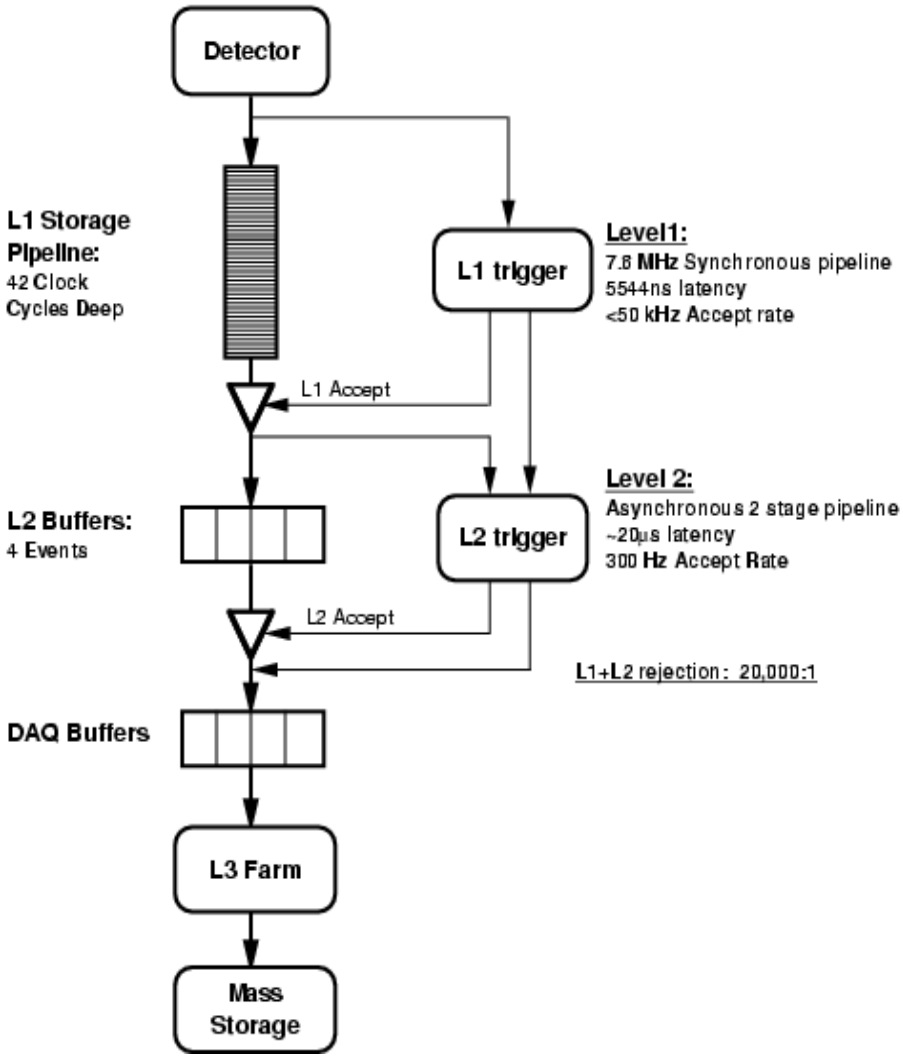

Figure 3.9: **The CDF Trigger System.** Selections imposed at each of the three CDF trigger levels reduce readout rates and enrich data with interesting events.

The trigger is not a discrete subdetector system like those described in previous sections. Rather, it is a combination of hardware and software systems (sketched in Figure 3.9) that gather information from subdetectors and use this information in assessing the potential physics content of events. The **Level-1** trigger is incorporated in the readout electronics of subdetector systems and determines, through comparison with preloaded trigger criteria (thresholds, coin-

cidence counts, *etc.*), whether an event merits further consideration. The Level-1 system operates synchronously and issues decisions to the *Trigger Supervisor* (TS), custom electronics that broadcast decisions over VME backplanes to all subdetector systems. On Level-1 accept (L1A), event data are loaded into one of four memory buffers implemented in each of the subdetectors. Information is fetched asynchronously from the buffers by the **Level-2** trigger system upon receipt of L1A.

The Level-2 trigger [50] consists of a PC running Linux[7] and a number of VME modules, **PULSAR**s, that collect event information from the L1 subdetectors. Several PULSARs are needed to interface with the multiple output channels of the L1 systems. Individual PULSARs merge data received from these systems into formatted packets that are transmitted over optical links to the PC. The PC uses the formatted data to partially reconstruct events and to evaluate a set of software-based trigger algorithms. Upon completion of the algorithms, the PC returns a L2 decision to another PULSAR that communicates with the TS. The TS relays the decision to the other tiers of the trigger system. If an event is accepted at L2, the L1 data from all subdetectors are sent to the **Level-3** system (L3).

The L3 trigger [51] is an array of ~ 250 PC's running Linux. If accepted at L2, event data from all CDF II subdetectors are sent through a network switch. The switch routes the data from individual events to separate L3 PC's. The machines fully reconstruct events, performing detailed tracking algorithms, calorimeter shower modeling, muon stub finding, *etc.* The reconstructed event information is used in the evaluation of a final set of trigger algorithms. If the event passes the L3 trigger requirements, the system outputs the reconstructed event data for permanent storage on tape. Stored data is used in offline repro-

[7]The University of Pennsylvania developed the PC system used in the L2 trigger.

cessing to build software data structures that represent reconstructed "physics objects" (*eg*: electrons, muons and jets). These objects are the starting point of physics analyses at CDF.

The selections applied at each level of the trigger limit the output of data to rates that subsequent stages are able to accept. Processing at L1 is hardware based and fast enough to keep pace with the beam crossing rate of 2.5 MHz. The designed maximum L1 output to L2 is 50 kHz. The L2 trigger thus has $\sim 20 \mu s$ to return a decision so that hardware memory buffers are available to accept data following the next L1A. The L2 system is designed to issue accepts at a maximum rate of $\sim$300 Hz. This rate is determined from the requirements of the L3 system, which can send data to storage at a rate of $\sim$100 Hz, or $\sim$50 MB/s.

Chapter 4

Event Selection

4.1 Datasets & Trigger Requirements

The first step in our selection of events for the $e\mu$ search is the determination of datasets and Monte Carlo samples. CDF datasets are collections of reconstructed events that pass the requirements of trigger paths (sets of L1, L2 and L3 triggers). In selecting events accepted by particular triggers, we limit the processing of events to those that will not trivially fail the selection criteria we apply in the analysis. We model the expected Standard Model background content of the datasets using samples of events generated with Monte Carlo techniques. We generate additional Monte Carlo samples to assess potential contributions from LFV signals.

4.1.1 High-p_T Lepton Datasets

Our search utilizes data from the inclusive, high-p_T lepton datasets, *bhel0d* and *bhmu0d*. These are the respective products of the CEM18 and CMUP18 / CMX18 trigger paths. The triggers select events that satisfy the requirements listed in

Table 4.1. Accepted events contain at least one high-E_T electron candidate with energy depositions in the CEM calorimeter (a CEM "cluster") or a high-p_T muon candidate with stubs in the CMU and CMP or CMX muon chambers. p_T refers to the transverse momentum of a COT track matched to either a CEM cluster or a muon stub and E_T represents the transverse energy ($E\sin\theta$) of a CEM cluster. p_T^{CMU} and p_T^{CMX} are momenta determined from corresponding muons stubs. Other quantities listed in Table 4.1 are explained in Section 4.2.

Trigger Level	**CEM18**	**CMUP18**	**CMX18**
Level 1	$E_T \geq 8$ GeV $p_T \geq 8$ GeV/c $Had/Em \leq 0.125$	$p_T^{CMU} > 6$ GeV/c CMP stub $p_T \geq 4.1$GeV/c	$p_T^{CMX} > 6$ GeV/c $p_T \geq 8.3$GeV/c
Level 2	$E_T \geq 16$ GeV $p_T \geq 8$ GeV/c $Had/Em \leq 0.125$ $\eta \leq 1.32$	$p_T \geq 8.3$ GeV/c CMU stub CMP stub	$p_T \geq 10.1$ GeV/c CMX stub
Level 3	$E_T \geq 18$ GeV $p_T \geq 9$ GeV/c $Had/Em \leq 0.125$ $L_{shr} \leq 0.2$ $\chi^2_{strip} \leq 20$ $\Delta Z_{cem} \leq 8$ cm	$p_T \geq 18$ GeV/c $\Delta X_{CMU} \leq 10$ cm $\Delta X_{CMP} \leq 10$ cm	$p_T \geq 18$ GeV/c $\Delta X_{CMX} \leq 10$ cm

Table 4.1: **High-p_T Lepton Trigger Requirements.** The CEM and CMUP/CMX trigger paths require events that meet several hardware and reconstructed-event criteria. Events passing all levels of a trigger path enter a corresponding dataset, bhel0d (CEM18) and/or bhmu0d (CMUP18/CMX18).

The high-p_T electron and muon datasets were collected over the period 03/2002-08/2004. Both datasets are processed with version 5.3.3_nt of the CDF offline

production software and have been reformatted as *TopNtuples* . TopNtuples are data structures distilled from reconstructed event information. The ntuples are output from an inclusive lepton filter in the "TopFind" software module that takes reconstructed events as input. The filter applies a loose subset of the full lepton identification cuts described below. The cuts in TopFind are fully efficient with respect to our event selection and allow us to obtain ntuples of manageable size.

We choose events from the high-p_T datasets based on electron and muon "goodrun lists". The lists indicate operational periods in which the CDF II detector systems that are important for the reconstruction and triggering of high-p_T leptons are known to have functioned properly. The total $\mathcal{L}_{\rm int}$ for the good runs in the *bhel*0*d* and *bhmu*0*d* datasets are 369.6 pb^{-1} and 357.0 pb^{-1} respectively. We select events for the high-p_T $e\mu$ search that are marked "good" for both electrons and muons. This results in a dataset of slightly smaller integrated luminosity (344 pb^{-1}).

4.1.2 Monte Carlo Samples

The leptonic decays of $Z/\gamma^* \to \tau\tau$ (Drell-Yan), top/anti-top ($t\bar{t}$), and dibosons (WW, WZ and ZZ) are important physics backgrounds in our search. We model these processes using samples of events generated with the PYTHIA Monte Carlo (MC) generator [52]. We provide Feynman diagrams of the processes in the following chapter. Table 4.2 lists the samples, their sizes and corresponding production cross sections (σ). As will be described in Section 5.1, we use the various σ's and the numbers of MC events that pass our selection criteria to determine the expected Standard Model background in the 344 pb^{-1} dataset.

The cross sections given for $t\bar{t}$ [53] and diboson [54] production are the next-to

leading order (NLO) values. A top quark mass (m_{top}) of 178 GeV/c^2 is used in generating the $t\bar{t}$ sample. The cross section listed in Table 4.2 for the Drell-Yan process $p\bar{p} \to Z/\gamma^* \to \tau\tau$ is the next-to-next leading order (NNLO) value for continuum ($M_{ll} > 30$ GeV/c^2) production. This is obtained by scaling the PYTHIA leading order cross section by the ratio of NNLO to LO predictions obtained from PHOZPR calculations [55]. We apply a lepton filter (efficiency = 13.65%) while ntupling the *ztop4i* sample to reduce its size. We employ two additional Drell-Yan samples, *ztop2i* and *ztop0i*, in checks of our lepton identification procedure that we describe in Section 5.2.

Process	**Sample**	N_{events} ($\times 10^6$)	σ (pb^{-1})
$Z/\gamma^* \to \tau\tau$	ztop4i	1.4	337.7 (NNLO)
$t\bar{t}$	ttopel	1.2	6.1 (NLO)
WW	wtop1w	0.4	12.1 (NLO)
WZ	wtop1z	0.4	3.7 (NLO)
ZZ	ztopcz	0.4	1.4 (NLO)
$Z/\gamma^* \to ee$	ztop2i	1.0	230.6 (LO)
$Z/\gamma^* \to \mu\mu$	ztop0i	2.0	234.2 (LO)

Table 4.2: **Monte Carlo Background Samples.** We use PYTHIA generated event samples to model the SM backgrounds in our search. The cross sections listed are used to scale the event yields measured in the samples to predictions for our 344 pb^{-1} dataset. The *ztop2i* and *ztop0i* samples are used in tests of our lepton identification procedure.

We use PYTHIA generated MC samples of Higgs events, $d\bar{d} \to H \to e\mu + \text{H.C.}$, to model $\tilde{\nu}_\tau$ production and LFV decay. The Higgs is forced to an oppositely charged electron-muon final-state by modification of the PYTHIA decay table. We generate nine samples of 10K events that correspond to different $\tilde{\nu}_\tau$ masses (50, $100 - 800$ GeV/c^2). Because the signal model we consider for $\tilde{\nu}_\tau$ production

assumes the narrow resonance approximation [56], we specify a constant Higgs width that is smaller than our experimental resolution.

Nine additional samples are used to model the LFV decay of the Z' over the same range of masses. We select the PYTHIA $p\bar{p} \to Z'$ production process and exclude contributions from Z/γ^*. As explained in Section 2.3, we consider LFV decays in which the Z' couples to left-handed fermions and specify such couplings for $e\mu$ using the PYTHIA input menu. We set Z' couplings to other fermions to zero.

All MC samples (both SM and signal) are generated with PYTHIA version 6_216 and input to a GEANT3 [57] based simulation of the CDF II detector. These simulations use the CTEQ5L [58] parton distribution functions (PDF's) to model the momentum distribution of the initial state partons. Simulated detector output is processed by the same CDF offline reconstruction software that is used to process actual data recorded by the detector. Since our analysis relies on few and relatively simple triggers, we do not simulate the response of the CDF trigger system. Instead, we emulate the effect of the trigger in Monte Carlo by weighting the event yields by factors, f_{trig}, that represent the probability for passing at least one of the high-p_T lepton triggers. The specific factors we apply are listed in Table 4.3. These correspond to the four types of reconstructed muon used in the analysis and are combinations of the efficiencies[1] of individual triggers.

4.1.3 Jet E_T Datasets

We estimate background due to the misidentification of jets as leptons using data collected with jet-E_T triggers. We use four datasets, $gjt10d$, $gjt20d$, $gjt30d$ and $gjt40d$ that correspond to E_T thresholds of 20, 50, 70 and 100 GeV respec-

[1]Values for the trigger efficiencies are 0.96 (CEM18), 0.908 (CMUP18) & 0.965 (CMX18)

Electron type	**Muon type**	**Trigger**	ϵ_{trig}
CEM	CMUP	CEM18‖CMUP18	.9996
CEM	CMX	CEM18‖CMX18	.9998
CEM	CMU	CEM18	.9660
CEM	CMP	CEM18	.9660

Table 4.3: **Trigger Efficiency Scale Factors.** These factors represent the probability for events of a particular $e\mu$ category to pass the associated trigger(s). They are used to correct our Monte Carlo event yields for the effect of the trigger selection in data.

tively. Other requirements imposed by the jet triggers are listed in Table 4.4. Section 5.1.2 discusses the methods we use to calculate lepton misidentification probabilities from these datasets.

4.2 Lepton Identification

We identify electrons and muons through the application of standard CDF high-p_T lepton identification (ID) cuts detailed in [59]. These cuts distinguish electrons and muons from the larger set of reconstructed objects to which they belong. The CDF production software reconstructs all objects that possess a found CEM cluster, for example, as members of the *CdfEmObject* class. Of such objects (*eg:* photons, electrons and jets), only those that satisfy the electron ID requirements have characteristics similar to test-beam electrons. Likewise, every COT track with $p_T > 10$ GeV/c is a member of the *CdfMuon* class. Muon ID requirements enable the selection of candidates with additional "muon-like" qualities from the set of generic CdfMuon objects.

We provide summaries of the ID cuts in Tables 4.5 and 4.6. The criteria listed in the tables are used to identify electrons and muons in both data and MC

Level	**gjt10d**	**gjt20d**	**gjt30d**	**gjt40d**
Level 1	$E_T \geq 5$ GeV	$E_T \geq 5$ GeV	$E_T \geq 10$ GeV	$E_T \geq 10$ GeV
Level 2	$E_T^{seed} \geq 3$ GeV $E_T^{side} \geq 1$ GeV $E_T \geq 15$ GeV	$E_T^{seed} \geq 3$ GeV $E_T^{side} \geq 1$ GeV $E_T \geq 40$ GeV	$E_T^{seed} \geq 3$ GeV $E_T^{side} \geq 1$ GeV $E_T \geq 60$ GeV	$E_T^{seed} \geq 3$ GeV $E_T^{side} \geq 1$ GeV $E_T \geq 90$ GeV
Level 3	$Isol \leq 0.7$ $E_T \geq 20$ GeV	$Isol \leq 0.7$ $E_T \geq 50$ GeV	$Isol \leq 0.7$ $E_T \geq 70$ GeV	$Isol \leq 0.7$ $E_T \geq 100$ GeV

Table 4.4: **JetE_T Trigger Requirements.** The jet-E_T trigger paths select events based on several hardware and reconstructed-event criteria. Events passing all levels of a trigger path enter a corresponding dataset.

generated events. The remaining portion of this section describes the individual ID requirements.

The *DefEmObject* electron ID cut requires that the CEM cluster of an electron candidate be matched to an extrapolated COT track. The *Fiducial* and Z_0^{trk} requirements ensure that electron candidates are reconstructed in instrumented regions of the detector. L_{shr} refers to the lateral spread of electromagnetic showers over adjacent calorimeter towers. Test-beam studies with the CEM calorimeter have provided the optimal cut value for this quantity. We cut on ΔX_{CES} and ΔZ_{CES} to require that shower positions measured by the CES detector match those of extrapolated COT tracks. $\chi^2_{strip} < 10$ demands that clusters found in the CES are consistent with those obtained in test-beam studies.

We additionally require that electron candidates deposit most of their energy in the CEM (E_{Had}/E_{EM} is small) and do not radiate energetic photons before reaching the calorimeter ($E/P < 2$). We remove conversion electrons by vetoing

Quantity	**Requirement**
DefEmObject	true
Region	CEM
Conversion	false
Fiducial	true
E_T	$\geq$ 20 GeV
p_T^{trk}	$\geq$ 10 GeV
$\mid Z_0^{trk} \mid$	$\leq$ 60 cm
Track Axial Segments	≥ 2
Track Stereo Segments	≥ 2
E_{Had}/E_{Em}	$\leq (0.055 + (0.00045 \times Energy))$
E/P	$\leq 2.0 \parallel P_T \geq$ 50 GeV
$\mid Z_0^{trk} \mid$	$\leq$ 60 cm
$\mid \Delta Z_{ces} \mid$	$\leq$ 5 cm
$Q \times \Delta X_{ces}$	-3 cm $\leq$, $\leq$ 1.5 cm
L_{shr}	≤ 0.2
χ^2_{strip}	≤ 10
Isolation	≤ 0.1

Table 4.5: **Electron Identification Cuts.** High-p_T electron ID cuts and their values.

candidates that form a pair with nearly parallel trajectories originating from a common vertex, which signifies a parent particle of negligible invariant mass. Finally, we require electron candidates to have isolated energy depositions in the CEM in order to suppress jet backgrounds. The "Isolation" criteria listed in Table 4.5 rejects electron candidates with more than 10% of their energy in a 0.4 radius $\eta - \phi$ cone around the seed cluster.

We consider four categories of muon candidates, those with tracks matched to stubs in the CMU, CMP or CMX chambers or matched to stubs in both the CMU and CMP chambers ("CMUP" muons). Several of the cuts described for electron candidates also apply to muons. In addition, we impose a number of quality requirements on the matching of extrapolated COT tracks to muon stubs. We

Quantity	Requirement
DefMuonObject	true
p_T	$\geq$ 20 GeV
E_{Had}	$\leq max(6., 6. + 0.0280 \times (P - 100.))$
E_{Em}	$\leq max(2., 2. + 0.0115 \times (P - 100.))$
$\mid Z_0^{trk} \mid$	$\leq$ 60 cm
Track Axial Segments	$\geq$ 3
Track Stereo Segments	$\geq$ 3
$\mid D_0 \mid$	$\leq$ 0.20 if TrackSiHits==0 $\leq$ 0.02 if TrackSiHits > 0
Isolation	$\leq$ 0.1
$\mid \Delta X_{cmu} \mid$	$\leq$ 3.0 cm if CMUP, CMU
$\mid \Delta X_{cmp} \mid$	$\leq$ 6.0 cm if CMUP, CMP
$\mid \Delta X_{cmx} \mid$	$\leq$ 6.0 cm if CMX
$\mid \rho(\eta, Z_0, 155) \mid$	$>$ 140 cm if CMX

Table 4.6: **Muon Identification Cuts.** High-p_T muon ID cuts and their values.

also cut on the impact parameter (D_0) of a muon candidate in order to reduce cosmic-ray backgrounds and require that timing information from the TOF detector is consistent with muon candidates originating from the interaction region. The L1 XFT trigger (part of the CMX18 trigger path) indirectly constrains the trajectories of CMX muon candidates in data by requiring four axial track segments. We impose this constraint in MC by requiring that the radius at which CMX candidates exit the COT (ρ) be larger than 140 cm. Finally, we require that hadronic and electromagnetic calorimeter energies are small so that muon candidates are consistent with minimum ionizing particles.

The efficiency of lepton identification and reconstruction differs in data and MC. We account for this difference by applying scale factors ($\epsilon_{ID/reco}$), listed in Table 4.7, to the event yields found in Monte Carlo [59].

Lepton Type	$\epsilon_{ID/reco}$
CEM	0.996
$CMUP$	0.930
CMX	1.002
CMU	0.923
CMP	0.950

Table 4.7: **Lepton Reconstruction/ID Scale Factors.** These factors are used to scale the lepton ID and reconstruction efficiency in Monte Carlo to the corresponding values in data.

4.3 Event-Level Cuts

We impose several event-topology criteria that require reconstructed events to be consistent with direct LFV decay. We consider events with at least one electron and one muon candidate that pass the lepton ID criteria described above. Next, we select electrons and muons of opposite charge and choose the highest-p_T $e\mu$ pair in events that contain several combinations of identified leptons. Last, we require the absolute difference between a pair's Z_0^{trk} to be less than 5 cm to ensure that the leptons originate from a common $p\bar{p}$ interaction.

Chapter 5

Analysis Techniques

We search for evidence of LFV decays to $e\mu$ in the 344 pb^{-1} high-p_T lepton datasets. Our approach involves the application of the selection criteria described in the previous chapter to events in data. To determine whether the result supports the discovery of an LFV signal we first calculate potential signal yields and the expected contributions of backgrounds to our pool of selected events. We perform several cross-checks that validate our event selection procedure before comparing these estimates with observation. Finally, we establish techniques that allow us to set 95% confidence level upper limits on the cross section times branching ratios of LFV processes and discuss the uncertainties that influence this result.

5.1 Event Yields

We obtain signal yields in Section 5.1.1 and SM background expectations in Section 5.1.2 using *acceptances* (α), defined as the ratio of the number of selected events in a MC sample to the number of events generated. We determine the efficiency of our event selection in data by scaling the MC acceptances with the

scale factors $f_{reco/ID}$ and f_{trig} described in the previous chapter. This provides a total corrected acceptance for each process, α_{tot}, that we use with corresponding cross section times branching ratios ($\sigma \times \mathrm{Br}(\mathrm{e}\mu)$) and the integrated luminosity of our dataset to calculate event yields:

$$N_{exp} = (f_{trig} \cdot f_{reco/ID}) \cdot \alpha_{tot} \cdot (\sigma \times \mathrm{BR}) \cdot \mathcal{L}_{\mathrm{int}} \tag{5.1}$$

As we discuss in Section 5.1.2, background from misidentified lepton candidates are estimated using probabilities calculated in data rather than with MC acceptances. We depend on data to obtain an accurate estimate of number of "fake" leptons in our sample because the processes that give rise to this background are not well modeled with Monte Carlo.

5.1.1 Signal Monte Carlo

We categorize events selected from the $\tilde{\nu}_\tau$ samples by the type of identified muon (CMU,CMP,CMUP,CMX) they contain. The numbers of events in each muon category are used to calculate a corresponding set of $\alpha' s$, that we correct using the appropriate $f_{reco/ID}$ and f_{trig} scale factors. We combine the scaled α's of each muon category to obtain a total corrected acceptance (α_{tot}) at each generated $\tilde{\nu}_\tau$ mass. We then fit the α_{tot}'s from the nine $\tilde{\nu}_\tau$ samples to a curve, shown in Figure 5.1, that parameterizes corrected acceptance as a function of $\tilde{\nu}_\tau$ mass.

We follow the same procedure in the calculation of the acceptance function for $p\bar{p} \rightarrow Z' \rightarrow e\mu$ shown in Figure 5.1. The apparent difference in the Z' acceptance curve with respect to that for $d\bar{d} \rightarrow \tilde{\nu}_\tau \rightarrow e\mu$ arises from our assumption of pure, left-handed fermionic Z' couplings. Figure 5.2 sketches the Z' production and decay processes. The Z' is produced predominantly polarized, its spin aligned with the z-axis on account of the left-handed quark and right-handed anti-quark

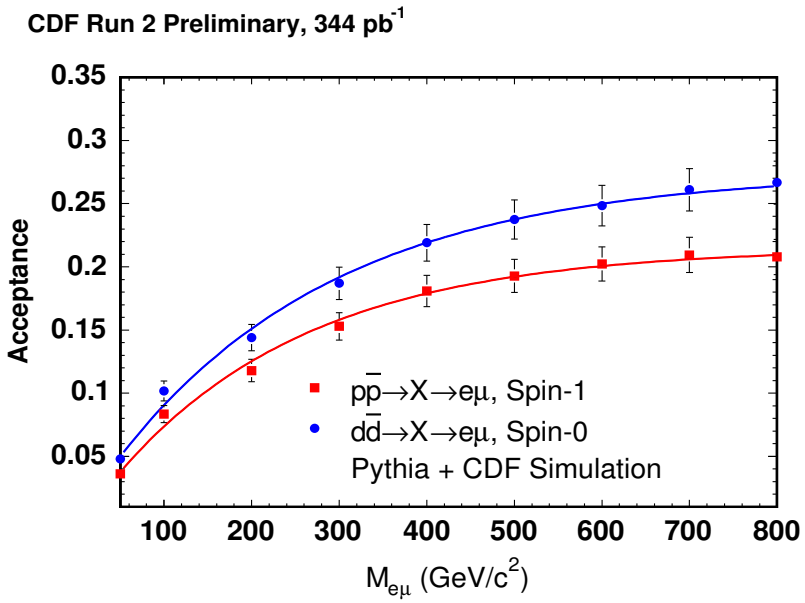

Figure 5.1: **Signal Acceptance.** Z' acceptances are smaller than those for $\tilde{\nu}_\tau$ because of a difference in the angular distributions of the $e\mu$ decay products.

from which it is generated. Because orbital angular momentum is zero in the Z' rest frame, the total angular momentum (J) in this frame is $1\hbar$.

The $e\mu$'s from Z' decay must also be produced in a $J = 1\hbar$ state for angular momentum to be conserved. Because the final-state (anti-)leptons to which the Z' couples are also left(right)-handed, their spins align with the axis of their emission in the Z' rest frame. For instance, the $e\mu$ form a state with J and z-component J_z equal to $1\hbar$ when emitted along the z-axis. The probability for an electron and muon in this angular momentum state to be emitted at angle θ^* with respect to the z-axis (see Figure 5.2, right) is given by the square modulus of the $d^1_{1,1}$ rotation matrix [60]. Thus, like leptons in W decay, the $e\mu$ decay products in the Z' models we consider follow a $(1 + \cos\theta^*)^2$ angular distribution in the Z' rest frame. Positrons and anti-muons alternatively follow a $(1-\cos\theta^*)^2$ distribution. The leftmost plot in Figure 5.3 shows that the generator-level angular distributions of $e^\pm$ from the 200 GeV/c^2 Z' sample conform to

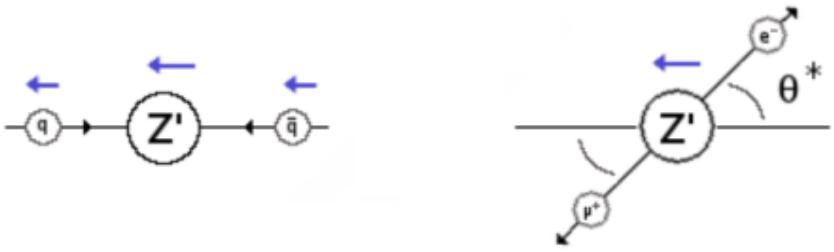

Figure 5.2: **Z' Polarization.** The Z' is polarized in its rest-frame for our signal model because we assume pure left-handed fermionic couplings. The couplings influence the angular distribution of the $e\mu$ decay products. The probability for their emission at angle θ^* with the z-axis is proportional to $(1 \pm cos\theta^*)^2$.

expectation.

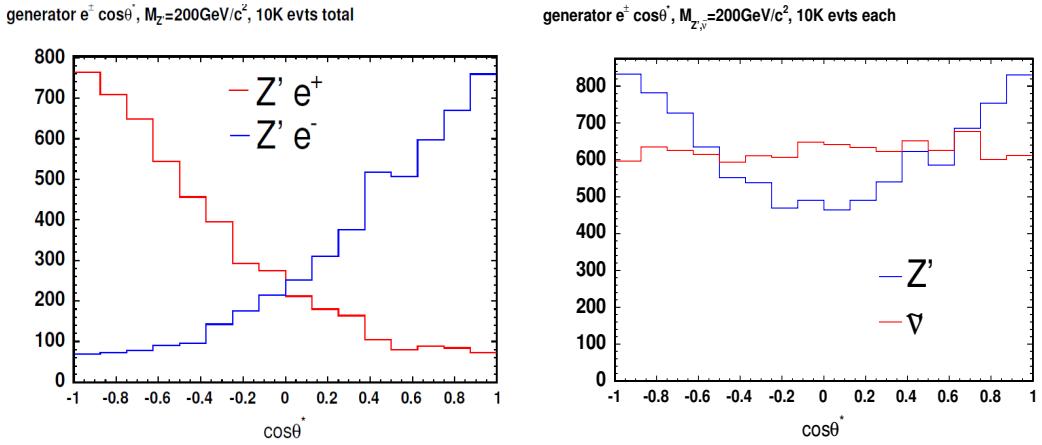

Figure 5.3: **Angular Distributions.** The angular distributions of generator-level electrons and positrons from Z' decay in the Z' rest frame are shown on the left. Their combined distribution, right, contrasts with that of isotropic $\tilde{\nu}_\tau$ decay. The excess of $cos\theta^* \approx 1$ leptons from Z' decay leads to a smaller acceptance relative to the $\tilde{\nu}_\tau$.

We present the combined $e^\pm$ $cos\theta^*$ distribution from the 200 GeV/c^2 Z' and $\tilde{\nu}_\tau$ samples in Figure 5.3. The distributions for muons are similar and are not shown. Differences in the distributions explain the smaller Z' acceptance of Figure 5.1. The Z' and $\tilde{\nu}_\tau$ are typically produced with small p_T and leptons from Z' decay, emerging preferentially in the z-direction, are less likely to be

reconstructed in the central region of the detector, as indicated in Figure 5.4.

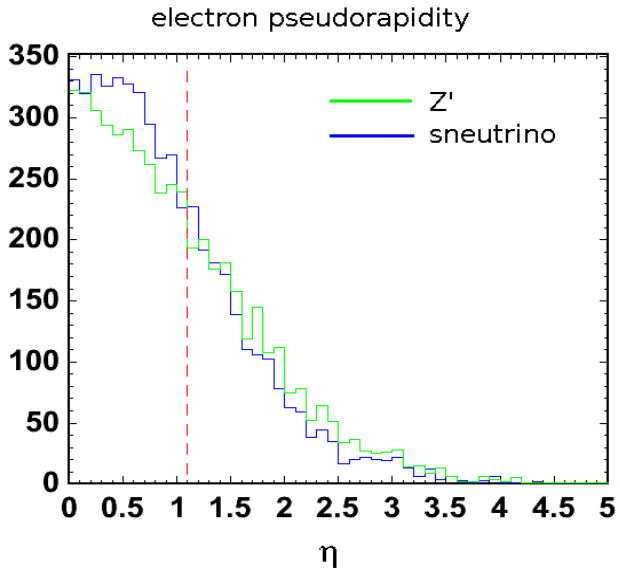

Figure 5.4: **Generator Level Pseudorapidity.** The difference between the angular distributions of Z' and $\tilde{\nu}_\tau$ decay products results in a larger acceptance for sneutrinos. This plot compares the generator-level $|\eta|$ distribution of $e^{\pm}$ from Z' and $\tilde{\nu}_\tau$ in the lab-frame. The dashed line indicates our event selection criterion of $|\eta| < 1.1$.

We will use the calculated $\tilde{\nu}_\tau$ and Z' acceptance curves in Section 5.3 to "invert" Equation 5.1 and determine limits on the $\sigma \times \mathrm{Br}(\mathrm{e}\mu)$'s of the signal processes. The technique we use in this procedure depends on the widths of Gaussian functions that we fit to the reconstructed signal $M_{e\mu}$ distributions. We include the $M_{e\mu}$ distributions from the nine sneutrino samples in Appendix A for the purpose of that discussion. Figure 5.5 plots the RMS extracted from these and corresponding Z' $M_{e\mu}$ distributions. The figure shows that the $M_{e\mu}$ distributions broaden with increasing particle mass, a consequence of degradation in momentum and energy resolution with increasing p_T and E_T.

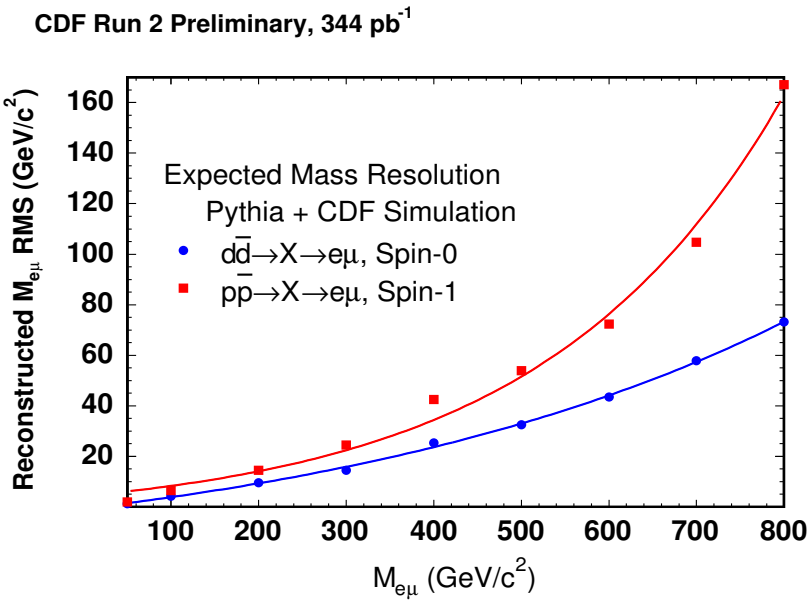

Figure 5.5: **Signal $M_{e\mu}$ widths.** Fits to the RMS of the signal $M_{e\mu}$ distributions are used to set the widths and locations of acceptance windows in our sensitivity and cross section limit calculations.

5.1.2 Backgrounds

The relevant physics backgrounds in our search are the leptonic decays of $Z/\gamma^* \rightarrow \tau\tau$, $t\bar{t}$ and dibosons. Figure 5.6 shows the leading order diagrams for these processes. We calculate acceptances for the SM backgrounds using a procedure similar to that explained for the signal models. We calculate the contribution expected from each SM background source using the production cross sections from Table 4.2 in Equation 5.1. Table 5.3 lists the integrated contributions of each of the background channels. We use these to normalize the $M_{e\mu}$ distributions reconstructed from the MC samples to the theoretical expectation. The normalized $M_{e\mu}$ distributions of all SM backgrounds are combined in Figure 5.7.

Objects misidentified as leptons are an additional background in our search. Isolated jets that deposit a significant amount of their energy in the electromagnetic calorimeters may be misreconstructed as electrons. Events that contain such

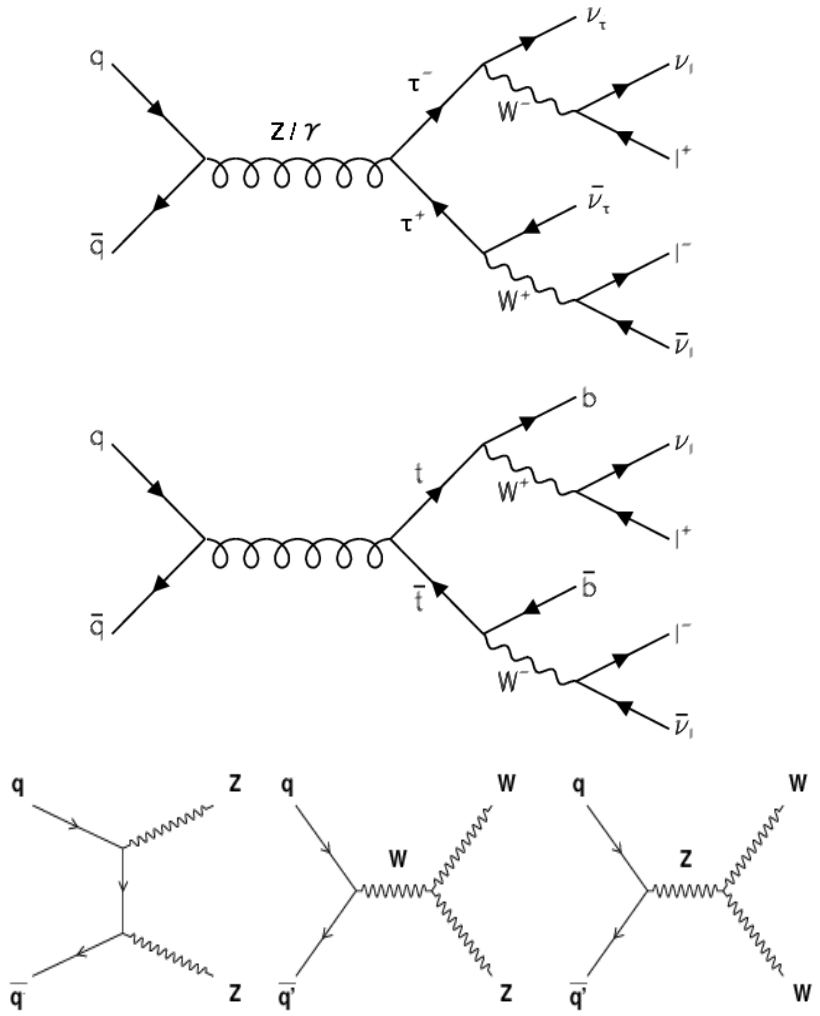

Figure 5.6: **Background Processes.** These diagrams represent the leading order SM backgrounds that contribute in the $e\mu$ search.

"fake" electrons can pass our event selection criteria and contribute to an $e\mu$ signal. Likewise, some charged pions will not shower in the CHA but "sail-through" to the muon chambers. Similarly, pions and kaons may decay in flight, producing real muons that "punch through" the CHA to reach the muon chambers. Muon candidates from these sources can pass our identification requirements and enter our pool of selected events. These processes occur infrequently and their misidentification as high-p_T leptons depends on detailed characteristics of the CDF II detector. Modeling such misidentification in Monte Carlo is difficult. We obtain

a more reliable estimate of this background by applying misidentification probabilities (*ie,* fake rates) measured in jet-enriched data samples to events in our high p_T lepton dataset.

Our treatment of fake leptons is based on a technique developed in the CDF Top-Dilepton analysis [61]. We define fake rates as the probability for a "fakeable object", a loosely identified CdfEmObject or CdfMuon associated with a jet, to pass the full lepton identification criteria. We determine fake rates by dividing the number of fakeable objects that pass the ID cuts (described in Section 4.2) by the total number of fakeable objects in the dataset. Tables 5.1 and 5.2 list the cuts that define the fakeable objects denominators.

Quantity	**Value**
Region	CEM
Conversion	false
HadEm	$\leq (0.055 + (0.00045 \times En))$

Table 5.1: **Denominator CdfEmObject Cuts.** These cuts define the loosely identified CdfEmObjects appearing in the denominator of our CEM fake rate. They are a subset of the full electron ID cuts.

Quantity	**Requirement**
Fiducial	true
$\mid D_0 \mid$	≤ 0.20 cm if Track Si Hits==0
	≤ 0.02 cm if Track Si Hits > 0

Table 5.2: **Denominator CdfMuon Cuts.** These cuts define the CdfMuon objects appearing in the denominators of our muon fake rates. They are a subset of the full muon ID cuts.

We calculate fake rates in the $gjt10d$, $gjt20d$, $gjt30d$ and $gjt40d$ jet datasets.

We remove trigger bias from the datasets by selecting jets that do not exclusively satisfy the trigger criteria listed in Table 4.4. All jets in an event are considered to be unbiased if multiple jets in that event pass the requirements imposed by the jet trigger. Alternatively, we consider a jet to be biased if it alone meets the trigger thresholds. To determine which jets satisfy the trigger criteria, it is necessary to recalculate jet-E_T with respect to $z_0 = 0$, the value used in the Level 3 trigger, instead of using default jet-E_T values calculated with respect to a reconstructed event z_0. Figure A.3 in Appendix A shows the E_T of jets from the $gjt20d$ sample before and after the unbiasing procedure.

We remove real leptons from the unbiased samples by rejecting events in which the invariant mass of a denominator object pair falls between $76 - 106$ GeV/c^2 (to remove Z) or in which the transverse mass formed from the missing E_T and denominator object is greater than 50 GeV/c^2 (to remove W). These requirements reject an average of 1% and 10% of events from the samples respectively. Finally, we count the number of objects that pass the numerator and denominator cuts and calculate the misidentification probabilities shown in the plots of Appendix A. We parameterize the electron and muon fake rates in terms of E_T and p_T respectively. We combine results from the CMUP and CMX categories muon (labeled TMUO in the figure) and, separately, the CMU-only and CMP-only categories (LMUO) to improve statistics.

The weighted average of the fake rates calculated from each dataset is indicated with black squares in the plots of Figure A.4. We use the E_T and p_T parameterized averages to estimate the background contribution from fakes leptons in the high-p_T lepton samples. We select events containing one lepton the passes the ID cuts of Section 4.2 and at least one fakeable object of different lepton flavor. We reject an event if it contains both electrons *and* muons that pass the identification cuts. This selection specifically rejects events that we will

later consider as potential signal candidates and is used to safeguard against the introduction of bias in the analysis[1]

Next, we impose the event-topology cuts on all combinations of real lepton + fakeable objects in the event and confirm that the trigger requirements are satisfied. Passing combinations are binned in invariant mass and the relevant fake rate is applied. The result provides an estimate of the background due to fake leptons as a function of $M_{e\mu}$, which we show together with the SM backgrounds in Figure 5.7. The integrated number of expected fake events for the CEM, TMUO and LMUO categories are $1.6 \pm 0.1_{stat} \pm 0.3_{sys}$, $0.3 \pm 0.2_{stat} \pm 0.3_{sys}$ and $1.4 \pm 1.1_{stat} \pm 1.1_{sys}$.

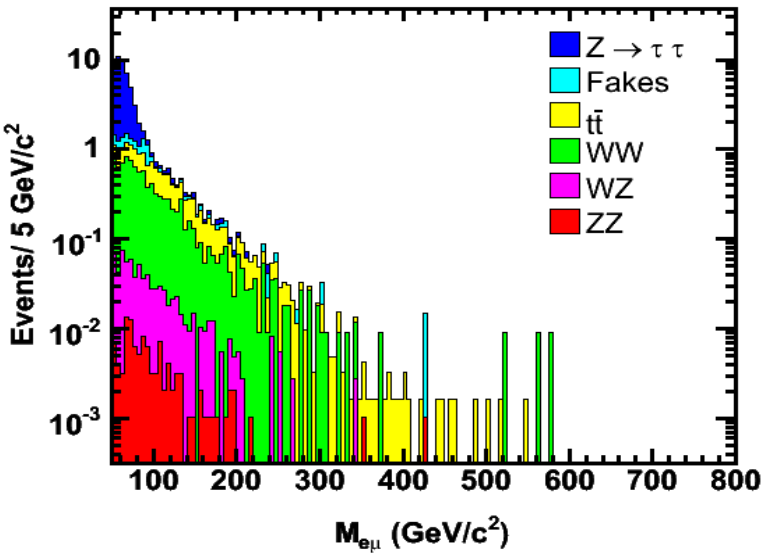

Figure 5.7: **Background $M_{e\mu}$ Distributions.** This plot shows stacked $M_{e\mu}$ distributions of the SM and fake backgrounds scaled to theoretical predictions. $Z \rightarrow \tau\tau$ is the largest source of background and contributes primarily reconstructed invariant masses below 100 GeV/c^2.

[1]We are able to impose this selection without significantly underestimating our fake background because our MC studies indicate that high-mass $e\mu$ events from SM sources is small.

Channel	Expectation $(50 - 800$ GeV/c$^2)$
$Z \to \tau\tau$	$39.3 \pm 1.1 \pm 3.4$
$t\bar{t}$	$6.4 \pm 0.2 \pm 1.1$
WW	$9.0 \pm 0.5 \pm 1.0$
WZ	$0.7 \pm 0.1 \pm 0.1$
WZ	$0.1\pm < 0.1\pm < 0.1$
$fake\ lepton$	$3.3 \pm 1.4 \pm 1.8$
Prediction	$58.9 \pm 1.9 \pm 4.1$

Table 5.3: $e\mu$ **Background Expectations.** We use corrected acceptances and theory cross sections to calculate the SM expectations in the $50-800$ GeV/c^2 invariant mass range. We derive fake lepton background estimates from data. Errors shown are $\pm$ (statistical) $\pm$ (systematic).

5.2 Control Regions

We perform several cross-checks to validate our event selection procedure and background predictions. The tests include comparisons of Drell-Yan $\sigma\times$Br(eμ) 's calculated in data with the NLO prediction. We also compare the $M_{e\mu}$ distribution of the high-p_T lepton dataset to those of our background samples. The selection criteria we use in the tests differ, though only marginally, from those we apply in the $e\mu$ search. Modified requirements allow us to exclude events with $e\mu$ pairs of large invariant mass (potential signal candidates) and protect against bias in our final result. We minimize contributions from events in the "signal region", $M_{e\mu} > 100$ GeV/c^2, and focus on "control regions" that are rich in background.

5.2.1 Electron/Electron

We compare reconstructed $Z/\gamma^* \rightarrow ee$ invariant mass (M_{ee}) distributions from data and Monte Carlo samples and calculate a $\sigma(Z/\gamma^*)\times$Br(e$^+$e$^-$) to confirm our electron identification techniques. We use the *ztop2i* ntuples and the inclusive high-p_T electron dataset, *bhel0d*, for this study. As mentioned previously, the dataset represents 369.6 pb^{-1} after application of the electron goodrun list.

We select candidate events that contain at least two identified CEM electrons of reconstructed M_{ee} that falls within the range 76 GeV/c^2 $<$ M$_{\rm ee}$ $<$ 106 GeV/c^2. The M_{ee} requirement is chosen to be rather tight ($\pm 3\sigma$) in order to limit backgrounds to the Drell Yan process. We do not subtract backgrounds from the observed event yield because they contribute only $\sim$1.5% of the total. We then apply the event-topology cuts ($\Delta Z_0^{trk} < 5$ cm and opposite charge) to the electron pairs. If an event contains multiple combinations of reconstructed electrons that satisfy all of the above criteria, we select the combination with the highest

M_{ee} .

Figure 5.8 compares the reconstructed Monte Carlo M_{ee} distribution, which we normalize to the expectation in 369.6 pb^{-1}, with the distribution obtained from data. The apparent shift in the MC distribution with respect to data is attributed to a difference in the actual and simulated electron energy scales. We choose not to correct electron energy in the MC sample as a shift of this magnitude does not significantly impact our acceptance. We compare the data and MC electron p_T distributions of pairs that pass our selection criteria in Appendix A.

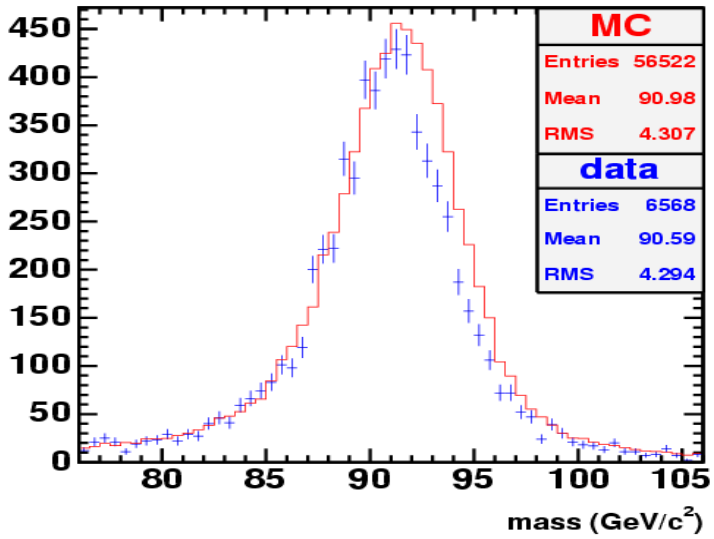

Figure 5.8: $Z/\gamma^* \to ee$ **Invariant Mass.** Data (points) and Monte Carlo (line). The relative shift between data and Monte Carlo is due to a discrepancy in the electron energy scale. We do not correct for this as it does not significantly effect our acceptance.

We calculate $\sigma(Z/\gamma^*) \times \mathrm{Br}(\mathrm{e^+e^-})$ using the number of data events that pass our selection and an acceptance, α_{tot}, determined from the MC sample. The acceptance calculation uses only those MC events in which the generator-level dielectron invariant mass lies between 66 and 116 GeV/c^2. We impose this requirement so that our $\sigma(Z/\gamma^*)\times\mathrm{Br}(\mathrm{e^+e^-})$ result may be compared with the NNLO

$\sigma(Z/\gamma^*)\times\mathrm{Br}(\ell^+\ell^-)$ calculated for the same range (252 ± 5 pb) in the Run II CDF W/Z cross section analysis [59]. Although the effect is small, the use of a wider M_{ee} range in the acceptance denominator also accounts for contributions in the $76 - 106$ GeV/c^2 window from outside events that are improperly reconstructed to sit within.

We correct the MC acceptance with the $f_{reco/ID}$ and f_{trig} scale factors appropriate for two CEM electrons. The resulting α_{tot} is used in Equation 5.1 to obtain $\sigma(Z/\gamma^*) \times \mathrm{Br}(\mathrm{e^+e^-})$, given in Table 5.4. As stated above, this result is to be compared with 252 ± 5 pb, the NNLO $\sigma(Z/\gamma^*) \times \mathrm{Br}(\ell^+\ell^-)$ for $66 < m_{Z/\gamma^*} < 116$ GeV/c^2 range. We find sufficient agreement between the measured and expected $\sigma(Z/\gamma^*) \times \mathrm{Br}(\mathrm{e^+e^-})$ for the validation of our electron selection technique.

N_{obs} $\mathcal{L}_{\mathrm{int}}$ α_{tot}	6568 369.6 pb^{-1} $6.8 \pm 0.1\%$
$\sigma(Z/\gamma^*) \times \mathrm{Br}(\mathrm{e^+e^-})$	260.5 ± 1.1 pb

Table 5.4: $Z/\gamma^* \rightarrow ee$ **Results.** Our measured cross section is consistent with the NNLO value of 252 ± 5 pb. We attribute the bulk of the excess in our measured $\sigma(Z/\gamma^*)\times\mathrm{Br}(\mathrm{e^+e^-})$ to background contamination, which we do not subtract. The error on acceptance is statistical only.

5.2.2 Muon/Muon

A similar test performed in the $Z/\gamma^* \rightarrow \mu\mu$ control region provides a check of our muon selection technique. We use the *bhmu0d* dataset, which represents 357.0 pb^{-1} after application of the muon goodrun list, and the *ztop0i* MC sample.

We choose events with at least two identified muons and require a pair that passes our event-level and invariant mass cuts. We further stipulate that at least one of the muons be CMUP or CMX to ensure that MC events satisfy the trigger requirements met in data. Figure 5.9 compares the dimuon invariant mass distribution in data to that obtained from the MC sample after its normalization to prediction.

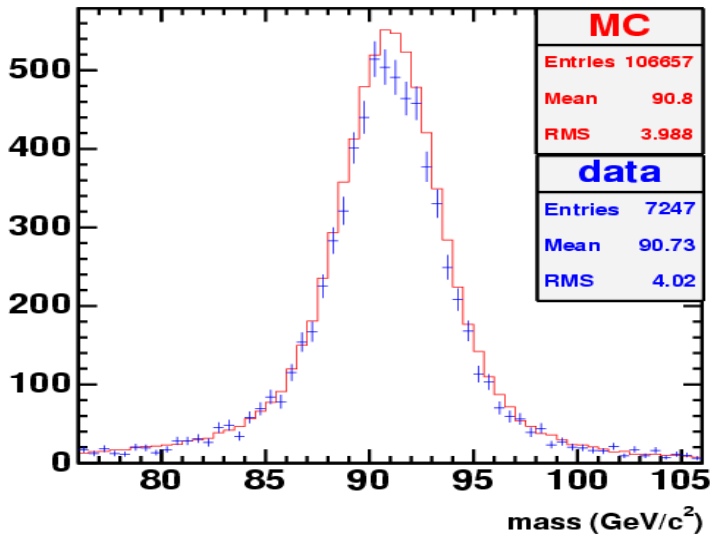

Figure 5.9: $Z/\gamma^* \to \mu\mu$ **Invariant Mass.** We find good agreement between data (points) and Monte Carlo (line). The MC distribution is normalized to theory.

The method we use to calculate a $\sigma \times \mathrm{Br}(\mathrm{e}\mu)$ in the $Z/\gamma^* \to \mu\mu$ control region is similar to that described for $\sigma(Z/\gamma^*) \times \mathrm{Br}(\mathrm{e}^+\mathrm{e}^-)$. In this case however, we apply separate corrections to the acceptances determined for each of the allowed muon combinations (*i.e.:* [CMUP or CMX] + [CMUP,CMU,CMP, or CMX]). The corrected acceptances are combined and the total is used to calculate a cross section times branching ratio for data. Table 5.5 lists the values input to Equation 5.1 and our result. The calculated $\sigma(Z/\gamma^*) \times \mathrm{Br}(\mu^+\mu^-)$ is consistent with the NNLO prediction of 252 ± 5 pb.

N_{obs} $\mathcal{L}_{\rm int}$ α_{tot}	7247 357.0 pb^{-1} $8.0 \pm 0.1\%$
$\sigma(Z/\gamma^*) \times {\rm Br}(\mu^+\mu^-)$	255.2 ± 0.9 pb

Table 5.5: $Z/\gamma^* \to \mu\mu$ **Results.** Our measured cross section agrees with the NNLO value of 252 ± 5 pb. The error given for acceptance is statistical only.

5.2.3 Electron/Muon

A low-mass $e\mu$ control region permits a direct test of the event selection and the Monte Carlo background predictions that we use in the search. We apply the full selection criteria described in Sections 4.2 and 4.3 and an additional reconstructed invariant mass constraint of 50 GeV/c^2 $\leq$ M$_{e\mu}$ $\leq$ 100 GeV/c^2. This $M_{e\mu}$ region is dominated by SM backgrounds and was excluded in the CDF Run I $e\mu$ search.

As in our final analysis, we choose events in data from runs marked "good" for both electrons and muons, leaving a 344 pb^{-1} dataset. We require that MC events pass the criteria of at least one of the CEM18, CMUP18 or CMX18 triggers. We calculate acceptances for the Monte Carlo samples in the $50-100$ GeV/c^2 window and use the corrected values to predict an expected number of background events for each channel. Figure 5.10 compares the $M_{e\mu}$ distributions of data and MC. The degree of consistency observed is adequate considering the small number of events involved. Table 5.6 lists the observed and predicted event yields.

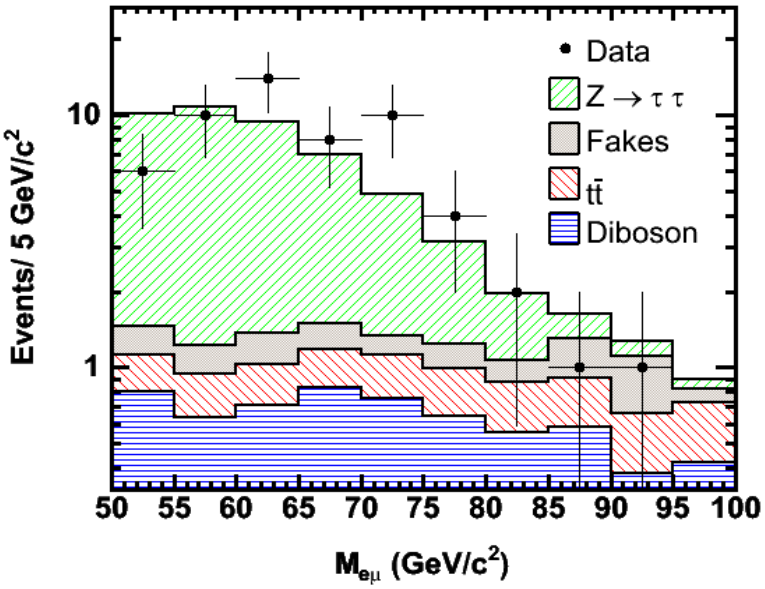

Figure 5.10: **Low-$M_{e\mu}$ Control Region Distributions.** We compare data and MC in the $M_{e\mu}$ region below 100 GeV/c^2. The agreement in the shapes of the distributions observed is sufficient given the small number of observed and predicted events in the region.

Channel	Control Region
$Z \to \tau\tau$	$38.8 \pm 0.9 \pm 2.8$
diboson	$6.6 \pm 0.2 \pm 0.6$
$t\bar{t}$	$3.6 \pm 0.1 \pm 0.5$
fake lepton	$2.9 \pm 1.1 \pm 1.3$
Prediction	$51.9 \pm 1.5 \pm 3.2$
Observation	56

Table 5.6: **Low-$M_{e\mu}$ Control Region Event Counts.** This table shows the individual contributions of background sources to the distributions shown in Figure 5.10. We find good agreement between the observed and predicted event yields.

5.3 Sensitivity

Having confirmed the consistency of results and predictions in the control regions, we now assess our sensitivity to an RPV sneutrino[2] signal. Sensitivity refers to the anticipated strength of our $\sigma\times$Br(eμ) and particle mass limits. The procedure we use to calculate an expected $\sigma(\tilde{\nu}_\tau)\times$Br(e$\mu$) upper-limit is similar to the $\sigma(Z/\gamma^*)\times$ Br($\ell^+\ell^-$) calculations of the previous section. Here, however, we do not apply the event selection in data and therefore remain "blind" to the true number of events observed in data, N_{obs}. We instead assume that the $M_{e\mu}$ distribution in data will correspond to the sum of the predicted backgrounds, $N_{exp} \equiv \Sigma n_{exp}$. This assumption (*i.e.:* the "null hypothesis") allows us to determine an *a priori* $\sigma\times$Br(eμ) limit using only background estimates.

Even if the null hypothesis eventually proves correct and our data does not contain a true signal, we expect that observation will deviate from background predictions because of statistical fluctuations. We address this in the sensitivity study by conducting 5000 pseudo-experiments in which fluctuated background distributions are considered as our observation N_{obs}. First, we use the integral of each background $M_{e\mu}$ distribution as the mean of Poisson probability distribution. Then, in every trial, we draw a random value (n_{fluc}) from the probability distributions to represent the integrals of statistically fluctuated background distributions. We distribute the n_{fluc} events from each backgrounds in $M_{e\mu}$ according to the shape of the original distribution. Finally, we combine the results of all background channels to obtain a total fluctuated background expectation, N_{fluc}, and $M_{e\mu}$ for each trial.

The observation of N_{fluc} events in data when N_{exp} background events are expected does not eliminate the possibility of contributions from LFV signals. We

[2]We do not present a sensitivity study for Z' decays because this interpretation was added after the search concluded.

translate the number of observed and predicted background events to an upper-limit on the number of signal events in data, N_{sig}, using a Bayesian technique. We scan $\sim$600 $M_{e\mu}$ points between $50-800$ GeV/c^2 and count the number of fluctuated background events observed in a window around each point. The separation between points in $M_{e\mu}$ and the size of the windows we apply are determined from 1/10 and 3$\times$ the fitted RMS of the reconstructed $\tilde{\nu}_\tau$ invariant mass distribution (see Figure 5.5) evaluated at the $M_{e\mu}$ values of the scan points. These functional dependencies are chosen to ensure overlap between the windows, preventing gaps in $M_{e\mu}$ coverage. We input the event totals in each window ($N^i_{obs} = N^i_{fluc}$, where i denotes contributions in a single $M_{e\mu}$ window), the expected background in the windows (N^i_{exp}) and the uncertainties on the background and signal acceptance (discussed in the following section) to a Bayesian limit calculator [62]. The Bayesian algorithm returns a 95% confidence level (C.L.) upper-limit on the number of signal events in data, N^i_{sig}.

We perform the procedures described in the preceding two paragraphs for each of the 5000 trials. We then calculate a mean ($\bar{N}^i_{sig}$) signal limit in each $M_{e\mu}$ window and the 1σ and 2σ variances. These values, together with the $d\bar{d} \rightarrow \tilde{\nu}_\tau \rightarrow e\mu$ acceptance curve from Figure 5.1, are used to calculate $\sigma(\tilde{\nu}_\tau) \times$ Br(eμ) upper-limits. We input the $\bar{N}^i_{sig}$ and α_{tot} evaluated at each point in Equation 5.1 to obtain the mean 95% C.L. upper-limit $\sigma \times$Br(eμ) curve, shown in Figure 5.11.

Figure 5.11 also shows the $\sigma(\tilde{\nu}_\tau)\times$Br(e$\mu$) prediction as intersecting the calculated upper-limits. This curve is obtained from Equation 5.2, the LO $\sigma\times$Br(eμ) for $d\bar{d} \rightarrow \tilde{\nu}_\tau \rightarrow e\mu$ in the narrow width approximation [56]. The $\Gamma_{d\bar{d}}$ and $\Gamma_{e\mu}$ partial widths are proportional to the square of the RPV $\tilde{\nu}_\tau$ couplings. We choose the current best limits for λ'_{311} and λ_{132} from low-energy experiments (0.10 and 0.05 respectively) and input $\hat{s} = (1.96 \text{ TeV})^2$ and $\tau = m_{\tilde{\nu}_\tau}/s^2$.

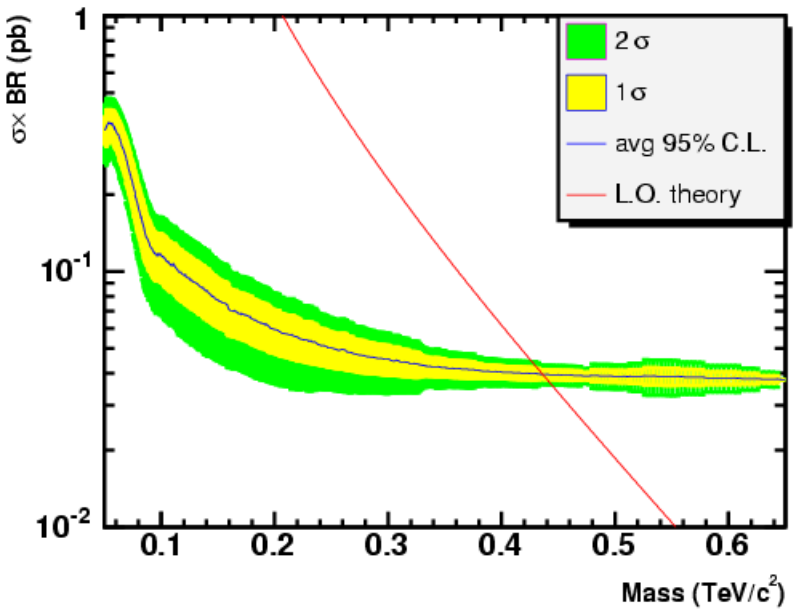

Figure 5.11: **Sensitivity.** The leading order cross section times branching ratio (red) is shown with the mean 95% CL upper-limit obtained when assuming contributions from backgrounds only. The intersection of the theory curve with our sensitivity bands suggests a $\tilde{\nu}_\tau$ mass limit above 430 GeV/c^2.

$$\sigma(d\bar{d} \to \tilde{\nu}_\tau \to e\mu) = \frac{4\pi^2}{9}\frac{\Gamma_{d\bar{d}}\Gamma_{e\mu}}{m\hat{s}\Gamma_t} \times \int_\tau^1 dx \left[\bar{d(x)}d(\bar{\tau/x}) + d(x)d(\tau/x)\right]/x \quad (5.2)$$

$$\Gamma_{d\bar{d}} = \frac{3}{4} \times \frac{(\lambda'_{311})^2}{4\pi} m_{\tilde{\nu}_\tau} \quad , \Gamma_{e\mu} = \frac{3}{4} \times \frac{(\lambda_{132})^2}{4\pi} m_{\tilde{\nu}_\tau} \quad , \Gamma_t = \Gamma_{d\bar{d}} + \Gamma_{e\mu} \quad (5.3)$$

We obtain values for the cross section by performing a numeric integration of the parton distribution at the $\sim$600 $M_{e\mu}$ points in the scan. The parton number densities for d and $\bar{d}$ are taken from the CTEQ6L [58] library and we use routines from the GSL [63] software package to integrate the density function over parton momentum fractions x. We assume sneutrino branching ratios to $e^+\mu^-$ and $e^-\mu^+$ only and double the prediction of Equation 5.2 to account for contributions from both channels. The intersection of the LO curve with the mean upper-limit in

Figure 5.11 suggests that we may expect to set a limit beyond ~ 430 GeV/c^2.

Figure 5.12 shows our sensitivity to results from a particular pseudo-experiment in which we have added $d\bar{d} \rightarrow \tilde{\nu}_\tau \rightarrow e\mu$ contributions to the background expectations. For this scenario we calculate an expected number of signal events for a 300 GeV/c^2 $\tilde{\nu}_\tau$ using the LO cross section and acceptance determined at that mass. The result, 16.2 events, is Poisson fluctuated and then used to select a total number of events from the signal $M_{e\mu}$ distribution shown in Appendix A. We add these events to the fluctuated SM prediction and perform the upper-limit cross section calculation. The resulting SM + RPV sneutrino prediction is shown as a black curve in Figure 5.12. The broad $> 2\sigma$ discrepancy in our $\sigma(\tilde{\nu}_\tau) \times \mathrm{Br}(e\mu)$ upper-limit confirms our sensitivity to 300 GeV/c^2 $\tilde{\nu}_\tau$ decay.

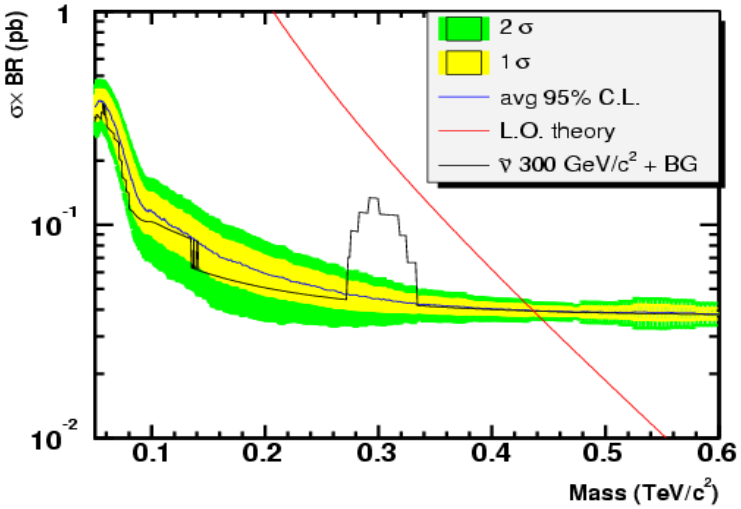

Figure 5.12: **Sensitivity for a $\tilde{\nu}_\tau$ hypothesis.** Our mean sensitivity (blue) is shown with results of a particular pseudo-experiment (black) that assumes a 300 GeV/c^2 $\tilde{\nu}_\tau$ signal. The peak near 300 GeV/c^2 shows that we are sensitive to the leading order prediction.

The techniques we employ in the sensitivity study resemble those we use in the interpretation our search results in the following chapter. While similar, several aspects of the methods described above have evolved during the course of the

analysis. First, we discard the LO $\sigma \times \mathrm{Br}(\mathrm{e}\mu)$ of Equation 5.2 in favor of NLO values provided to us by Choudhury *et. al* [64]. Second, we adopt an approach in which every event in data and MC respectively contributes to the N^i_{obs} and N^i_{exp} at each of the ~ 600 $M_{e\mu}$ points in the scan. The new procedure is depicted in Figure 5.13.

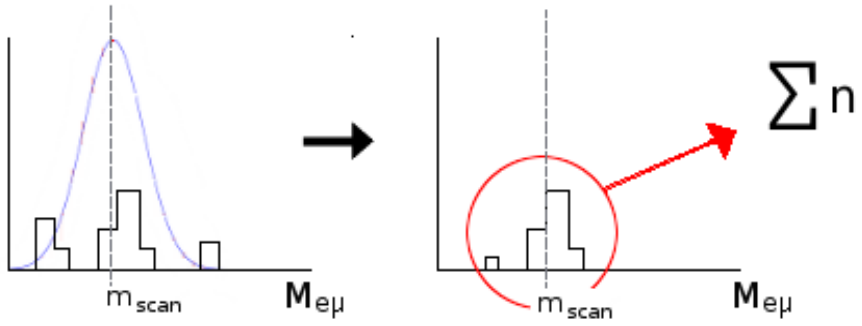

Figure 5.13: $\sigma \times \mathrm{Br}(\mathrm{e}\mu)$ **Scan Technique.** The technique we use to set $\sigma \times \mathrm{Br}(\mathrm{e}\mu)$ upper-limits in data centers a unit-amplitude Gaussian on several scan points (m_{scan}). We use the Gaussian to weight all predicted and observed events (left). The weighted events (right) are summed and input to the upper-limit $\sigma \times \mathrm{Br}(\mathrm{e}\mu)$ calculation.

We sweep a unit amplitude Gaussian across the $M_{e\mu}$ range and use the function to weight all data and MC events. We scan invariant masses between 50 and 800 GeV/c^2 as before but now center the Gaussian, rather than a fixed width acceptance window, on each of the ~ 600 $M_{e\mu}$ points. The width of the Gaussian varies across the range and is determined from the $M_{e\mu}$ resolution curve shown in Figure 5.5. The Gaussian amplitude evaluated at the $M_{e\mu}$ value of an event determines the weight with which it contributes to the event total for a given scan point. This technique removes spurious structure in the upper-limit $\sigma \times \mathrm{Br}(\mathrm{e}\mu)$ curves produced with the original method.

5.4 Systematic Uncertainties

The Bayesian algorithm we use to obtain upper-limit $\sigma \times \mathrm{Br}(\mathrm{e}\mu)$'s requires the uncertainties of two quantities, that on the product of signal acceptance and luminosity, $\delta(\alpha_{tot}\mathcal{L}_{\mathrm{int}})$, and the error on the number of expected background events, $\delta(N_{exp})$. This section discusses the sources of uncertainty that contribute to these quantities and explains the methods we use to estimate their magnitudes. Table 5.7 summarizes the contributions to $\delta(N_{exp})$ and $\delta(\alpha_{tot}\mathcal{L}_{\mathrm{int}})$.

Uncertainty Source	$\delta(\alpha_{tot}\mathcal{L}_{\mathrm{int}})$	$\delta(N_{exp})$
Luminosity	6.0%	5.6%
E & P Resolution	3.2%	–
MC Generator	2.9%	–
PDF's	2.4%	2.3%
Scale Factors	1.6%	1.6%
Fake Probabilities	–	3.1%
Cross Sections	–	4.4%
Total Uncertainty	7.9%	8.8%

Table 5.7: **Systematic Uncertainties.** This table lists the various sources of uncertainty in our measurement. Luminosity error is the dominant uncertainty on both signal and background predictions.

While an understanding of the uncertainties involved in the analysis is important, we find they have little effect on the strength of the limits we set. As shown in Figure 5.14, inflating the $\delta(N_{exp})$ and $\delta(\alpha_{tot}\mathcal{L}_{\mathrm{int}})$ uncertainties to 20% produces only a $\sim$3 GeV/c^2 difference in our $\tilde{\nu}_\tau$ mass limit. Likewise, their reduction to zero improves the mass limit by just $\sim$1 GeV/c^2. Our limits are robust against variations in uncertainty because background estimates in this $M_{e\mu}$ region fall below one event, with no events observed in data.

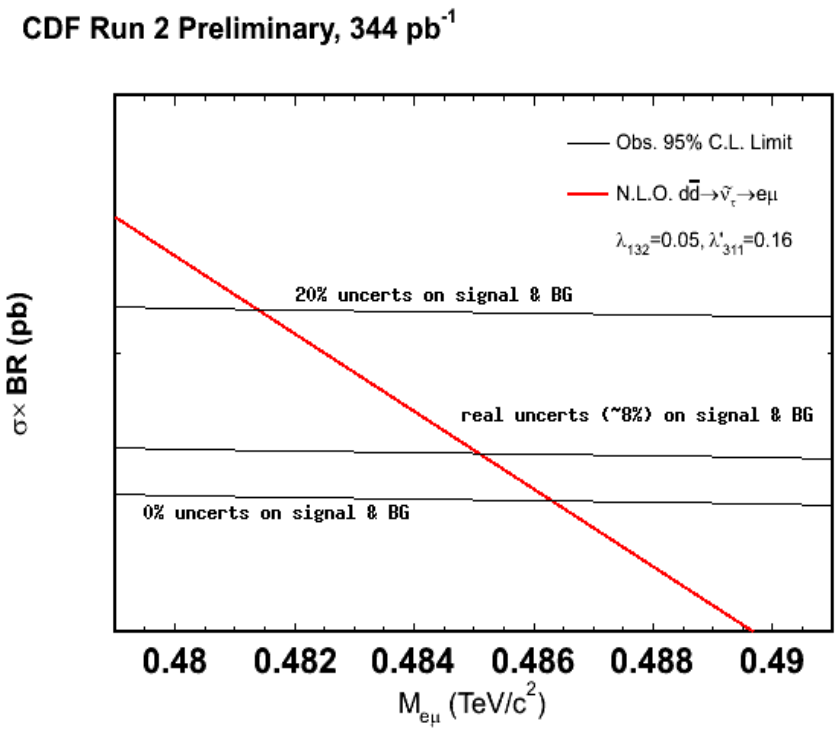

Figure 5.14: **Uncertainty Independence.** Our expected $\sigma \times \mathrm{Br}(e\mu)$ limits are generally insensitive to the magnitudes of the uncertainties. A ~ 5 GeV/c^2 difference in the $\tilde{\nu}_\tau$ mass limit results when changing the uncertainties from $0 - 20\%$.

5.4.1 Mass Resolution

As described in Section 5.3, the sizes of the acceptance windows we apply in the limit calculation depend on the widths of the reconstructed signal distributions. Uncertainties in the widths of the simulated $M_{e\mu}$ distributions arise from underlying uncertainties in energy and momentum resolution. We perform a toy Monte Carlo study to investigate how these detector-level uncertainties translate to an uncertainty on signal acceptance.

The CDF simulation software accounts for detector resolution and we could vary the resolutions used during simulation to determine the effect on acceptance. Instead, we avoid the complexity of the software by beginning with the output of the Monte Carlo generator. We smear the generator-level energies and

momenta of electrons and muons in our signal samples with resolution functions that represent the accuracy of measurements from the COT and CEM (see Sections 3.2.2 and 3.2.4). After smearing, the generator-level energy and momentum distributions nearly match those of reconstructed electrons and muons.

We then form $M_{e\mu}$ distributions from the smeared four-vectors, use the RMS's of these distributions to define $M_{e\mu}$ windows and perform the acceptance calculation. Next, we vary the resolutions by their quoted uncertainties and again smear the generator-level energies and momenta. This results in another set of $M_{e\mu}$ distributions with different RMS's, which we use to recalculate signal acceptance. We take the largest acceptance difference found using this procedure, 3.2%, as the uncertainty due to resolution effects.

5.4.2 Monte Carlo Generation

Our signal predictions suffer uncertainties associated with the Monte Carlo techniques we use. We estimate these by comparing the signal acceptance calculated with $d\bar{d} \rightarrow H \rightarrow e\mu$ in PYTHIA to that calculated with the $d\bar{d} \rightarrow \tilde{\nu}_\tau \rightarrow e\mu$ process in Herwig [65]. The uncertainty on SM background acceptance due to Monte Carlo generation is found to be negligible.

Herwig can be used to generate a number RPV SUSY processes. Process generation is controlled with an input file in which one specifies RPV coupling values and sparticle masses. We select the $d\bar{d} \rightarrow \tilde{\nu}_\tau$ production process and obtain a 100% $\tilde{\nu}_\tau \rightarrow e\mu$ branching fraction by inserting non-zero values for λ'_{311} and λ_{132} . The λ'_{311} and λ_{132} couplings also factor in the RPV production and decay of charged sleptons, *i.e.:* $\bar{u}d \rightarrow \tilde{\tau} \rightarrow e\mu$, and we specify an infinite stau mass to obtain $\tilde{\nu}_\tau$ production only. We then run Herwig from within the same CDF Monte Carlo software that we use for generation with PYTHIA. The largest acceptance

difference we observe between Herwig and PYTHIA samples generated for the same resonance mass and set of parton distribution functions is 2.9%.

5.4.3 Parton Distribution Functions

We estimate uncertainties due to the parton distribution functions (PDF's) employed in the Monte Carlo generation of signal processes using the CTEQ Hessian technique. [66] With this approach we are able to determine PDF uncertainties without generating multiple Monte Carlo samples that differ only by the PDF's used. We weight the acceptance calculated using CTEQ5L PDF's with a set of scale factors to determine corresponding acceptances for alternate PDF sets.

The Hessian approach utilizes global data on hard-scattering processes and parameterizes these in terms of multidimensional vectors. The "best fit" between data and PDF sets, which are also formulated as parameterized vectors, is determined using a χ^2 function. The χ^2 is expanded about its minimum and the quadratic term in the series includes a Hessian matrix. The eigenvectors of the Hessian constitute a basis for the translation of predictions between different PDF sets. The technique provides scale factors that can be used to estimate the uncertainties on observable quantities that result from variations in the eigenvectors. We apply 40 scale factors to determine the uncertainty in acceptance due to variations in the 20 eigenvectors of the CTEQ6M PDF set. Adding the percent acceptance differences in quadrature, we find a 2.4% uncertainty due to the choice of PDF set.

5.4.4 Luminosity

The largest contribution to the uncertainties of both signal and SM background estimates stems from a 6% uncertainty on luminosity [67]. This value is the

combination of a 4% uncertainty on the efficency of the CLC detector and a 4% uncertainty on the inelastic $p\bar{p}$ cross section. The 6% factors directly in $\delta(\alpha_{tot}\mathcal{L}_{\rm int})$ but only 5.6% in $\delta(N_{exp})$ since the estimated number of misidentified leptons is not influenced by errors in luminosity measurement.

5.4.5 Lepton Identification

The CEM electron ID scale factor is sensitive to the amount of background present in the invariant mass window used in its derivation. The uncertainty from background contamination is measured from the largest discrepancy observed in the scale factor when calculated over a range of window widths. This uncertainty is combined with the statistical uncertainty on measurement to provide an overall error on the scale factor (0.1%). Uncertainties on the CMUP(0.51%), CMX(0.56%), CMU-only(0.94%) and CMP-only(0.84%) scale factors are determined with a similar technique. We find that lepton ID contributes 1.6% to the total uncertainty on corrected acceptance.

5.4.6 Fake Rates

We obtain the uncertainty on the expected number of fake leptons from differences in the fake rates measured in the various inclusive jet data samples. Appendix A shows the fake rates obtained from the samples. The largest differences are $\sim$ 1.5% for the CEM selection and $\sim$ 0.2% and $\sim$ 0.6% for the TMUO and LMUO categories. These uncertainties introduce a 3.1% relative uncertainty on the total expected background.

5.4.7 Background Cross Sections

Errors on the NLO cross sections we use to obtain estimates of the SM backgrounds also contribute to the overall uncertainty of our measurement. The error on the $t\bar{t}$ cross section is given in [53] as $\sim 15\%$. This value is the combination of PDF uncertainties ($\sim 10\%$) and the uncertainty resulting from the choice renormalization scale ($\sim 5\%$) added linearly. The authors estimate the uncertainty due to PDF's using the Hessian method described above. The uncertainty due to renormalization scale is determined from the variation in the cross section when calculated at different scales (m_{top}, $m_{top}/2$ and $2m_{top}$).

Uncertainties on the WW, WZ and ZZ NLO cross sections (6%, 7% and and 7% respectively) are calculated by the same method [68]. We include a 4% uncertainty on the NNLO Drell-Yan cross section. This is the linear combination of a 2% uncertainty on the LO cross section and a 2% uncertainty on the K-factor we use to scale to NNLO.

Chapter 6

Results

We find no evidence for the LFV decays of heavy neutral particles in 344 pb^{-1}. This chapter presents several interpretations of our null result. We first quantify the level at which data and prediction agree. We then set generic $\sigma\times\text{Br}(\text{e}\mu)$ upper-limits for the LFV decays of heavy scalar and vector particles to $e\mu$. Using these limits, we constrain the masses and couplings of the $\tilde{\nu}_\tau$ and Z' in specific RPV SUSY and E_6-like LFV models.

6.1 Standard Model Consistency

The agreement of data and prediction found in the low-mass control region persists for $M_{e\mu}$ values above the 100 GeV/c^2. Figure 6.1 shows the observed and expected $M_{e\mu}$ distributions over a portion of the full $50 - 800$ GeV/c^2 range. No events appear in data beyond 159 GeV/c^2. Table 6.1 shows that we gain an additional 5 data events in the signal region, slightly fewer that the ~ 7.7 expected. For contrast, Figure A.10 shows the $M_{e\mu}$ distribution we would expect if a 300 GeV/c^2 $\tilde{\nu}_\tau$ were present in data.

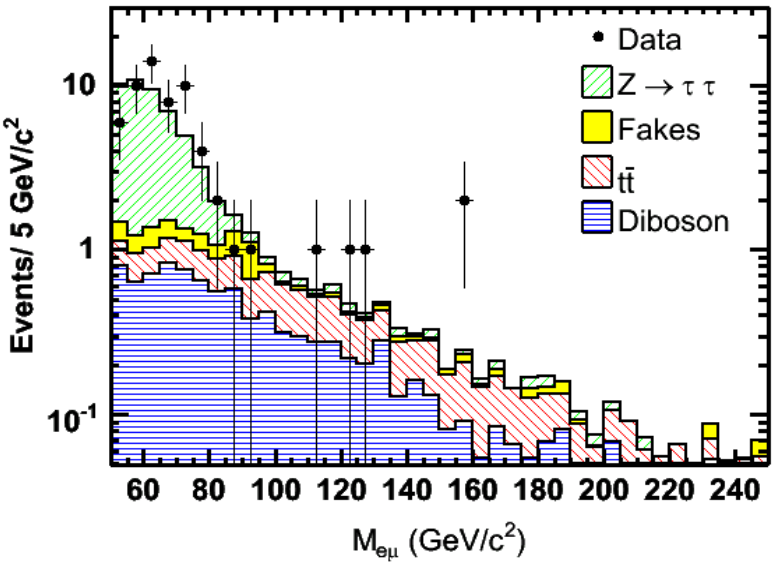

Figure 6.1: $M_{e\mu}$ **Distributions.** Observed and predicted $M_{e\mu}$ distributions agree well over the full $M_{e\mu}$ range. No events appear in data beyond 159 GeV/c^2.

Channel	Control Region	Signal Region
$Z \to \tau\tau$	$38.8 \pm 0.6 \pm 2.3$	$0.6 \pm 0.0 \pm 0.0$
diboson	$6.6 \pm 0.2 \pm 0.4$	$3.5 \pm 0.1 \pm 0.2$
$t\bar{t}$	$3.6 \pm 0.1 \pm 0.2$	$3.2 \pm 0.1 \pm 0.2$
fake lepton	$2.9 \pm 1.1 \pm 1.3$	$0.4 \pm 0.4 \pm 0.4$
Prediction	$51.9 \pm 1.1 \pm 2.7$	$7.7 \pm 0.4 \pm 0.5$
Observation	56	5

Table 6.1: **Event Predictions and Observation.** The total background expectations in both the signal and control regions agree with observations.

We quantify the consistency of data and prediction using a χ^2 test. Bins for the test are chosen before observing data in the signal region in order to avoid biasing the result. We use bins of variable width to achieve individual occupancies of at least 5 predicted events. This value is the minimum needed to satisfy the Gaussian approximation of the Poisson distributed background predictions that is assumed in χ^2 tests. We re-bin the $M_{e\mu}$ distributions of Figure 6.1 and are left with 12 bins. The lower edge of the upper-most bin is placed at 114 GeV/c^2. Table A.1 provides the boundaries and occupancies of all bins.

Equation 6.1 shows the "Pearson-χ^2" formula we use in the test. The numerator in Equation 6.1 is the squared difference between observation and prediction in each $M_{e\mu}$ bin. The σ_i in the denominator is the statistical error, $\sim \sqrt{5}$, and the systematic uncertainty on the predictions of each bin, added in quadrature.

$$\sum_i \frac{(N^i_{obs} - N^i_{exp})^2}{\sigma_i^2} \tag{6.1}$$

The test returns a χ^2 statistic of 14.0. For 12 bins (11 degrees of freedom), this value corresponds to a p-value of 23%. The p-value represents the probability of finding lesser agreement between observation and prediction assuming the provided uncertainties on the expectation in each bin. If the high-mass $e\mu$ search were performed many times on independent data samples, we would expect 23% of the results to show a larger discrepancy than that which we observe. A given hypothesis is typically rejected as consistent with observation if an obtained p-value is $< 5\%$. Because our result exceeds this value, we judge observed discrepancies to be insignificant and retain the SM hypothesis as a valid explanation of our data.

6.2 Cross Section Limits

With no evidence for New Physics in the high-mass $e\mu$ channel, we turn to setting generic $\sigma \times \mathrm{Br}(e\mu)$ upper-limits on LFV processes. This procedure involves the application of techniques developed in the sensitivity study to data. Figure 6.2 shows the results of the fixed-window limit calculation for the scalar particle (*i.e.:* sneutrino) hypothesis overlaid on the sensitivity curves shown previously. We presently ignore the NLO prediction that is also shown; its relevance is discussed in the following section.

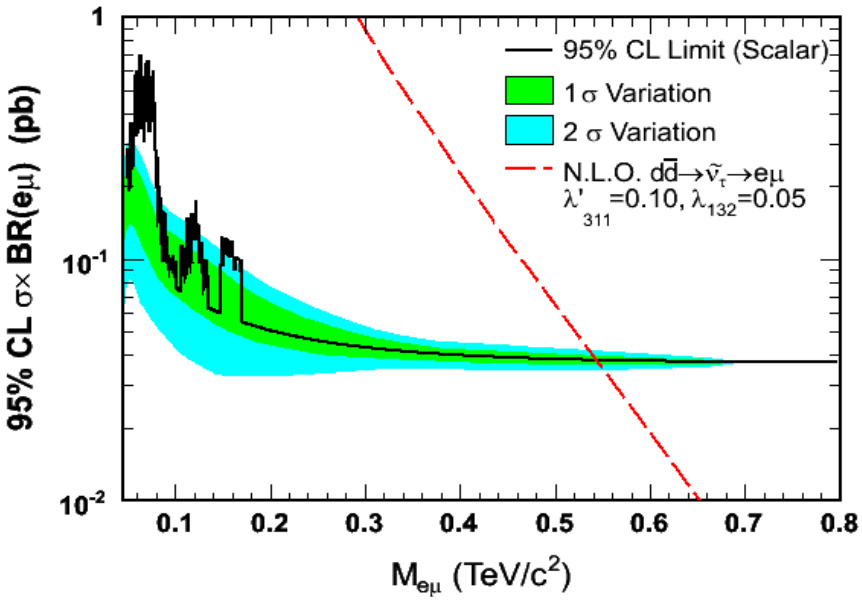

Figure 6.2: **Scalar $\sigma \times \mathrm{Br}(e\mu)$ Upper-Limit.** We plot the $\sigma \times \mathrm{Br}(e\mu)$ determined for the scalar particle hypothesis with the sensitivity curves of the previous chapter. The sharp structure of the upper limit is a result of the discrete acceptance windows applied to data. The hashed line indicates the NLO $d\bar{d} \rightarrow \tilde{\nu}_\tau \rightarrow e\mu$ prediction. Its intersection with the upper limit defines a $\tilde{\nu}_\tau$ mass limit of ~ 540 GeV/c^2.

Figure 6.2 demonstrates good agreement between the upper-limit $\sigma \times \mathrm{Br}(e\mu)$'s determined from data and our predicted sensitivities. The peak near 150 GeV/c^2 contains 2 events. The squarish shape of the peak is a result of these events

falling into and out of the sliding acceptance window used in the $M_{e\mu}$ scan. The jagged structure apparent in the upper-limit is a similar artifact of the fixed-width windows we apply to data. This structure is absent in the upper-limit $\sigma\times$Br(eμ) 's shown in Figure 6.3, which we generate using the Gaussian weighting technique described in the previous chapter. This figure presents the 95% CL upper-limit $\sigma\times$Br(eμ) 's for both scalar (lower curve) and vector (upper curve) particle decays. Limits for the vector hypothesis are less restrictive than those for the scalar due to the difference in acceptance described in Section 5.1.1.

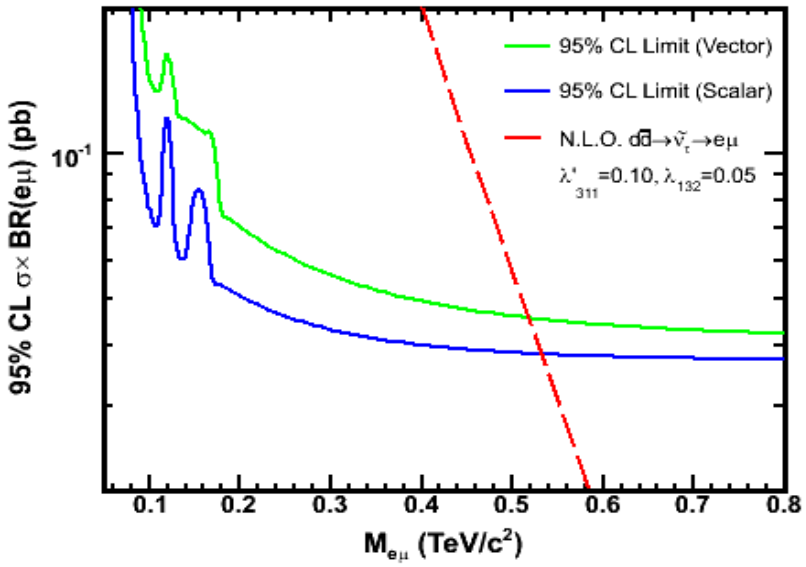

Figure 6.3: **Scalar and Vector $\sigma\times$Br(eμ) Upper Limits.** This plot shows the result of a recalculation of the upper limit $\sigma\times$Br(eμ) for the scalar hypothesis (lower solid curve) using the Gaussian weighting technique. The corresponding limit for the vector particle hypothesis is shown as the solid upper curve. As in Figure 6.2, the intersection of the NLO $d\bar{d}\rightarrow\tilde{\nu}_\tau\rightarrow e\mu$ prediction with the upper limit gives a 95% CL $\tilde{\nu}_\tau$ mass limit of $\sim$ 540 GeV/c^2. We do not show the theoretical $\sigma(Z')\times$Br(eμ) . The intersection of the upper curve with the NLO prediction has no meaning.

Although the acceptance functions we use to determine the upper-limit $\sigma\times$ Br(eμ) curves are determined from Monte Carlo samples of specific physics processes, our results can be interpreted as general constraints on the LFV decays

of heavy scalar and vector particles. The two-body decays of all scalar particles are isotropic and the acceptance for such events is therefore independent of the identity of the parent particle. This fact allows us to use the $H \rightarrow e\mu$ process in PYTHIA to represent RPV $d\bar{d} \rightarrow \tilde{\nu}_\tau \rightarrow e\mu$ decays.

A similar argument applies to the decays of spin-1 particles. In this case, however, the angular distributions of the decay products depend on the particle's chiral couplings to $q\bar{q}$ and $e\mu$. Equation 6.2 shows the angular dependency of the general spin-1 cross section [28]. The g_V and g_A are the vector and axial-vector couplings to quarks and leptons and θ^* is the angle of the outgoing lepton with respect to the incoming quark.

$$\frac{d\sigma(q\bar{q} \rightarrow \ell^+\ell^-)}{d\ cos\theta^*} \propto (g_V^{q\ 2} + g_A^{q\ 2})(g_V^{\ell\ 2} + g_A^{\ell\ 2})(1 + cos^2\theta^*) + 8(g_V^q g_A^q g_V^\ell g_A^\ell) cos\ \theta^* \quad (6.2)$$

Although different assumptions for the vector and axial-vector couplings in Equation 6.2 result in different $e\mu$ angular distributions, all lead to the same acceptance difference with respect to the decays of scalar particles. As shown in Figure A.12, the integral of Equation 6.2 between $\eta = \pm 1$ does not depend on the relative magnitudes of the couplings. As a result, the spin-1 (geometric) acceptance difference is independent of relative differences in left and right-handed couplings. The upper-limit cross section we calculate assuming a pure left-handed ($g_A = -g_V$) coupling therefore represents the general spin-1 result.

6.3 Mass-Coupling Limits

We now use the $\sigma \times \mathrm{Br}(\mathrm{e}\mu)$'s upper-limits presented in the previous section to constrain the RPV SUSY and LFV Z' decay models described in Chapter 2.

Figure 6.3 shows the NLO $d\bar{d} \rightarrow \tilde{\nu}_\tau \rightarrow e\mu$ prediction as a hashed curve that intersects the upper-limit $\sigma \times \mathrm{Br}(\mathrm{e}\mu)$'s. The $M_{e\mu}$ value at which the curve for the scalar hypothesis coincides with the NLO prediction gives the $\tilde{\nu}_\tau$ mass limit ($\sim$ 540 GeV/c^2) for the assumed values of $\lambda_{132} = 0.05$ and $\lambda'_{311} = 0.10$, *i.e.:* the limits from low-energy experiment. These coupling values were also used to determine a $\tilde{\nu}_\tau$ mass limit in the CDF Run I $e\mu$ search. Comparing with the result of that analysis. This is a $\sim$ 170 GeV/c^2 improvement in $\tilde{\nu}_\tau$ mass limit.

Next, we decrease the λ_{132} and λ'_{311} coupling values from the low-energy limits and determine a new set of NLO $\sigma\times\mathrm{Br}(\mathrm{e}\mu)$ predictions. We use these to determine a corresponding set of $\tilde{\nu}_\tau$ mass limits that we plot in Figure 6.4. The Figure depicts excluded regions in the $M_{e\mu} - \lambda'_{311}$ plane, parameterized by values of the λ_{132} coupling. Regions to the left of the curves are excluded at 95% CL. A plot of $M_{e\mu} - \lambda_{132}$ exclusion regions, provided in Figure A.11, does not provide information beyond what is conveyed by Figure 6.4.

The $\tilde{\nu}_\tau$ mass limit found from Figure 6.3 appears in Figure 6.4 as the point at which the $\lambda_{132} = 0.05$ curve intersects the upper axis of the plot. We see that our limits on the RPV couplings are stronger (*i.e.:* smaller) than those set by low-energy experiment for a wide range of $\tilde{\nu}_\tau$ masses. For example, when using the left-most curve of Figure 6.4 and assuming a $\tilde{\nu}_\tau$ mass of 250 GeV/c^2, both λ_{132} and λ'_{311} coupling limits improve to ~ 0.01. The λ'_{311} limit is improved further if the λ_{132} limit is made less restrictive.

We follow a similar procedure to exclude regions in the Z' mass-coupling plane. We use the upper curve of Figure 6.3 and NLO $\sigma(Z')\times\mathrm{Br}(\mathrm{e}\mu)$ predictions from the modified E_6 models (not shown in Figure 6.3) to set simultaneous limits on $m_{Z'}$ and Q^l_{12} . Each E_6 model predicts a $q\bar{q} \rightarrow Z'$ production cross section that we multiply with a $\mathrm{Br}(\mathrm{e}\mu)$ to obtain a Z' LFV decay prediction. We calculate the branching ratios from versions of the models that are extended to include the

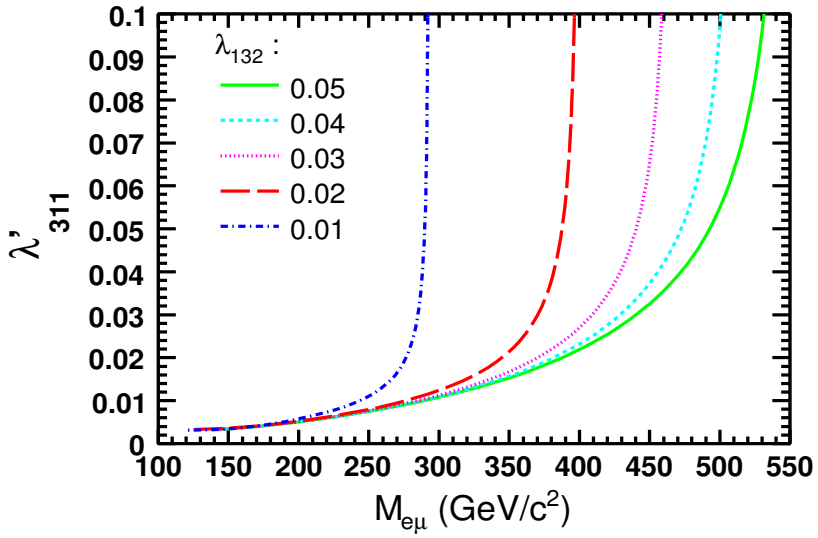

Figure 6.4: $M_{e\mu} - \lambda'_{311}$ **Exclusion Regions.** Regions to the left of the curves represent excluded values of λ'_{311} as a function of $\tilde{\nu}_\tau$ mass and λ_{132} . We obtain the curves by decreasing the RPV coupling values used in the NLO prediction of Figure 6.3 and then plotting the range $M_{e\mu}$ points at which the resulting predictions coincide with the upper-limit $\sigma(\tilde{\nu}_\tau) \times \mathrm{Br}(\mathrm{e}\mu)$.

Q^l_{12} LFV coupling. Figure 6.5 shows the Q^l_{12} values at which the predicted and upper-limit $\sigma(Z') \times \mathrm{Br}(e\mu)$ curves intersect as a function of $m_{Z'}$. The E_6 limits we present are heuristic; E_6 models do not admit LFV Z' couplings by design.

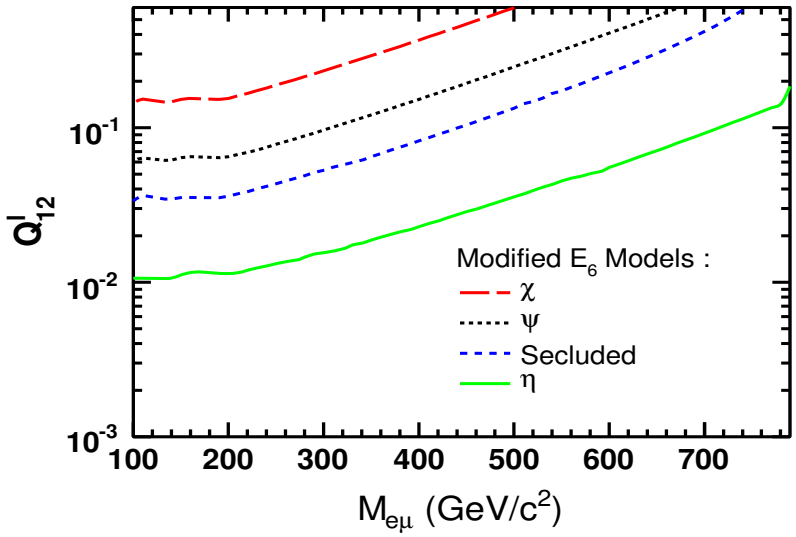

Figure 6.5: $M_{e\mu} - Q^l_{12}$ **Exclusion Region.** Regions above the curves represent excluded values for Q^l_{12} as a function of Z' mass. The displayed limits are meant as an illustration of our $M_{e\mu}$ reach. None of the E_6 models contain a LFV coupling by construction.

Table 2.2 in Section 2.3 suggests that our results are not competitive with the Q^l_{12} limits obtained from SINDRUM II data. Although we are unable to match the sensitivity of that dedicated $\mu \to e$ conversion experiment, our $\sigma(Z')\times$ Br(eμ) limits are not subject to the same degree of model dependence. In addition, our direct search for LFV Z' decay is not as susceptible to coherent interference effects. The amplitudes of SM processes at low momentum transfer can add destructively with that of virtual Z' exchange and suppress a low-energy Z' signature. Our direct search, on the other hand, involves resonant Z' production at large values of momentum transfer, where the SM contribution to the amplitude is small. Thus, while not as quantitatively impressive as the results of low-energy

experiment, our $m_{Z'} - Q^l_{12}$ results compliment existing limits.

Figure 6.6 provides another representation of our Z' limits. The cross section for $p\bar{p} \rightarrow Z' \rightarrow e\mu$ in the narrow width approximation given by Equation 6.3 [69].

$$\sigma(p\bar{p} \rightarrow Z' \rightarrow e\mu) = \frac{\pi}{48s} W_{Z'}(s, m^2_{Z'}) \mathrm{Br(Z' \rightarrow e\mu)} \tag{6.3}$$

Here s is the square of the center of mass energy and $W_{Z'}$ is a hadronic structure function. $W_{Z'}$ depends on the Z' couplings to left-handed quark doublets (z_q), its couplings to right-handed quark singlets (z_u, z_d) and functions w_u and w_d, which encapsulate QCD dependency:

$$W_{Z'}(s, m^2_{Z'}) = g^2_Z[(z^2_q + z^2_u)^2 w_u(s, m^2_{Z'}) + (z^2_q + z^2_d)^2 w_d(s, m^2_{Z'})] \tag{6.4}$$

The cross section in Equation 6.3 can be rewritten to separate the Z' couplings, which are model dependent, from the structure function, which is calculated independently from s, the Z' mass and parton distribution functions.

$$\sigma(p\bar{p} \rightarrow Z' \rightarrow e\mu) = \frac{\pi}{48s}[c_u w_u(s, m^2_{Z'}) + c_d w_d(s, m^2_{Z'})] \tag{6.5}$$

$$c_{u,d} = g^2_z(z^2_q + z^2_{u,d}) \cdot \mathrm{Br(Z' \rightarrow e\mu)} \tag{6.6}$$

Our upper-limits on the $\sigma(Z') \times \mathrm{Br(e\mu)}$ translate directly to excluded regions in the $c_u - c_d$ plane. Figure 6.6 shows four $c_u - c_d$ curves parameterized by $m_{Z'}$. Areas above the curves are excluded at 95% CL. Our results compare well with similar limits obtained in the CDF Z' dilepton search [31]. That analysis, for example, presents limiting c_u and c_d values for a 400 GeV/c^2 Z' of 1×10^{-4} and $c_d = 9 \times 10^{-4}$ respectively.

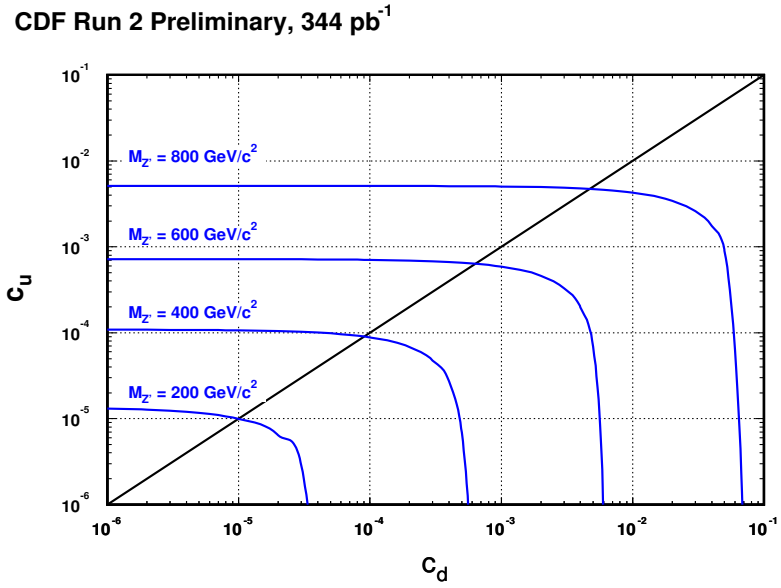

Figure 6.6: $c_u - c_d$ **Exclusion Region.** Regions above the curves indicate excluded combinations of the model-dependent c_u and c_d parameters as a function of Z' mass.

Chapter 7

Conclusions

To summarize, we have searched 344 pb^{-1} for evidence of LFV decays of heavy neutral particles to $e\mu$. We obtain results that are consistent with SM predictions and we set general, upper-limit $\sigma \times \text{Br}(\text{e}\mu)$'s on the decays of scalar and vector particles. With these results we develop simultaneous constraints on the masses and LFV couplings of the $\tilde{\nu}_\tau$ and Z' in RPV SUSY and modified E_6 models respectively. Our search improves the $\tilde{\nu}_\tau$ mass limit to ~ 540 GeV/c^2 when assuming low-energy limits for the RPV couplings, a ~ 170 GeV/c^2 gain with respect to the CDF Run I result.

The ubiquity of LFV effects in extensions to the SM guarantees that searches for LFV will be of continued experimental interest. Direct searches for LFV processes are likely to be conducted at an early stage in the operation of the CERN Large Hadron Collider (LHC) and will cover the parameter space that remains for TeV-scale LFV phenomena. RPV sneutrino production cross sections, for example, are $10^1 - 10^4$ times larger at the LHC than corresponding values at the Tevatron [70]. At a pp collision energy of $\sqrt{s} = 14$ TeV , the Drell-Yan production of Z' bosons will be similarly enhanced [71].

While the discovery potential of the LHC is vast, the large integrated lumi-

nosities delivered by the Tevatron and the mature understanding of the CDF/D0 detectors that has developed sustain hopes for an early discovery of LFV New Physics. An ongoing CDF analysis will extend the $e\mu$ search to 1 fb^{-1}, more than three times the amount of data used in this analysis. The search will employ new electron identification techniques that have been shown to increase acceptance by $\sim 7\%$. The approach utilizes a calibration of the strips and wires of the CES chambers to provide energy measurements for electrons that are independent of those obtained with the CEM calorimeter. Energy depositions on the strips and wires can then be associated to form two dimensional clusters matched to COT tracks. This technique permits replacement of the current $E/P < 2$ and χ^2_{strip} electron ID cuts, which tend to be over-efficient in their rejection of electrons.

Perhaps more interesting will be the exploration of the $e\tau$ and $\mu\tau$ channels in this analysis. Strong theoretical motivations support searches that include the tau channels. Models that introduce multiple Higgs doublets, for example, can give rise to LFV couplings (κ_{ij}) from the mixing between Higgs of different generations [72]. The maximal $\nu_\tau - \nu_\mu$ mixing indicated by the Superkamiokande data suggests that the $\kappa_{\tau\mu}$ coupling is large. As a result, such models can predict a significant $h \to \mu\tau$ branching ratio. In the absence of a discovery, limits on $\kappa_{\tau\mu}$ are expected to improve substantially with 1 fb^{-1} of Run II data over those achieved by low-energy experiments.

Both RPV SUSY and family non-universal Z' models can also give rise to an $\ell - \tau$ signature. A preferential Z' coupling to the third family has been shown to improve fits to electroweak precision data [73]. The non-diagonal $\ell - \tau$ couplings that result after lepton mixing are less constrained by low-energy experiment than those for $e\mu$ [74]. Existing low-energy limits on the RPV SUSY couplings associated with a $\ell - \tau$ final-state are likewise more than an order of magnitude larger than the low-energy limit on the $e\mu$ coupling considered in this analysis [75].

The future analysis will be sensitive to the predictions of such models through the reconstruction of hadronic tau decays. Tau reconstruction at CDF makes use of an "isolation cone" that surrounds a high-p_T track matched to a calorimeter cluster. A requirement on the number of tracks within the isolation cone allows tau candidates to be discriminated from jets. Currently, the reconstruction of π^0 candidates in tau decays relies on one dimensional position measurements from the CES and a subtractive technique to obtain an indirect π^0 energy measurement from the CEM calorimeter. Tau identification will be improved in the analysis by extending the use of two dimensional CES clusters to π^0 reconstruction.

With a larger dataset and increased acceptance, the future analysis will substantially increase sensitivity to LFV predictions. We anticipate larger event yields above $M_{e\mu} = 100$ GeV/c^2 and we plan to improve the statistical techniques used to analyze the $M_{e\mu}$ distributions. We desire a method that is capable of providing a better indication of consistency between observation and SM predictions. Given the compelling theoretical and phenomenological rationales for weak-scale LFV, we will also prepare for a possible discovery of heavy new particles and the LFV decays.

Bibliography

[1] M. L. Perl *et al.*, Phys. Rev. Lett. **35**, 1489 (1975).

[2] Herb *et al.*, Phys. Rev. Lett. **39**, 252 (1977).

[3] F. Abe *et al.*, Phys. Rev. Lett. **74**, 2626 (1995).

[4] S. Abachi *et al.*, Phys. Rev. Lett. **74**, 2632 (1995).

[5] K. Kodama *et al.*, Phys. Lett. B **504**, 218 (2001).

[6] C.S. Wu *et al.*, Phys. Rev. **105**, 1413 (1957).

[7] J. H. Christensen *et al.*, Phys. Rev. Lett. **13**, 138 (1964).

[8] R. Davis Jr., Phys. Rev. Lett. **12**, 303 (1964).

[9] J. N. Bahcall, Phys. Rev. Lett. **12**, 300 (1964).

[10] Y. Fukuda *et al.*, Phys. Rev. Lett. **81**, 1562 (1998).

[11] Q. R. Ahmad *et al.*, Phys. Rev. Lett. **87**, 71301 (2001).

[12] S. Coleman and S. Glashow, Phys. Lett. B **405**, 249 (1997).

[13] M.C. Gonzalez-Garcia and Y. Nir, Rev. Mod. Phys. **75**, 345 (2003).

[14] A. Abulencia *et al.*, accepted for publication in Phys. Rev. Lett., [arXiv:hep-ex/0603006].

[15] J. Wudka, J. Phys. G: Nucl. Part. Phys. **31**, 1401 (2005).

[16] M. L. Brooks *et al.*, Phys. Rev. Lett. **83**, 1521 (1999).

[17] U. Bellgardt *et al.*, Nucl. Phys. B **299**, 1 (1988).

[18] R. D. Bolton *et al.*, Phys. Rev. D **38**, 2077 (1988).

[19] T. Appelquist and J. Carazzone, Phys. Rev. D **11**, 2856 (1975).

[20] An explanation of the stability fermion masses to corrections from heavy particles is provided on page 3, M. Drees, *An Introduction to Supersymmetry*, [arXiv:hep-ph/9611409].

[21] The mass of a neutralino LSP can be constrained by cosmological observations : D. Hooper and T. Plehn, Phys. Lett. B **562**, 18 (2003).

[22] S. Martin, *A Supersymmetry Primer*, [arXiv:hep-ph/9709356].

[23] F. Ledroit and G. Sajot, GDR-S-008 (1998).

[24] R.M. Barnett *et al.*, Phys. Rev. D **54**, 1 (1996).

[25] D. Acosta *et al.*, Phys. Rev. Lett. **91**, 171602 (2003).

[26] R. Barbier *et al.*, Phys. Rept. **420**, 1-202 (2005).

[27] H. Georgi and S. Glashow, Phys. Rev. Lett. **32**, 438 (1974).

[28] BNV interactions are shown to result from general SU(5) models : P. Renton, *Introduction to the Physics of Quarks & Leptons*, Cambridge University Press, Cambridge (1990), page 546.

[29] S. Weinberg, Phys. Rev. D **26**, 287 (1982).

[30] J. Schwarz, "The Second Superstring Revolution", Sakharov Conference Proceeding (1996), [arXiv:hep-th/9607067].

[31] A. Abulencia *et al.*, Phys. Rev. Lett. **95**, 252001 (2005).

[32] P. Langacker and J. Kang, Phys. Rev. D **71**, 035014 (2005).

[33] P. Langacker, private communications (2005).

[34] J. Bernabeu *et al.*, Nucl. Phys. B **409**, 69 (1993).

[35] W. Honecker *et al.*, Phys. Rev. Lett. **76**, 200 (1996).

[36] B. Murakami, Phys. Rev. D **65**, 055003 (2002).

[37] L. Sönnenschein, ICHEP Conference Proceeding (2004), [arXiv:hep-ex/0410036].

[38] NLO sneutrino production cross sections were provided to us by S. Majhi, co-author of [70]. The authors had previously provided cross section values at $\sqrt{s} = 1.8$ TeV for the CDF Run I $e\mu$ search.

[39] A technique called "slip stacking" is important for the generation of large $\bar{p}$ yields : S. Shukla, *Slip Stacking in the Fermilab Main Injector*, Snowmass Conference Proceeding (1996).

[40] G. Jackson and G. W. Foster, *Storage Ring for Enhanced Antiproton Production at Fermilab* , IEEE PAC Conference Proceeding (1996).

[41] CDF II Collaboration, FERMILAB-PUB-96/390-E (1996).

[42] D. Acosta *et al.*, Nucl. Instrum. Meth. A **461**, 540 (2001).

[43] F. Abe *et al.*, Phys. Rev. D **50**, 5550 (1994). The value in this paper, 60.3 mb, is determined for collisions at $\sqrt{s} = 1.8$ TeV. The inelastic cross section at $\sqrt{s} = 1.96$ TeV extrapolates to 61.7 mb.

[44] T. Affolder *et al.*, Nucl. Instrum. Meth. A **526**, 249 (2004).

[45] C. Paus, *et. al.*, Nucl. Instrum. Meth. A **461**, 579 (2001).

[46] L. Balka *et al.*, Nucl. Instrum. Meth. A **267**, 272 (1988).

[47] S. Bertolucci *et al.*, Nucl. Instrum. Meth. A **267**, 301 (1988).

[48] G. Ascoli *et al.*, Nucl. Instrum. Meth. A **268**, 33 (1988).

[49] A. Artikov *et al.*, Nucl. Instrum. Meth. A **538**, 358 (2005).

[50] K. Anikeev *et al.*, "CDF Level 2 Trigger Upgrade", IEEE Trans. Nucl. Sci., accepted for publication (2005).

[51] G. Gomez-Ceballos, *et al.*, Nucl. Instrum. Meth. A **518**, 522 (2004).

[52] PYTHIA v6.216. T. Sjöstrand *et al.*, Comp. Phys. Commun. **135**, 238 (2001).

[53] M. Cacciari *et al.*, JHEP **0404**, 068 (2004).

[54] J. M. Campbell and R. K. Ellis, Phys. Rev. D **60**, 113006 (1999).

[55] C. R. Hamberg, W.L. van Neerven and T. Matsuura, Nucl. Phys. B **359**, 343 (1991).

[56] S. Dimopolous, *et al.*, Phys. Rev. D **41**, 2099 (1990).

[57] GEANT v3.2113. R. Brun *et al.*, *GEANT: Simulation Program for Particle Physics Experiments. User Guide and Reference Manual*, CERN-DD-78-2-REV.

[58] H. L. Lai *et al.*, Eur. Phys. J. C **12**, 375 (2000).

[59] A. Abulencia *et al.*, submitted to Phys. Rev. D, [arXiv:hep-ex/0508029].

[60] A discussion of rotation matrices is found in Appendix C : D. Perkins, *Introduction to High Energy Physics*, Cambridge University Press, Cambridge, 2000.

[61] D. Acosta *et al.*, Phys. Rev. Lett. **93**, 142001 (2004).

[62] The CDF Statistics Committee: J. Heinrich *et al.*, [arXiv:physics/0409129].

[63] GSL software, `http://www.gnu.org/software/gsl/`

[64] S. Majhi, private communications (2005).

[65] HERWIG 6.5, G. Corcella, I.G. Knowles, G. Marchesini, S. Moretti, K. Odagiri, P. Richardson, M.H. Seymour and B.R. Webber, JHEP **0101**, 010 (2001) [arXiv:hep-ph/0011363], [arXiv:hep-ph/0210213].

[66] J. Pumplin *et. al.*, Phys. Rev. D **65**, 014013 (2002).

[67] S. Klimenko, J. Konigsberg, and T.M. Liss, FERMILAB-FN-0741 (2003).

[68] D. Acosta *et al.*, Phys. Rev. D **71**, 091105 (2005).

[69] M. Carena, A. Deleo, B. Dobrescu, T. Tait. *Z' Gauge Bosons at the Tevatron*, FERMILAB-Pub-04/129-T (2004).

[70] D. Choudhury, S. Majhi and V. Ravindran, Nucl. Phys. B **660**, 343 (2003).

[71] M. Cvetic and S. Godfrey, *Discovery and Identification of Extra Gauge Bosons*, [arXiv:hep-ph/9504216], to be published in *Electroweak Symmetry Breaking and Beyond the Standard Model*, eds T. Barklow, S. Dawson, H. Haber, and J. Seigrist.

[72] T. P. Cheng and M. Sher, Phys. Rev. D **35**, 3484 (1987).

[73] J. Erler and P. Langacker, Phys. Rev. Lett. **84**, 212 (2000).

[74] P. Langacker and M. Plumacher, Phys. Rev. D **62**, 013006 (2000).

[75] M. Chemtob, Prog. Part. Nucl. Phys. **54**, 71 (2 005).

Appendix A

Additional Figures

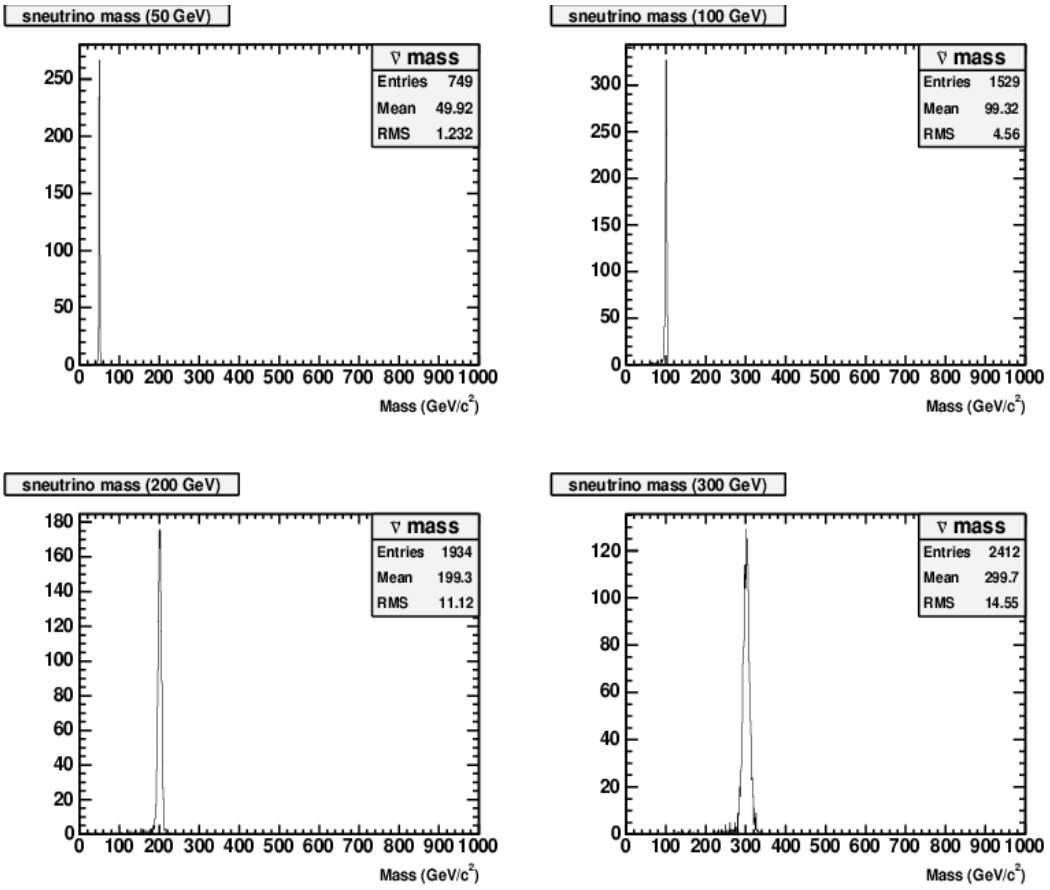

Figure A.1: **Sneutrino Mass Distributions.** These plots show reconstructed $M_{e\mu}$ distributions from the $50 - 300$ GeV/c^2 samples. We use the widths of the distributions to set the size of the acceptance window we apply in the upper-limit cross section calculations. The distributions broaden due to the degradation of muon p_T resolution with increasing momentum.

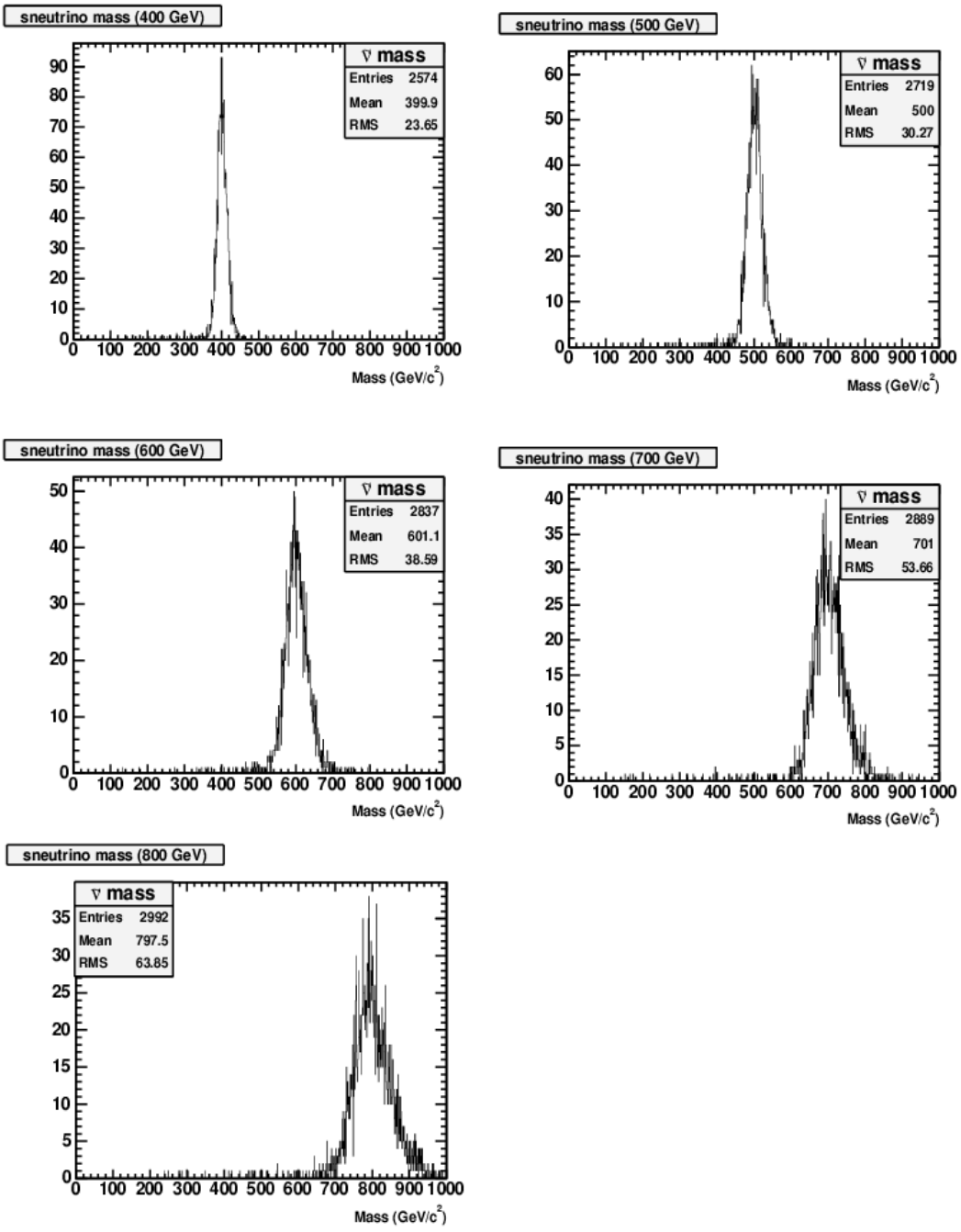

Figure A.2: **Sneutrino Mass Distributions.** These plots show reconstructed $M_{e\mu}$ distributions from the $400 - 800$ GeV/c^2 samples. We use the widths of the distributions to set the size of the acceptance window we apply in the upper-limit cross section calculations. The distributions broaden due to the degradation of muon p_T resolution with increasing momentum.

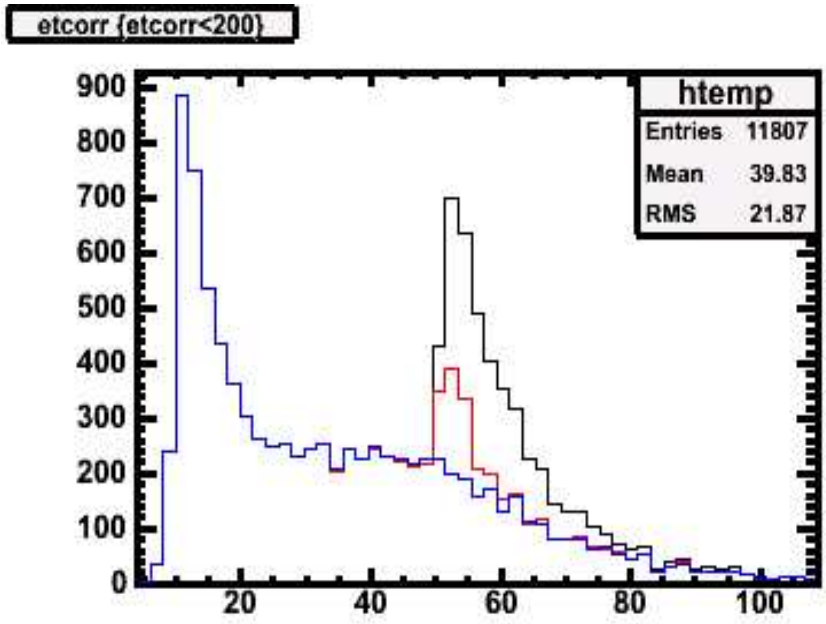

Figure A.3: **Jet Sample Unbiasing.** The raw E_T distribution from the Jet50 sample is shown in black (the larger histogram peaked at 50 GeV). The smaller (red) peak at 50 GeV results when we apply our unbiasing procedure without first correcting the Jet E_T for the difference in on-line vs. off-line Z_0. The blue curve (peaked at 10 GeV) results when we apply this correction and indicates that we are able to remove most of the trigger bias.

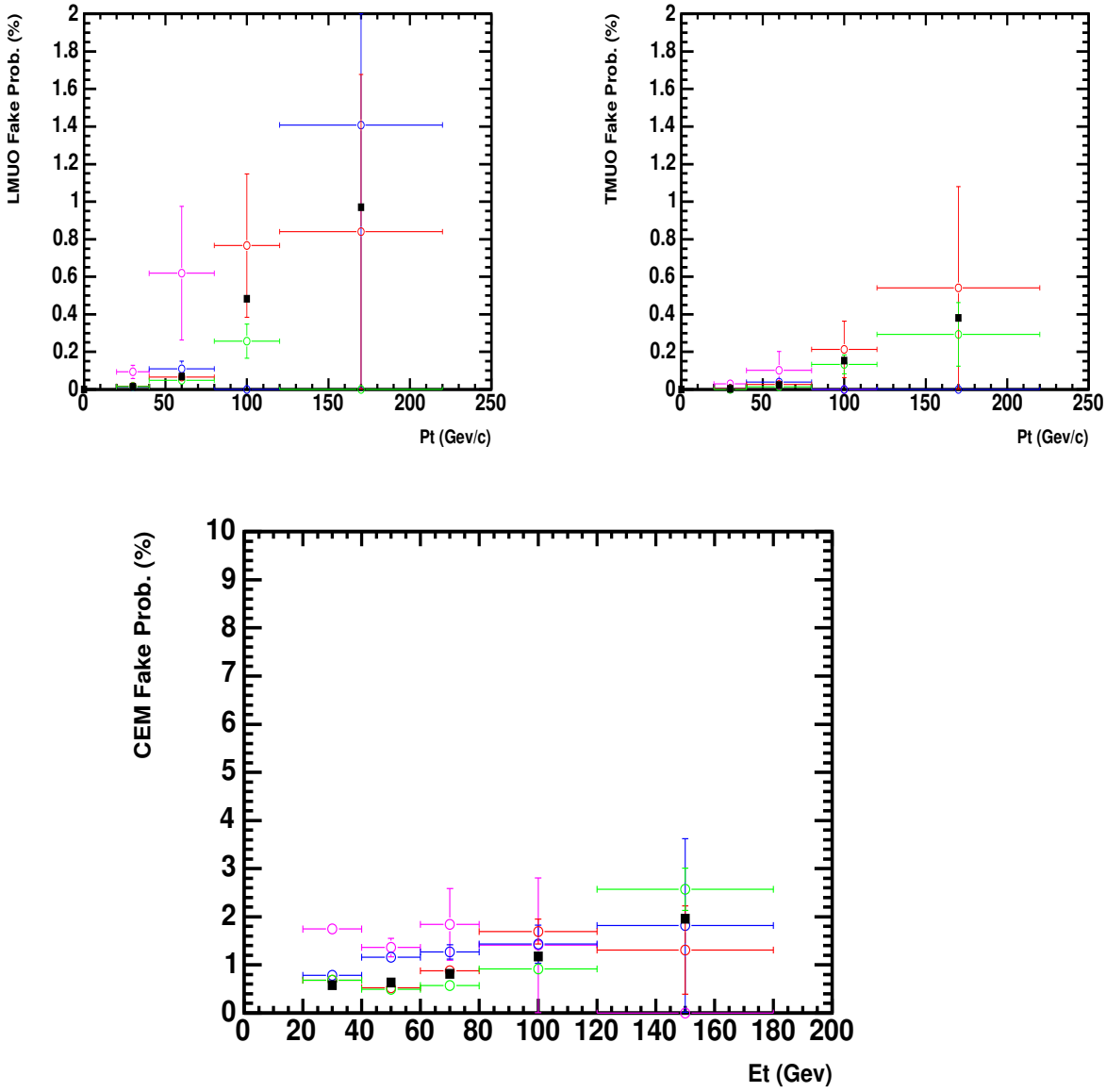

Figure A.4: Jet → Lepton **Fake Rates.** Fake rates measured in various jet data samples (jet20=magenta, jet50=blue, jet70=red and jet100=green) are generally consistent. Differences in the fake rates are used to estimate the systematic uncertainty on the fake lepton background.

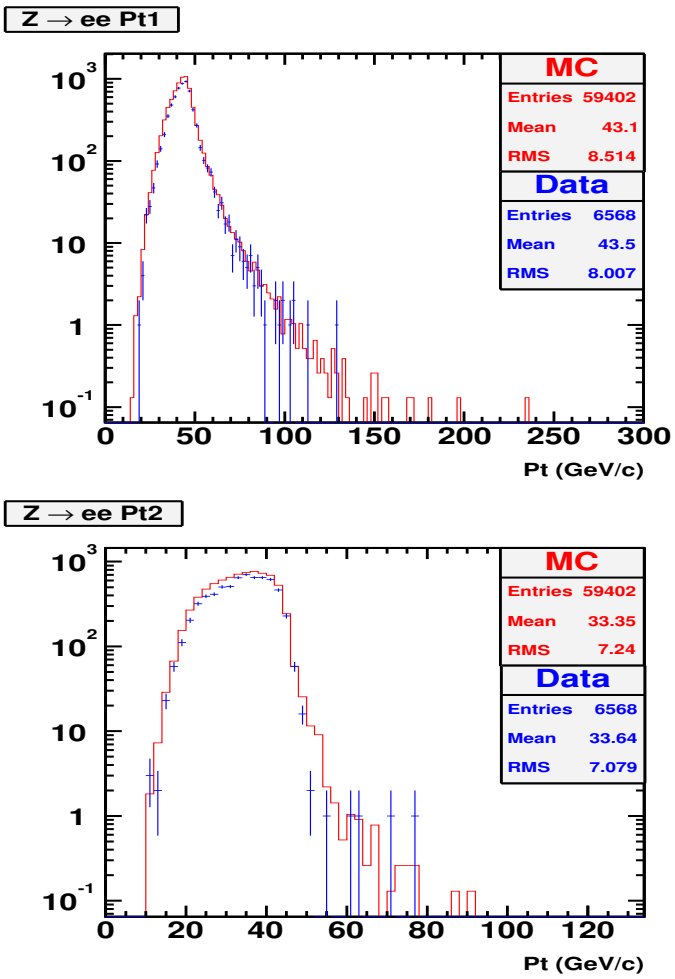

Figure A.5: $Z \rightarrow ee$ p_T **Distributions.** The upper distribution shows the p_T of the leading electrons from data (points) and MC (line) pairs that pass our electron/electron control region selection. The lower distribution compares the p_T's of the lower-p_T electrons.

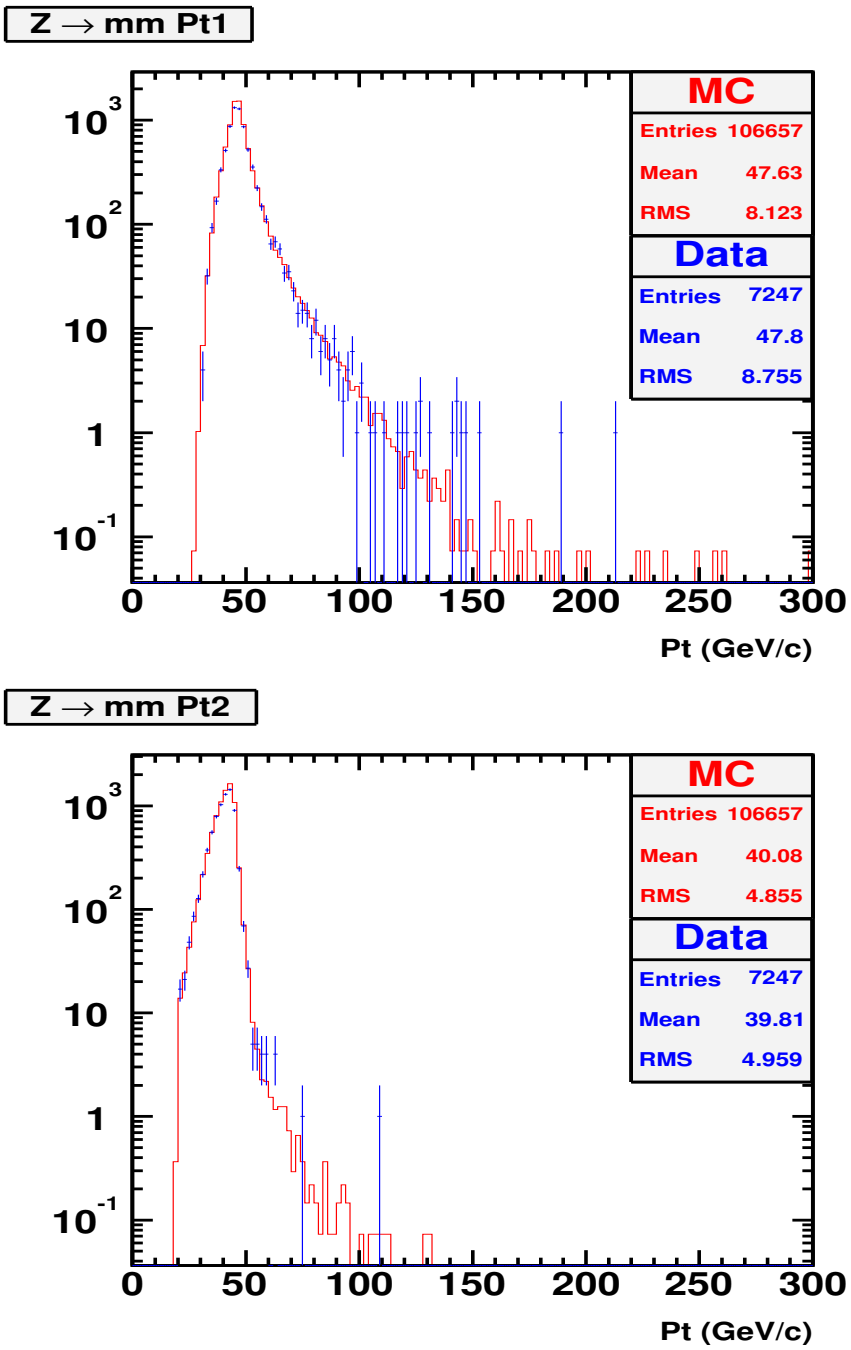

Figure A.6: $Z \rightarrow \mu\mu$ p_T **Distributions.** The upper distribution shows the p_T of the leading muons from data (points) and MC (line) pairs that pass our muon/muon control region selection. The lower distribution compares the p_T's of the lower-p_T muons.

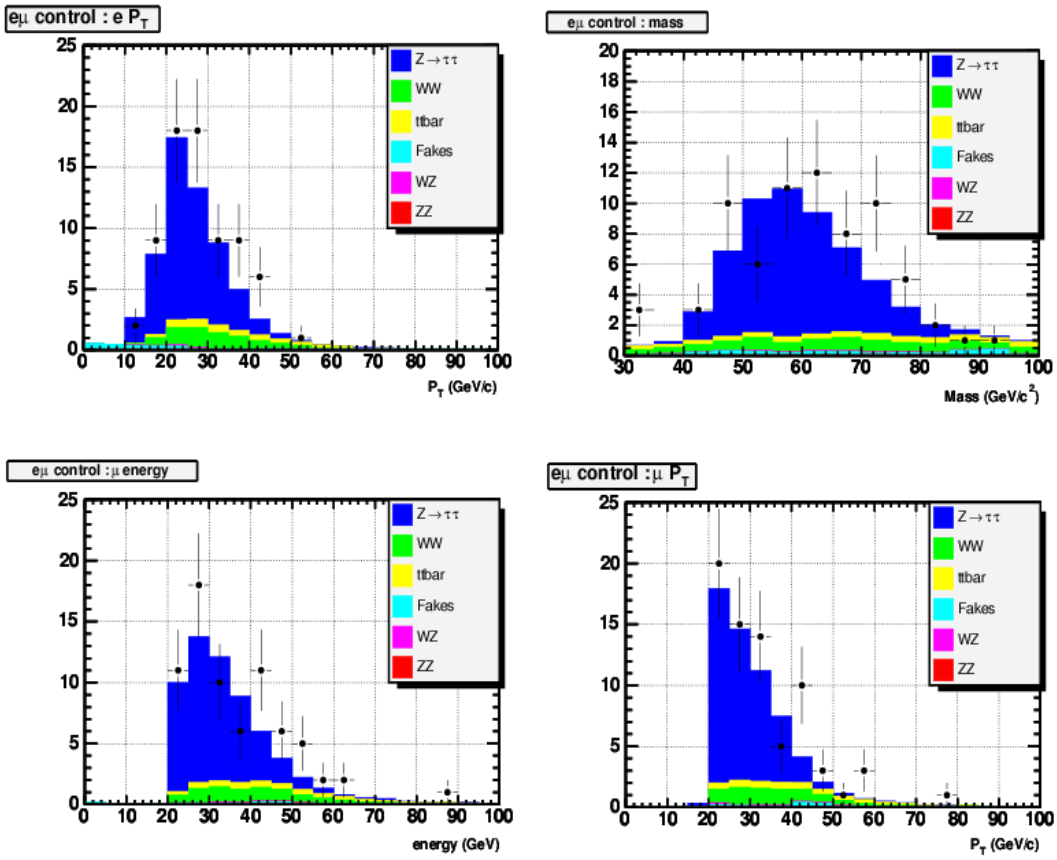

Figure A.7: $e\mu$ **Control Region Kinematics.** We compare the predicted and observed kinematic distributions of $e\mu$ pairs below 100 GeV/c^2 to verify our event selection procedure.

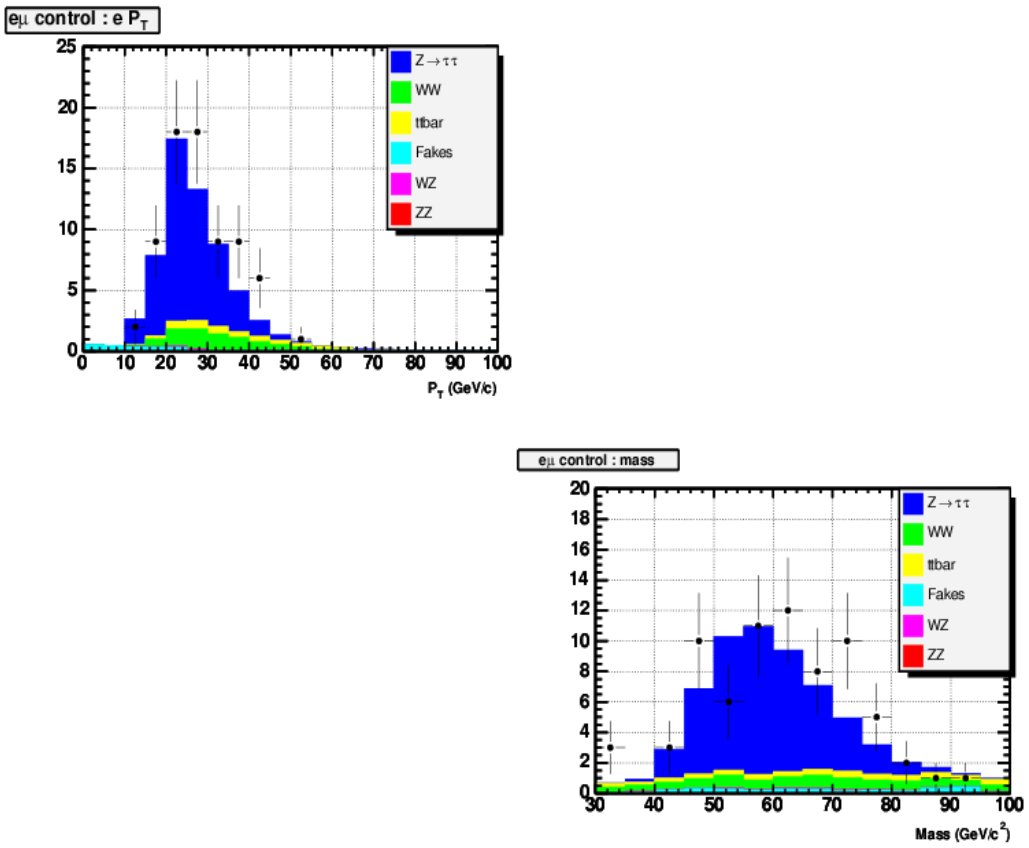

Figure A.8: $e\mu$ **Control Region Kinematics.** We compare the predicted and observed kinematic distributions of $e\mu$ pairs below 100 GeV/c^2 to verify our event selection procedure.

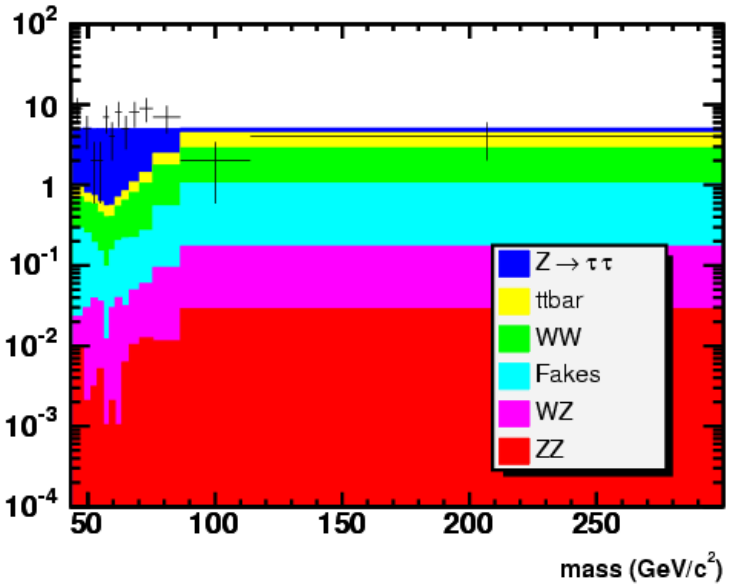

Figure A.9: $e\mu$ **Control Region Kinematics.** We use bins of variable width in the χ^2 test to obtain predicted bin occupancies of at least 5 events.

Bin	**Upper edge**	**Expected**	**Observed**
1	50	5.10 ± 2.24	5
2	51.2	5.02 ± 2.24	2
3	53.7	5.03 ± 2.26	2
4	56	5.01 ± 2.24	7
5	58.4	5.03 ± 2.24	4
6	60.7	5.02 ± 2.24	8
7	63.4	5.00 ± 2.24	5
8	66.3	5.05 ± 2.24	8
9	70.3	5.08 ± 2.24	9
10	75.7	5.04 ± 2.25	7
11	86.5	5.08 ± 2.25	2
12	114	5.80 ± 2.24	4
total χ^2			14.0
p value			0.23

Table A.1: **Reduced χ^2 Results.** We perform a χ^2 to determine the consistency between the observed and predicted SM background $M_{e\mu}$ distributions. The resulting p-value indicates good agreement.

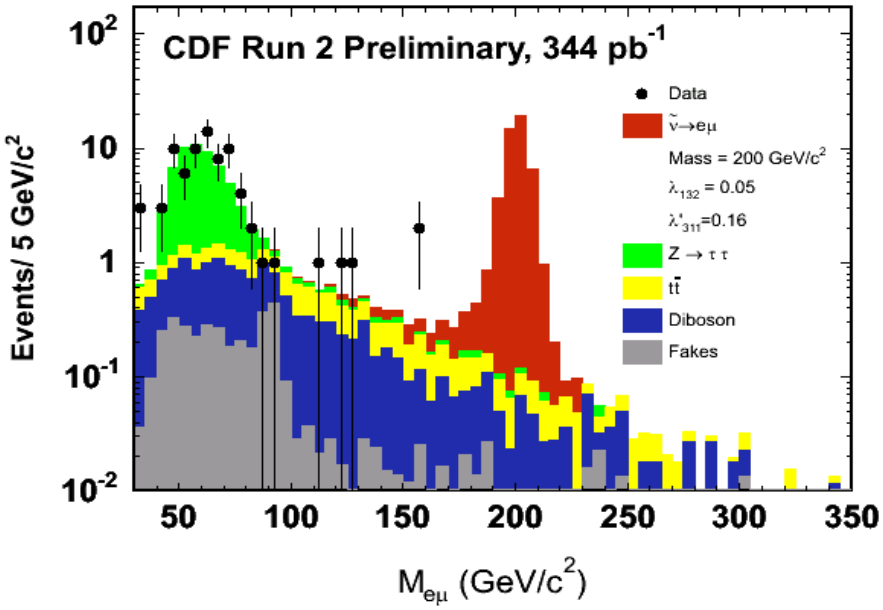

Figure A.10: $M_{e\mu}$ **Distribution with** $\tilde{\nu}_\tau$ 300 GeV/c^2 **Hypothesis.** We use the NLO $\sigma(\tilde{\nu}_\tau) \times \mathrm{Br}(e\mu)$ and the $\tilde{\nu}_\tau$ acceptance curve to predict the number of at 300 GeV/c^2 $\tilde{\nu}_\tau$'s in data. Following procedures described in Section 5.3, we construct a hypothetical $M_{e\mu}$ distribution from the total $\tilde{\nu}_\tau$ expectation and add this to the background distribution. The plot shows that data is not consistent with the 300 GeV/c^2 hypothesis.

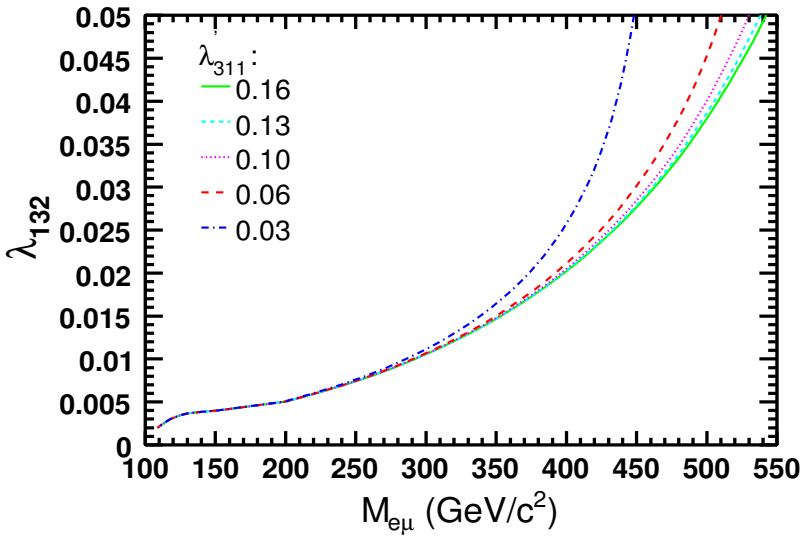

Figure A.11: $M_{e\mu} - \lambda'_{311}$ **Exclusion Regions.** Regions to the left of the curves represent excluded values of λ'_{311} as a function of $\tilde{\nu}_\tau$ mass and λ_{132} . The curves are obtained by decreasing the RPV coupling values used in the NLO prediction of Figure 6.3 and plotting the range $M_{e\mu}$ points at which the resulting predictions coincide with the upper-limit $\sigma(\tilde{\nu}_\tau) \times \mathrm{Br}(\mathrm{e}\mu)$.

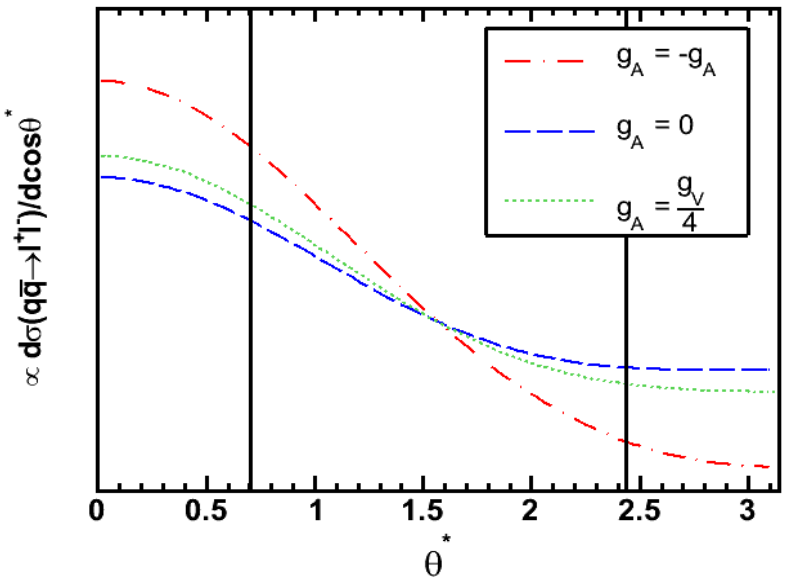

Figure A.12: **Spin-1 Angular Dependence.** This plot demonstrates the angular dependence of $\sigma \times \mathrm{Br}(e\mu)$ for a general spin-1 particle on the vector and axial-vector couplings. Different values of the couplings in Equation 6.2 lead to different angular distributions of the final-state leptons. Z' acceptance is not influenced by these differences because the integrated cross sections are equal in $\eta = \mp 1$ range (the area between the solid vertical lines).